Design and Fabrication of Granular Materials for Surface Acoustic Waves

by

Tian Gan

B.S. Department of Intensive Instruction
Nanjing University, China, 2012

Submitted to the Department of Mechanical Engineering and the Department of Electrical Engineering & Computer Science in Partial Fulfillment of the Requirements for Degrees of

Master of Science in Mechanical Engineering and
Master of Science in Electrical Engineering & Computer Science

at the

Massachusetts Institute of Technology
June 2015

ARCHIVES
MASSACHUSETTS INSTITUTE OF TECHNOLOGY
JUL 30 2015
LIBRARIES

© 2015 Massachusetts Institute of Technology. All Rights Reserved

Signature of Author..... Signature redacted .....
Department of Mechanical Engineering
Department of Electrical Engineering & Computer Science
May 19, 2015

Certified by ... Signature redacted .....
Nicholas Fang
Associate Professor of Mechanical Engineering
Thesis Supervisor

..... Signature redacted
Karl Berggren
Professor of Electrical Engineering & Computer Science
Thesis Reader

Accepted by ..... Signature redacted .....
David Hardt
Professor of Mechanical Engineering
Chair, Mechanical Engineering Committee on Graduate Students

..... Signature redacted ...
Leslie Kolodziejski
Professor of Electrical Engineering & Computer Science
Chair, Electrical Engineering & Computer Science Committee on Graduate Students

Design and Fabrication of Granular Materials for Surface Acoustic Waves

by

Tian Gan

Submitted to the Department of Mechanical Engineering and the Department of Electrical Engineering and Computer Science in Partial Fulfillment of the Requirement for Degrees of

Master of Science in Mechanical Engineering and
Master of Science in Electrical Engineering and Computer Science

Abstract:

Granular materials with structural discreteness and periodicity can lead to novel propagation behaviors of mechanical waves. Acoustic studies of granular media typically involve macroscopic particles whereas contact-based vibrations of microparticles remain largely unexplored. The adhesion which can be neglected on millimeter scale is significant on micron scales and therefore microparticles are expected to yield qualitatively different dynamics.

We model the microparticle array as locally resonant metamaterials for surface acoustic waves by using the effective medium approach. In experiment, we employ the convective assembly method to fabricate the centimeter-sized, two-dimensional granular crystal consisting of 1μm silica spheres adhered to the substrate. Laser-induced transient grating technique is used to generate and detect surface acoustic waves in microsphere array samples. We demonstrate, both experimentally and by theoretical analysis, that the Rayleigh wave in the substrate interacts with the contact resonance of microspheres leading to hybridization and "avoided-crossing" at a high frequency regions$\sim 10^2$MHz.

Furthermore, we fabricate the microsphere waveguide structure by template-assisted-self-assembly. By using the same laser technique, we have observed the waveguide behavior in experimental measurement.

Thesis Supervisor: Prof. Nicholas Fang
Title: Associate Professor of Mechanical Engineering

Thesis Reader: Prof. Karl Berggren
Title: Professor of Electrical Engineering & Computer Science

To my family and friends

Acknowledgements

I would like to acknowledge and thank my advisor, Prof. Nicholas Fang. He provided me with the chance, and made my graduate research possible. I have learned so many thing when working with him. He was always patient to educate me, listen to my thoughts, and give me valuable suggestions. It's easy for a graduate student get lost in the long-term education and research period. Fortunately, my adviser always shows me the greatest support and understanding to my decisions in study and research. He stands from my perspective and considers for me. Also to my thesis reader, Prof. Karl Berggren, I thank him for all of the offer of assistance during my thesis preparation.

With much love, I thank my mom and my dad. I thank my mother for being mother and for taking care of me so well. I thank my father for using the chimney built by rectangular bricks as an example to explain the idea of calculus to me when I was a kid. My father has shown me how lovely and sweet a father can be. Also to my cousin, Feifei, thank you for chatting, shopping and having fun with my mother when I was in the U.S.

To Dr. Nicholas Boechler, I do not think I can thank you enough. You taught me physics and how to do research. You gave me guidance on my experiment and took patience to help me conquer research challenges.

To Dr. Jun Xu, thanks for helping me settle down in Prof. Fang's group and for all of your help with my research. To Anshuman, many thanks to you. You are a great labmate, collaborator, TA and friend. Thanks for all the time in explaining the physics to me. Thanks for all the suggestions and discussions about our research project. To Jeff and Alex, you are great collaborators. Jeff, I hope you do well during the postdoctoral time and hope you do well after that. Alex, thank you so much for giving me ideas and suggestions. Your tutoring and explanations have helped me so much. To Eunnie, I thank you for all of your help in my study, research and life. You are always the "go-to" person during my graduate school time. To Fan Wang, I appreciate all of your patience in listening to me and your offer of assistance. I look forward to watching movie and having fun with Zhitian again! To Mo, thank you for all the help with my coursework, my research and for all the fun you have brought to us. To Qing Zhao, you are my best friend in graduate school and you are also my friend for life. I hope you do well when I am away from you. Yet we will definitely keep in touch and visit each other later. To Yi Huang, you are the most wonderful girl and friend I have ever met. I hope everything goes well with you and I believe so. To Sha Miao, you are such a lovely "sunny girl". And hope those oil companies get through the difficult time soon and so does your project. Greatest wishes to you. To Yangying Zhu, you are a great friend and sister to me. Thanks for the offer of help in my research and my coursework. To Yongbin Sun, you are a great project partner. Thanks for your understanding and all the help. Best wishes to you and Xiaoyu.

I thank my friends in MIT-CHIEF, you have given me so much fun. I thank Le, you are a great confounder for our confounder day event. Thanks for teaching me "take-it-easy". To Jiayuan, we call each other sister and we are! To Yan, Xuanhe, Zhuo, Pei, and Jiayuan, thanks for the hot-pot party and thanks for the Sichuan peppercorn powder.

Last but not least, my deepest gratitude goes to my best friend: Xueying and Lulu. Xueying, you have given me so much fun since my undergraduate time. Although sometimes you are too talkative and I have to endure your forever chatting, I am often way too talkative as well. So thanks for your patience and for always considering for me. To Lulu, you are my best friend forever. We have been best friend since secondary school. Fortunately, the technology has developed so well that we can chat everyday although we are far from each other geographically.

Contents

List of Figures

Chapter 1 Introduction

This thesis concentrates on the wave phenomenon in granular crystal system composed of microscale particles and explores the possibility of modulating mechanical waves at high frequencies as desired by various engineering applications. We demonstrate that the effective modulation of mechanical surface waves can be achieved by coupling the contact resonance of a two-dimensional granular crystal consisting of microparticles and surface acoustic waves (SAWs) propagating along the substrate surface via both numerical computation and experimental measurement. This introduction contains the description of the project motivation, a brief historical setting and thesis organization.

1.1 Motivation

A mechanical wave is essentially a propagating oscillation of matter. Different from electromagnetic waves, the propagation of mechanical waves has to be supported by medium. Mechanical waves can take different forms dependent on medium and wavelength/frequency. In general, the wavelength of a mechanical wave is inversely proportional to the frequency. The most common examples of mechanical waves such as sound waves and water waves occur at sonic or subsonic frequencies and have macroscopic wavelengths. The ultrasound waves used for biomedical imaging are in the range of 1~10MHz and the corresponding wavelengths are on the scale of 1mm, which allows the imaging of body tissues [1]. If we go even further to a nanoscale system and hypersound regime (10^2~10^7MHz), the propagating motion becomes lattice vibrations, which are referred to as thermal phonons, the effective wavelength is then of the atomic scale. This lattice vibration is important to the heat transfer in crystalline solids [2,3]. Mechanical

waves are thus prevalent in our everyday life as well as engineering applications, which makes the control of mechanical waves a significant research of field.

In macroscopic system, conventional methods of controlling mechanical waves and vibrations include viscous dampers, dissipative foams, tuned mass dampers, and active control loops [4]. Meanwhile, the design of artificial materials with structural periodicity and discreteness is proposed as an alternative method, which enables a greater degree of control over mechanical waves [2,5,6]. Briefly speaking, when the unit of a periodic structure has a similar dimension to the wavelength, this structure will influence the wave propagation and therefore modulate the wave.

Recently, the wave phenomenon and the potential of wave manipulation in granular materials have become a rich and rapidly developing research of field. A type of granular materials consisting of closely packed array of particles are frequently referred to as granular crystals (Figure 1.1). Due to their structural simplicity and flexibility, granular crystals have become an ideal test bed for probing the physics of wave phenomena in granular materials and exploring the possibility of wave modulation. The abundance of wave behaviors in granular crystals is another reason why they have attracted so much attention. And it originates in the nonlinear dynamic response. Nonlinearity is intrinsic to granular crystals: on the one aspect, the wave propagation in granular crystals are essentially supported by the Hertzian contact between neighboring elastic particles and that interparticle contact is nonlinear [7]; on the other aspect, granular crystals under uncompressed state cannot support tensile loads and thus the potential between neighboring granules is asymmetric [5,8]. The even more interesting characteristic of granular crystals is that their nonlinear responses are tunable by adjusting the static pre-compression or the dynamic excitation applied to the system. In consequence, granular crystals can exhibit diverse dynamic response encompassing linear, weakly nonlinear and strongly nonlinear regimes [9].

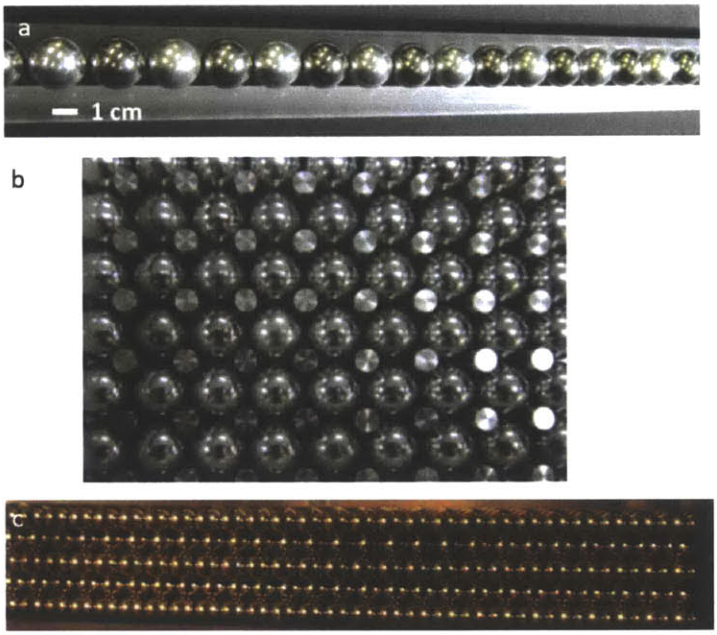

Figure 1.1 Examples of one-, two-, and three-dimensional granular crystals composed by metallic particles. (a) 1D diatomic granular crystal; (b) 2D closely-packed granular crystal confined in a matrix; (c) three dimensional granular crystal (adapted from Dr. Vincent Tournat's website http://perso.univ-lemans.fr/~vtournat/index.html).

The wave modulation in granular crystals has wide application potentials including the vibration/shock absorbers [10–12], actuators [13], sound focusing devices [14], etc. By designing the structure of granular system and including more physics elements into system, granular crystals can present even more complicated functions and become promising engineering devices. Boechler et al. proposed a one-dimensional granular crystal, which took advantage of the interplay of periodicity, nonlinearity and asymmetry in the granular crystal structure to realize functions of rapid switching and rectification. This result is applicable to the design of AND and OR logic gates or even to biomedical applications [15].

Despite of those developments, the modulation of mechanical waves with high frequencies (~100MHz) is rarely explored in granular system or other systems. The majority of studies about controlling mechanical waves are limited within the low frequency (~10 kHz) whereas devices,

such as surface acoustic wave filters for automotive electronics and remote control, have working frequencies on the scale of 100MHz [9]. The constraint in frequency is mainly caused by the system dimension. As mentioned previously, the frequency of a mechanical wave is inversely proportional to its wavelength. When artificial structure has a large dimension, it is too large to detect the propagating vibration or influence the wave with a high frequency and a small wavelength. The reported granular crystals are typically composed of macroscopic particles with dimensions of $0.1\text{mm} - 1\text{mm}$, which confines the wave modulation in a low frequency range.

Scaling down the granular system is a possible solution to achieving the modulation of high frequency waves. However, results of the study on macroscopic systems cannot be directly applied to the wave modulation in microscopic systems. As a system is scaled down, the physics can be qualitatively changed. For a granular system, the adhesive contact between particles and the substrate becomes a significant physical mechanism on a micron scale whereas it is negligible on a millimeter scale. The adhesive contact can connect microparticles and the substrate like an elastic spring. Accordingly, microparticles can oscillate on the substrate in a very similar way to spring oscillators. Several different "contact resonance" modes including rocking [16], axial [17] and lateral [17,18] vibrations, have been observed in experiment.

It has also been validated that as the dimension of particles goes to the micron scale, the corresponding resonant frequency can reach $\sim$100MHz, which is rightly the frequency regime we aim to extend the wave modulation to. Therefore we propose to take advantage of the contact resonance to realize the wave modulation at high frequencies. The mechanical contact between particles and the substrate is a surface interaction and decays exponentially as going downward into the bulk. The microparticle oscillation therefore is expected to influence surface waves only rather than bulk waves. In a solid medium, one type of surface elastic waves, usually called surface

acoustic waves (SAWs), can propagate. Thus in this thesis, we propose to modulate SAWs in the granular crystals. We have established a two-dimensional granular crystal system composed of closely packed microparticle arrays deposited on a substrate (Figure 1.2). As SAWs with wavelengths on the micron scale are excited, the contact resonance of microparticles are initiated as well. The contact between particles and the substrate is able to change the boundary condition of SAWs efficiently and therefore modulate the wave behavior. Since the contact resonance takes place at a high frequency (~100MHz), a strong hybridization between the contact resonance and SAWs as well as a modulated wave behavior are expected around that high frequency accordingly.

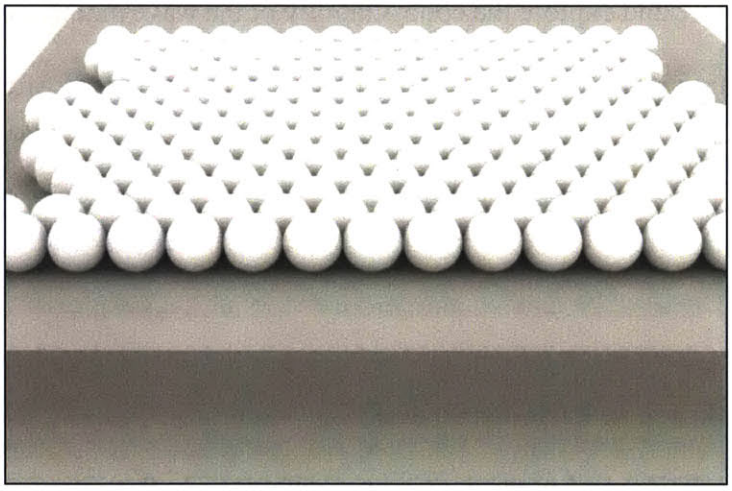

Figure1.2 The schematic illustration of the granular crystal system proposed to modulate SAWs. The system is composed of a closely packed two-dimensional monolayer of particles placed on an infinitely large flat substrate surface.

Although the coupling between SAWs and contact resonance of particles has been explored theoretically [19,20] and the experimental work on the modulation of SAW via phononic crystals has been reported [21], neither the physics of SAW propagation nor the wave modulation via the mechanical contact in a granular system has been analyzed in a systematic way. Meanwhile, the study on complicated SAW phenomena and the manipulation over SAWs are of great significance

in engineering applications. After the development of interdigital transducers (IDTs) which extended the frequency of SAWs to ultrasound regime and shrank their wavelengths accordingly, SAWs were widely applied for signal processing in tiny devices such as delay lines, resonators, convolvers and high-frequency filters [3]. Thus our study on the modulation of SAWs may have an impact on the development of signal processing devices as well.

In this project, both theoretical and experimental results are presented for understanding the novel wave phenomena in the microscopic granular system and exploring its applications in wave modulation. We first present a systematic analysis on the mechanism of the wave modulation in granular structure and explore the controllability of the wave modulation. We are also concerned with the application potential of the microscopic granular structure. After the analysis on wave modulation in the structure shown in Figure 1.2, we continue to design a granular SAW waveguide to demonstrate the application potential of granular materials in SAW-based devices.

1.2 Wave Modulation in Periodic Structure

The modulation and control of wave behavior via the interaction between the periodic structure and the wave is a universal concept in various fields of research. The design of artificial periodic structures for an increased ability to manipulate waves has become an intensively explored research topic. Especially in optics and acoustics, different concepts and mechanisms of wave modulation in periodic structure have been proposed. Metamaterials and photonic/phononic crystals are most well-known examples, which make use of the structural periodicity and discreteness to support wave phenomena not encountered in conventional materials [22,23].

The core idea of metamaterial is to do the bottom-up design of "artificial atoms" so that those structure units finally constitute a new material with unusual yet desirable wave properties. In general, metamaterials utilize the effective medium theory----the material as a whole is effectively homogeneous and fully described by effective parameters; the detailed structure of each artificial atom is invisible to the wave given that the scale of structure unit is much smaller than the wavelength [24]. After Pendry provided a feasible solution for realizing the metamaterial with negative refractive index experimentally [25], a research enthusiasm for metamaterial was aroused, which was thirty years after it was first proposed[3]. Shelby et al. then provided the first experimental verification of negative index of refraction [26]. In addition to negative refraction, the development of transformation optics [27] [28] enabled metamaterials to modulate effective parameters and control waves. The concept of metamaterials have also extended to mechanical waves. In 2000, the first experimental demonstration of sonic crystals with negative effective density was reported [29].

Photonic crystal is another intensively-researched concept for wave modulation. Photonic crystals are in general periodic nanostructures with a period on the same scale as the wavelength. The way that photonic crystals influence the motion of photons and manipulate photonic waves is an analogy of how crystal lattices of solids influence the motion of electrons. The concept of photonic crystals can date back to 1887 and it was boosted by the development of photonic band theory [30] and got another rapid growth after the first experimental demonstration in 1996 [31]. Phononic crystals as the counterpart of photonic crystals in acoustics, have also developed and demonstrated the manipulation of acoustic waves [23]. In essence, heat is a mechanical wave at a very high frequency. Phononic crystals on the nanoscale have been designed for the control of heat flow [6] as well.

This thesis will focus on the realization of high-frequency modulation of mechanical waves in a microscopic granular system. Although most studies in macroscopic granular systems focus on the tunable nonlinearity and the associated abundant wave behaviors, the mechanics involved in this thesis is still in the linear regime. The manipulation ability over mechanical waves at high frequencies are expected to be expanded dramatically after introducing the nonlinearity to the system. Therefore the nonlinear effect is one important content of our future work. In this project the mechanical wave we aim to modulate is SAW. There are also reports on the novel behavior of SAWs generated by using phononic structures such as phononic crystals [21,32–36]. Similar to studies on photonic/phononic crystals in other wave systems, those reported works focus on the band structure generated by phononic crystals. Recently, Yudistira et al. demonstrated a full SAW band gap in a two-dimensional honeycomb array via both theoretical analysis and experiment. Their microscale phononic crystal is able to generate a band gap around 100MHz [36], which again validates the necessity of scaling down the system to realize the high-frequency modulation. The manipulation of SAWs for practical applications including the subwavelength imaging has also been demonstrated by using phononic crystals [35].

1.3 Conceptual Organization of Thesis

In the remainder of this thesis, we will first present the theoretical analysis on the SAW modulation via microscopic granular materials in chapter 2. This part includes the detailed analysis on the mechanical contact between particles and the substrate, an introduction on SAWs which we aim to modulate, and the derivation of dispersion properties of SAWs in our microscopic granular crystal. In the end of Chapter 2 we also propose a design of SAW Luneburg lens, where gradient index for SAWs is realized by manipulating the structure of granular crystals. This Luneburg lens

structure is able to realize the aberration-free imaging or apply to the shock wave absorption. This content is provided to demonstrate the feasibility and variety in the application of granular crystals to SAW manipulation.

One challenge of this project is the fabrication of large-sized granular crystal composed of microscopic structure unit. In chapter 3 we introduce a self-assembly technique to fabricate the microscopic granular samples. Not only the detailed experimental operation but also a systematic analysis on the assembly mechanism are provided for the robust fabrication result.

In chapter 4 we introduce the technique applied to measuring the dispersion property of SAWs in the granular crystal system. In our experiment, we implement the laser-induced transient grating technique to excite SAWs on the substrate. The short laser pulses are used to produce broadband SAWs, which are often used in materials science [3].The measurement results and the corresponding discussions on different types of samples are presented.

After the study on SAW behaviors in granular crystal, in chapter 5 we explore the application potential of the granular crystal in wave manipulation. We have designed a granular-crystal-based SAW waveguide, which is a strip deposition of microsparticle array on the bare substrate. The theoretical analysis on waveguide mode, the fabrication of patterned granular structure and measurement results are included in this chapter.

Chapter 2 Theoretical Analysis on SAWs in Granular Materials

As proposed in Chapter 1, we expect to modulate SAWs at high frequencies in a granular system by making use of the mechanical contact between particles and the substrate. As shown in Figure 1.2, the proposed granular system is composed of a rigid flat substrate, which can be treated as infinitely large, and a monolayer of closely packed microscale particles with a hexagonal symmetry. Particles and the substrate are able to interact with each other via Hertzian contact. On the one aspect, SAWs can induce the motion of particles: as a SAW propagates on the medium, it leads to a displacement of substrate surface, which then changes Hertzian contact between substrate and particles and excites the particle oscillation. In return, the motion of particles changes the boundary condition of SAW and modulates its propagation property. Given that the dimension of particles is on the micro scale, the frequency of particle oscillation and the wave modulation is expected to reach ~100MHz.

In this chapter, an introduction to the Hertzian contact between substrate and microparticles will be discussed in 2.1. We review modeling theorems for Hertzian contact and determine the most suitable model, which is then applied to the analysis on particle oscillation in 2.2. In 2.3 we will introduce the property of unmodulated SAW by deriving its dispersion equation. In 2.4 the result from 2.1-2.2 (about the Hertzian contact) and that from 2.3 (about SAW property) will be combined to analyze the wave behavior in our granular system. In 2.5 we discuss in detail on the modulation of wave behavior via controlling several parameters including the particle dimension, work of adhesion, and the unit cell dimension. The result from 2.5 will help understand the mechanism of wave modulation and also enable the controllability of wave modulation. In 2.6 we

propose a design of Luneburg lens for SAWs as a demonstration of applying the granular-material-based structure to controlling wave propagation.

2.1 Contact Mechanics

The study on contact mechanics between curved surfaces can date back to Hertz' paper "on the contact of elastic solids" in 1882 [7,37]. In Hertz' model, the mechanical contact is associated with a deformation of contacting surfaces. Also it is required that the deformation is small with respect to the dimension of contacting bodies. In this model, the adhesive interaction such as van de Waals force is not taken into account.

The latterly-developed JKR theorem considers the adhesive interaction and therefore in JKR model contacting surfaces are attractive to each other. However, only the interaction within the contact area is considered. Outside of contact area, the interaction is neglected. By contrast, another model, DMT theorem involves the long-ranged interactions outside of the contact zone, the van de Waals, for instance. A qualitative statement of the difference between JKR and DMT is as follows: JKR predicts the separation of two surfaces to take place with a finite contact area whereas DMT predicts the separation at point contact, namely a zero contact area. The quantitative criterion which is adopted to determine the contact model was first proposed by Tabor [38]. Tabor defined a dimensionless parameter, the ratio of contacting surfaces' separation h outside of the contact area to the interatomic spacing z_0, which was referred to as Tabor ratio afterwards. Muller gave a more systematic analysis on the Tabor ratio and formulated it by the expression [39–41]:

$$\mu = \frac{32}{3\pi}\left(\frac{2R^{*}w^{2}}{\pi E^{*2}{z_0}^{3}}\right)^{\frac{1}{3}} \tag{2.1}$$

where R^* is the combined radius of contacting surfaces, E^* is the combined elastic modulus, and w is the adhesion work.

The combined radius satisfies ${R^*}^{-1} = {R_1}^{-1} + R_2^{-1}$, where R_1, R_2 are radii of curvature for the two contacting surfaces. In our system, it is the surface of a spherical particle with a radius R contacting with a flat substrate with an infinitely large radius of curvature. Thus $R_1 = R, R_2 = \infty$ and $R^* = R$. The combined elastic modulus is defined by the expression [40]

$$E^* = [(\frac{1-{\nu_p}^2}{E_p}) + (\frac{1-{\nu_1}^2}{E_1})]^{-1} \tag{2.2}$$

where E_p, ν_p are elastic modulus and Poisson's ratio of particles, E_1, ν_1 are for the substrate.

z_0 in equation (2.1) is the atom-atom distance. $z_0 = 0.4\text{nm}$ is a good estimation for the system of silica particles contacting with an oxidized aluminum layer [42].

The value of adhesion work w can be derived from Hamaker constant A_{12} according to [42]

$$w = \frac{A_{12}}{12\pi {D_0}^2} \tag{2.3}$$

where $D_0$is the interfacial contact separation and it is substantially smaller than the interatomic spacing z_0. Here we set $D_0 = \frac{z_0}{2.5} \approx 0.165nm$, which is a standard value used for the interfacial cut-off separation distance for various media [42]. The Hamaker constant for two macroscopic phases 1 and 2 in the medium 3 can be approximated to

$$A_{12} \approx \frac{3}{4}kT\left(\frac{\varepsilon_1-\varepsilon_3}{\varepsilon_1+\varepsilon_3}\right)\left(\frac{\varepsilon_2-\varepsilon_3}{\varepsilon_2+\varepsilon_3}\right) + \frac{3h\nu_e}{8\sqrt{2}} \frac{({n_1}^2-{n_3}^2)({n_2}^2-{n_3}^2)}{({n_1}^2+{n_3}^2)^{1/2}({n_2}^2+{n_3}^2)^{1/2}[({n_1}^2+{n_3}^2)^{1/2}+({n_2}^2+{n_3}^2)^{1/2}]} \tag{2.4}$$

Now we can calculate the value of Tabor ratio μ by plugging derived parameters above into (2.1). In our experiment system, the substrate is a glass slide with a 100nm-thick aluminum

coating on the surface. Particles which directly contact the aluminum coating have a radius of $R = 504\text{nm}$. Thus $R^* = 504\text{nm}$. The elastic modulus and the Poisson's ratio of aluminum are $E_1 = 62\text{GPa}$, $\nu_1 = 0.24$ [43] and those of silica microparticles are $E_p = 73\text{GPa}$, $\nu_p = 0.17$ [44]. Plug them into equation (2.2) we get the combined elastic modulus $E^* = 35\text{GPa}$.

A note here is although the surface of the aluminum coating is very likely to be oxidized to alumina, the elastic modulus and the Poisson's ratio are still determined by the main constituent of the whole aluminum layer. As a result, we use the values of elastic modulus and Poisson's ratio for aluminum instead of alumina in the above calculation. Yet properties associated with the contacting surface are determined by the surface material, namely alumina. We will use parameters for alumina when analyzing those properties. This point is rightly taken care of in the following calculation of Hamaker constant A_{12}.

For our system, phase 1 in equation (2.4) is the surface material. As mentioned above, it is alumina given the oxidization of the aluminum coating. Phase 2 is silica, the material of microparticles and Phase 3 is air. The environment temperature is T=293K. $\varepsilon_1 = 11\text{F/m}$, $\varepsilon_2 = 3.8\text{F/m}$, and $\varepsilon_3 = 1.0\text{F/m}$ are permittivity of the three phases. $n_1 = 1.75$, $n_2 = 1.45, and\ n_3 = 1.00$ are their refractive indices. ν_e is the main electron absorption frequency in the UV and according to [42], $\nu_e = 3.2 \times 10^{15}\text{Hz}$. Plug those values into (2.4), we get $A_{12} \approx 9.6 \times 10^{-20}\text{J}$. From equation (2.3) we can finally obtain $w = 0.094\text{J/m}^2$.

With all the variables ready, we plug them in (2.1) and obtain $\mu = 1.1$. In general, $\mu \to \infty$ indicates the JKR theorem applies whereas $\mu \to 0$ indicates that interactive forces outside of the contact area are not negligible and the DMT theorem is more suitable. As for $\mu = 1.1$ DMT theorem is a better choice. In addition, JKR theorem is a better approximation for soft and large

contacting bodies. DMT theorem is usually applied for solid and small bodies, which is namely the case in our system. Thus our further analysis on mechanical contact is based on DMT [39–41].

2.2 Contact Resonance

Particles can interact with the substrate via Hertzian contact. That interaction plays such an important role in the microscopic system that enables a contact resonance of particles. Different linear and nonlinear oscillation modes have been theoretically analyzed or experimentally observed [16–18,46]. In this section we focus on the linear axial vibration.

One frequently-used strategy to analyze the contact resonance is to model the contact as a linear spring. Then the motion of a particle in the vertical direction is simply a spring oscillator (Figure 2.1), which can be fully described by the spring constant and the particle mass.

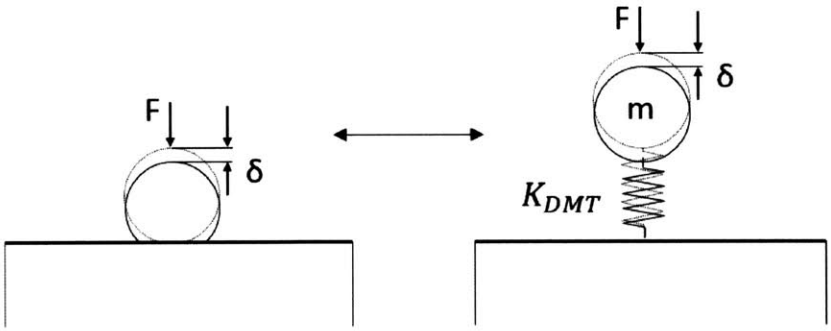

Figure 2.1 The mechanical contact (left) can be modeled as a spring oscillator (right). Due to the adhesive contact force F, the particle is deformed and the deformation can be quantified by the penetration depth δ. The oscillating particle then is modeled as a spring oscillator. K_{DMT} is the effective spring constant, the value of which can be derived from DMT model.

The spring constant can be derived from the differentiation of the attractive contact force F respect to the penetration depth δ at the equilibrium position. Formulations for the relation

between F and δ are different in different theoretical models. As we have determined to use DMT theorem according to Tabor ratio calculated in 2.1, we employ the formulation in DMT theorem, which is expressed as

$$F_{DMT} = \frac{Ka^3}{R} - 2\pi wR \tag{2.5}$$

where K is the equivalent modulus $K = \frac{4}{3}[(\frac{1-{\nu_p}^2}{E_p}) + (\frac{1-{\nu_1}^2}{E_1})]^{-1} = \frac{4}{3}E^*$, which is 47GPa in our system; a is the radius of the contact area; and the work of adhesion $w = 0.094\text{J/m}^2$.

For the computation of spring constant, we need to replace a with the penetration depth δ at first. According to the Hertzian contact profile, we have [40,41,47]

$$\delta(a) = \frac{a^2}{R} \tag{2.6}$$

where R is the radius of the particle. This equivalence relation is valid in DMT as well [41] [47].

Plug (2.6) into (2.5):

$$F_{DMT} = KR^{1/2}\delta^{3/2} - 2\pi wR \tag{2.7}$$

Therefore at the equilibrium state where $F_{DMT} = 0$, we can get the equilibrium displacement

$$\delta_0 = \left(\frac{2\pi wR^{1/2}}{K}\right)^{2/3} \tag{2.8}$$

According to the definition, spring constant is then

$$K_{2,DMT} = \frac{\partial F_{DMT}}{\partial \delta}|_{\delta_0} = \frac{3}{2}(2\pi wR^2K^2)^{1/3} \tag{2.9}$$

Plugging parameter values into (2.9), we obtain $K_{2,DMT} = 1.1\text{kN/m}$.

To calculate the resonant frequencyf_0, we first compute the mass of microparticle. Given the density of particle $\rho_p = 2.0 \times 10^3 \text{kg/m}^3$ we get

$m = \frac{4}{3}\pi\rho_p R^3 = 1.32 \times 10^{-15}\text{kg}$. Accordingly we obtain

$$f_0 = \frac{1}{2\pi}\sqrt{\frac{K_{2,DMT}}{m}} = 144\text{MHz}. \tag{2.10}$$

We can also estimate the equilibrium displacement δ_0 of the particle, which can be used to examine the validity of a linear dynamic model. Latterly we will estimate the displacement of substrate surface from the experimental data. If this estimated displacement is small enough in comparison with δ_0, the linear model is then proved to be valid. With variables we have computed, we can estimate δ_0 from (2.8), which is

$\delta_0 = 0.44\text{nm}$.

2.3 Unmodulated Rayleigh Wave on Bare Substrate

The excitation technique used in our experiment can excite both SAW and bulk waves including the longitudinal wave and the transverse wave. Due to the symmetric configuration of the excitation setup, SAWs in our system are Rayleigh waves. Rayleigh wave was first predicted by Lord Rayleigh in 1885. It travels along the medium surface and decays exponentially in the bulk. The Rayleigh wave has both transverse and longitudinal components, which share a phase difference [46].

In this section the theoretical analysis on the unmodulated Rayleigh wave propagating in a bare substrate will be given. The substrate in our system is a glass slide coated with a thin

aluminum layer. At this moment, we take it as granted that the aluminum coating will not influence the SAW propagation and therefore we treat the substrate as a pure glass slide. In this way the analysis process will be simplified. Later we will give computation result to prove this treatment is a reasonable approximation for our system.

2.3.1 Dispersion Equation of Rayleigh Wave

First, we set up the coordinate for the wave analysis. As illustrated in Figure 2.2, x axis is the propagating direction of wave; z axis points upwards from the substrate. The surface wave decays along the $-z$ direction. Rayleigh wave is uniform along y direction. Therefore our system is two-dimensional.

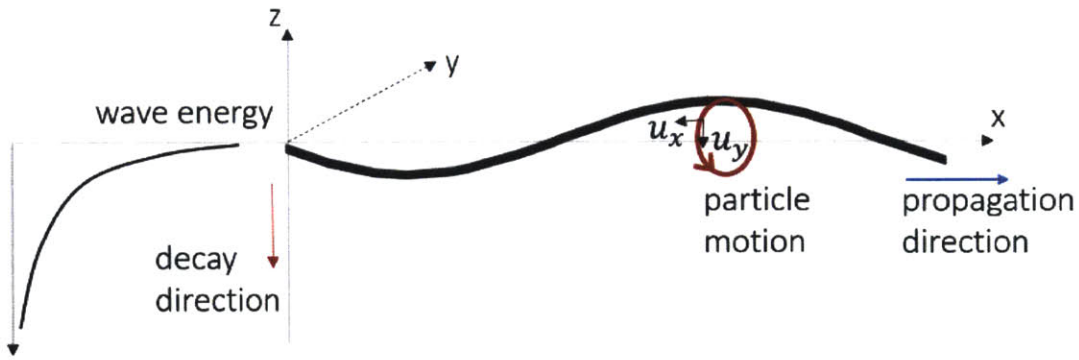

Figure 2.2 The schematic illustration of the Rayleigh wave system. The wave is propagating along x axis and the wave energy decays as going downwards to the substrate bulk. The path of particle indicates both the vertical and the horizontal motions.

The wave function can be expressed by the derivative of the wave potentials as below [46]:

$$u_x = \frac{\partial \varphi}{\partial x} - \frac{\partial \psi}{\partial z}, u_z = \frac{\partial \varphi}{\partial z} + \frac{\partial \psi}{\partial x} \tag{2.11}$$

φ *and* ψ are wave potentials for longitudinal and transverse wave components, respectively. They satisfy:

$$\nabla^2\varphi - \frac{1}{{c_L}^2}\frac{\partial^2\varphi}{\partial t^2} = 0,\ \nabla^2\psi - \frac{1}{{c_T}^2}\frac{\partial^2\psi}{\partial t^2} = 0 \tag{2.12}$$

where $c_L\ and\ c_T$ are the longitudinal wave speed and the transverse wave speed. Considering the decay behavior of the wave in z direction, wave potentials are formulated as:

$$\varphi = Aexp[i(\omega t - kx) - \nu z], \tag{2.13}$$

$$\psi = Bexp[i(\omega t - kx) - \nu' z],$$

where k is the wave vector in x direction; ν, ν' are decay constants for the longitudinal and transverse wave components. k, ω, ν, ν' satisfy

$$k^2 - \frac{\omega^2}{{c_L}^2} = \nu^2,\ k^2 - \frac{\omega^2}{{c_T}^2} = {\nu'}^2. \tag{2.14}$$

On the free surface of the substrate where $z = 0$, boundary conditions are:

$$\sigma_{zz} = 0, \sigma_{xz} = 0 \tag{2.15}$$

According to the isotropic Hooke's law and the strain-displacement relation, the boundary conditions can be reformulated into equations below:

$$\sigma_{zz} = \lambda\varepsilon_{xx} + \lambda\varepsilon_{yy} + (2\mu + \lambda)\varepsilon_{zz} = \lambda\frac{\partial u_x}{\partial x} + (2\mu + \lambda)\frac{\partial u_z}{\partial z} = 0, \tag{2.16}$$

$$\sigma_{xz} = 2\mu\varepsilon_{xz} = \mu\frac{\partial u_x}{\partial z} + \mu\frac{\partial u_z}{\partial x} = 0,$$

where $\lambda\ and\ \mu$ are Lame's constants. They can be related to wave speeds by equations below:

$$2\mu + \lambda = \rho{c_L}^2,\ \mu = \rho{c_T}^2. \tag{2.17}$$

where ρ is the density of medium.

Combining (2.11), (2.13-2.17) we get:

$$\left(2-\frac{\omega^2}{k^2{c_T}^2}\right)A-2\sqrt{\frac{\omega^2}{k^2{c_T}^2}-1}B=0, \tag{2.18}$$

$$2\sqrt{\frac{\omega^2}{k^2{c_L}^2}-1}A+\left(2-\frac{\omega^2}{k^2{c_T}^2}\right)B=0.$$

In order to get non-zero values of A, B, the coefficient matrix of equation (2.18) should have a zero determinant, namely

$$\begin{vmatrix}\left(2-\frac{\omega^2}{k^2{c_T}^2}\right) & -2\sqrt{\frac{\omega^2}{k^2{c_T}^2}-1}\\ 2\sqrt{\frac{\omega^2}{k^2{c_L}^2}-1} & \left(2-\frac{\omega^2}{k^2{c_T}^2}\right)\end{vmatrix}=0. \tag{2.19}$$

After simplification, the dispersion equation for Rayleigh wave is obtained:

$$(2-\frac{\omega^2}{k^2{c_T}^2})^2-4\left(1-\frac{\omega^2}{k^2{c_L}^2}\right)^{\frac{1}{2}}\left(1-\frac{\omega^2}{k^2{c_T}^2}\right)^{\frac{1}{2}}=0. \tag{2.20}$$

In our experimental system, the substrate is a glass slide with a very thin aluminum layer. At this moment we neglect the influence aluminum layer as mentioned previously. For the float glass, $c_L = 5640\text{m/s}, c_T = 3280\text{m/s}$ [48], and $\rho = 2.32\times10^3\text{kg/m}^3$. Plugging those values into equation (2.20) we can get the dispersion curve shown in Figure 2.3. Clearly, the dispersion relation of unmodulated Rayleigh wave is almost linear. The approximated Rayleigh wave speed can be derived from a linear fitting $c_R \cong \frac{\omega}{k}$, and the fitting result is $c_R = 3013\text{m/s}$, slightly smaller than the transverse bulk wave speed $c_T = 3280\text{m/s}$. As indicated by (2.20), $c_R \approx \frac{\omega}{k}$ cannot be larger than c_T otherwise the term $\left(1-\frac{\omega^2}{k^2{c_T}^2}\right)^{\frac{1}{2}}$ in (2.20) will be imaginary.

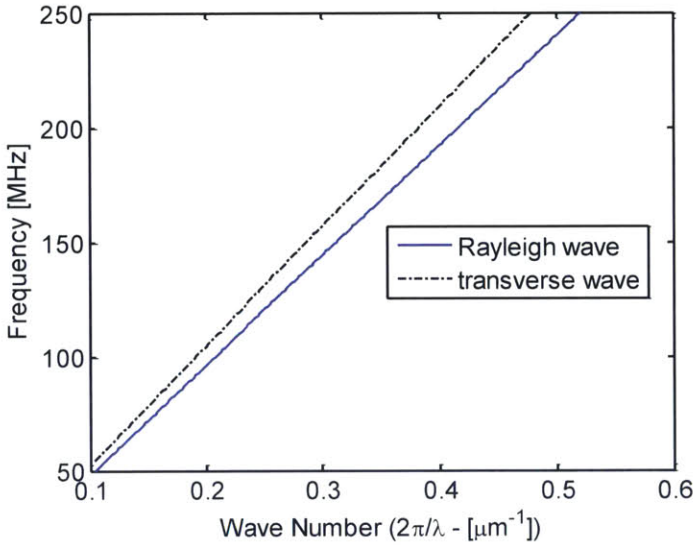

Figure 2.3 The dispersion curve of the unmodulated Rayleigh wave on bare glass slide. Solid blue line is for Rayleigh wave. The dispersion of bulk transverse wave is also plotted in dashed black line as a comparison.

2.3.2 Influence of Thin Metal Coating

The aluminum coating is required by the SAW measurement. However, it is not desirable if the metal coating influences the wave propagation. Now we solve the wave equation of a layered structure and revisit boundary conditions to analyze the influence of the metal layer on the Rayleigh wave.

Figure 2.4 The model for the wave analysis in a layered structure composed of a glass slide substrate (Phase I) and a thin aluminum coating (Phase II).

The structure of the system is shown in Figure 2.4. Phase I is the aluminum coating with a thickness of h. For aluminum, speed of longitudinal wave $c_{L_1} = 6420\text{m/s}$, speed of transverse wave $c_{T_1} = 3040\text{m/s}$ [48], and mass density $\rho_1 = 2.7 \times 10^3\text{kg/m}^3$. Phase II is the glass slide. $c_{L_2} = 5640\text{m/s}, c_{T_2} = 3280\text{m/s}$ and $\rho_2 = 2.32 \times 10^3\text{kg/m}^3$.

Wave potentials for the two phases are expressed as below:

$$\varphi_1 = Aexp[i(\omega t - kx) + \nu_1 z] + Bexp[i(\omega t - kx) - \nu_1 z], \tag{2.21}$$

$$\psi_1 = Cexp[i(\omega t - kx) + \nu_1' z] + Dexp[i(\omega t - kx) - \nu_1' z],$$

$$\varphi_2 = Eexp[i(\omega t - kx) - \nu_1 z],$$

$$\psi_2 = Fexp[i(\omega t - kx) - \nu_1' z],$$

where φ_1, ψ_1 are longitudinal and transverse wave potentials of phase I (aluminum coating) and φ_2, ψ_2 are of phase II (glass substrate).

At the free surface where $z = h$, boundary conditions are the same as those for the bare substrate without coating, namely (2.15):

$$\sigma_{zz_1} = 0, \sigma_{xz_1} = 0. \tag{2.22}$$

At the interface between two phases where $z = 0$, boundary conditions are:

$$u_{x_1} = u_{x_2},\ u_{z_1} = u_{z_2},\ \sigma_{zz_1} = \sigma_{zz_2},\ \sigma_{zx_1} = \sigma_{zx_2}. \tag{2.23}$$

We plug the expression of wave function as formulated by (2.21) into (2.22) and (2.23) and get six equations for the six unknown coefficients A, B, C, D, E, F. Again in order to get a nontrivial solution, the coefficient matrix is set to have a zero determinant. By solving the equation derived from zero determinant, we can get the dispersion equation for the layered structure. In Figure 2.5,

the vertical axis is the ratio of the wave number of layered structure $k_{layered}$ to that of the bare substrate k_{bare}. It clearly illustrates that the thin layer of aluminum can result in an increase of wave number and the increase gets more obvious as the wave frequency increases. However, the difference is negligible. As the frequency reaches 1200MHz, the wave number change is still less than 0.1%. In this way, we have proved the validity of neglecting the existence of aluminum coating. In the following discussion, we will still neglect the aluminum coating and treat the substrate as a pure glass slide.

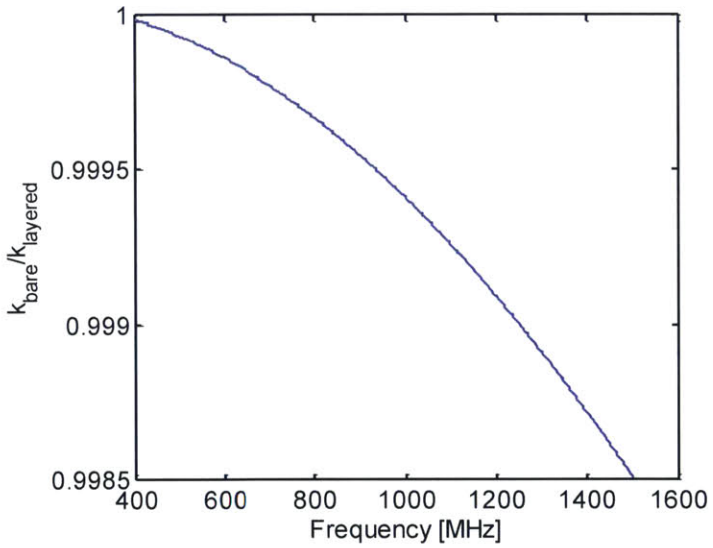

Figure 2.5 The ratio of wave numbers for the Rayleigh wave in the bare substrate k_{bare} and the Rayleigh wave in the layered structure system $k_{layered}$.

2.4 Hybridized Rayleigh Wave

The mechanical contact results in the contact resonance of microparticles and we have derived the resonance frequency in 2.2. This mechanical contact can change boundary conditions on substrate surface and influence the wave propagation as well. We expect to make use of this mechanical contact to couple the particle oscillation with SAW and modulate the wave behavior.

Our granular system is a substrate coated by a closely packed monolayer of microparticles. The schematic illustration of the wave modulation is shown in Figure 2.6. In this section we will derive the dispersion equation of Rayleigh wave modulated by the granular crystal coating.

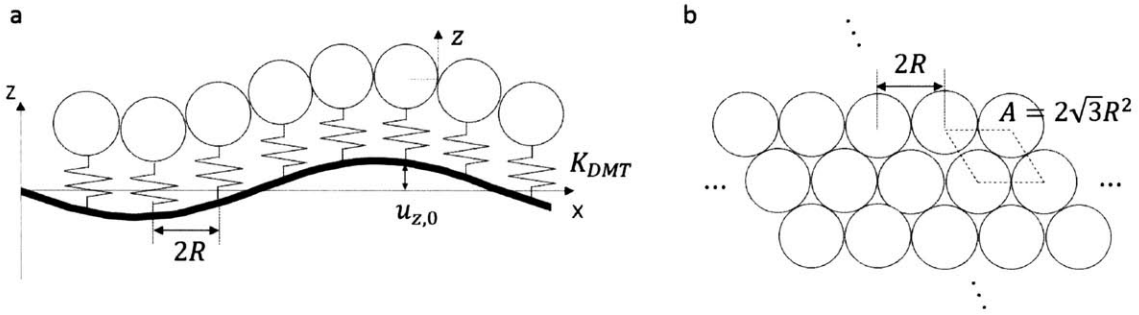

Figure 2.6 Schematic illustration of the SAW modulation via microsphere granular crystal. (a) The cross-sectional view where interactions between microparticle monolayer and the substrate is modeled as spring forces; (b) the top view of granular structure. A unit cell is marked by the dashed parallelogram.

In 2.2 we modeled the mechanical contact as a linear spring with a spring constant $K_{2,DMT}$. From the perspective of particles, the force imposed on them is

$$F_p = -K_{2,DMT}(z - u_{z,0}), \tag{2.24}$$

where z is the displacement of a particle and $u_{z,0}$ is the vertical displacement of the substrate surface rightly underneath this particle (therefore $u_{z,0} \equiv u_z|_{z=0}$) and thus $z - u_{z,0}$ is the deformation of the spring.

Once the particle oscillation is coupled with the wave propagation, the former will have the same frequency as the latter. Then the particle displacement is formulated into:

$$z = z_0 \exp(i\omega t). \tag{2.25}$$

Then we plug $F_p = m\ddot{z}$ and (2.25) into (2.24) and obtain

$$z = \frac{K_{2,DMT}}{K_{2,DMT} - m\omega^2} u_{z,0} \tag{2.26}$$

Now we define a parameter $\alpha = \frac{z}{u_{z,0}} = \frac{K_{2,DMT}}{K_{2,DMT} - m\omega^2}$, namely the ratio of vertical displacement between particles and the substrate surface. Then we can rewrite (2.26) into

$$z = \alpha u_{z,0} = \alpha\left(\frac{\partial \varphi}{\partial z} + \frac{\partial \psi}{\partial x}\right). \tag{2.27}$$

where the second equality is due to (2.11).

The spring force is exerted on the substrate as well and points to the opposite direction to F_p:

$$F_s = -F_p = K_{2,DMT}\left(z - u_{z,0}\right). \tag{2.28}$$

To be accurate, the force F_s is imposed on the tiny contact area between one particle and the substrate. Given the equation (2.6), we can get the contact area is $A_c = \pi\delta R$. In Hertzian contact the deformation is very small and the penetration satisfies $\delta \ll R$, therefore we have $A_c \ll A = 2\sqrt{3}R^2$, which is the cross-sectional area of a unit structure of the granular crystal (Figure 2.6.b). Based on this scaling relation, an important treatment, "effective medium approximation" is applicable. When the wave length scale is substantially larger than that of the unit cell, the detailed structure of a unit cell becomes unobservable to the wave. Then the composite medium can be treated as continuum and be described by averaged properties and parameters. In our case, the wavelength of SAW is no shorter than $7\mu m$. The wavelength of such scale can guarantee that the change of structure and force in the small contact area A_c of each unit cell A is undetectable. Therefore we implement the effective medium approximation and average the spring force over the whole unit cell area A. The force is then reformulated into an average pressure:

$$P_{ext} = \frac{F_S \cdot \boldsymbol{n}}{A}, \tag{2.29}$$

where $\boldsymbol{n}$ is the normal vector on the substrate surface and in our case $\boldsymbol{n}$ is along the $-z$ direction.

Accordingly, the boundary condition (2.15) is modified to

$$\sigma_{zz} = P_{ext}, \sigma_{xz} = 0.$$

Considering (2.24-2.28), we can get:

$$\sigma_{zz} = -\frac{K_{2,DMT}(\alpha-1)u_{z,0}}{2\sqrt{3}R^2}, \sigma_{xz} = 0. \tag{2.30}$$

Then we plug (2.13) - (2.17) into the updated boundary conditions (2.30), the new coefficient matrix is obtained:

$$\begin{vmatrix} 2{c_T}^2k^2\rho_2 - \rho_2\omega^2 - \frac{K_{2,DMT}(\alpha-1)\sqrt{3k^2-3\frac{\omega^2}{{c_L}^2}}}{6R^2} & 2{c_T}^2k^2\rho_2\sqrt{k^2-\frac{\omega^2}{{c_T}^2}}j - \frac{\sqrt{3}K_{2,DMT}(\alpha-1)kj}{6R^2} \\ 2{c_T}^2k^2\rho_2\sqrt{k^2-\frac{\omega^2}{{c_L}^2}}j & -{c_T}^2(2k^2-\frac{\omega^2}{{c_T}^2}) \end{vmatrix}.$$

Similarly, the determinant of this matrix has to be zero. By simplifying the corresponding equation, we have derived the dispersion equation:

$$(2-\frac{\omega^2}{k^2{C_T}^2})^2 - 4\left(1-\frac{\omega^2}{k^2{C_L}^2}\right)^{\frac{1}{2}}\left(1-\frac{\omega^2}{k^2{C_T}^2}\right)^{\frac{1}{2}} = \frac{m}{A\rho_2}\frac{\omega^4\left(1-\frac{\omega^2}{k^2{C_L}^2}\right)^{\frac{1}{2}}}{k^3{C_T}^4}\frac{1}{\left(\frac{\omega^2}{{\omega_0}^2}-1\right)}, \tag{2.31}$$

where $\omega_0 = \sqrt{\frac{K_{2,DMT}}{m}}$ is the angular frequency of microparticle's contact resonance. And we have obtained from (2.10) $f_0 = \omega_0/2\pi = 144\text{MHz}$.

The dispersion curve is shown in Figure 2.7. Around the resonant frequency f_0 no motion mode exists, which is a classic "avoided crossing" phenomenon and usually induced by strong hybridization. In our case, it is due to the hybridization between particle oscillation and Rayleigh wave. The lower branch of dispersion curves starts from the Rayleigh wave mode with low wave vector magnitudes. Then it approaches the horizontal asymptote corresponding to the resonant frequency f_0. As the wave vector magnitude increases, the upper branch behaves more similar to Rayleigh wave. Close to the "avoided-crossing" region, the upper branch deviates from Rayleigh-wave-like mode and stops at the threshold corresponding to the bulk transverse acoustic wave. This is consistent with the dispersion equation (2.31): we can see that the phase velocity $\frac{\omega}{k}$ has to be smaller than the transverse wave velocity c_T, otherwise the term $\left(1-\frac{\omega^2}{k^2{c_T}^2}\right)^{\frac{1}{2}}$ on the left hand side will become an imaginary number.

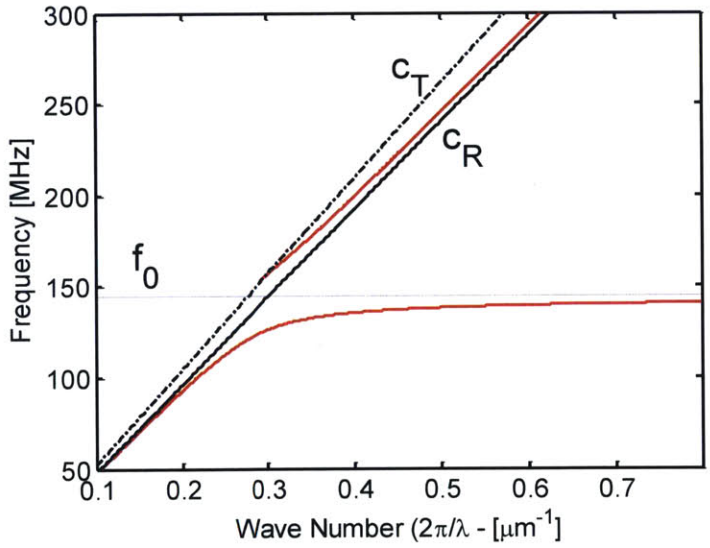

Figure 2.7 Dispersion relation. Red curves are the dispersion for the modified Rayleigh wave. The curves for the normal Rayleigh wave (solid black line) and for the bulk transverse wave (dashed black line) are also plotted as a comparison. The resonant frequency f_0 is indicated by the horizontal dashed blue line, around which the "avoided crossing" takes place.

A comparison between (2.31) and (2.20) indicates that the coupling between particle motion and SAW only results in a change of the right hand side (RHS) term of the dispersion equation. We then define the RHS term as "coupling strength", which quantifies the interaction strength of SAW and particle oscillation. The larger the value of this term, the stronger the coupling effect is expected. A sanity test is that when the coupling strength is made to vanish (for example, particles are nearly massless or particle coating is so sparse that the area of unit cell A becomes nearly infinitely large, the system is no different from the bare substrate case), the dispersion spectrum will recover to Rayleigh wave equation (2.20). Obviously, the coupling strength is adjustable by changing m, A, ρ_2. Meanwhile, the resonant frequency can be modulated by changing $m, K_{2,DMT}$. As illustrated by the dispersion curve (Figure 2.7), characteristics of the modulated Rayleigh wave can be fully described by the resonant frequency and the coupling strength. Thus we expect to design and control SAW propagation via the modulation of resonant frequency and coupling strength. This idea is to be elaborated in the following section.

2.5 Modulation of SAW in Micro/Nanoparticle-Based Granular Materials

As mentioned, the coupling strength and the frequency of avoided-crossing can be modulated by various parameters such as particle density and unit cell dimension. In our proposed system, the significant wave modulation takes place around the resonant frequency of contact resonance. If we define this resonant frequency f_0 as a functional frequency, then the ability to modulate $f_0$will enable devices satisfying different frequency needs. In general, coupling strength of a large value is preferred. A larger coupling strength will result in a more obvious and smoother bending in the avoided-crossing region and significantly slow down the velocity of wave, which

is desired in the signal-processing-related operation. Here we use numerical computation to analyze the influence of different parameters including the particle dimension, work of adhesion, and the unit cell on the wave behavior.

2.5.1 Particle Dimension

The particle dimension is quantified by particle radius R. First, let's exam its influence on the resonant frequency $f_0 = \frac{1}{2\pi}\sqrt{\frac{K_{2,DMT}}{m}}$. The equation (2.9) indicates that the spring constant $K_{2,DMT} \sim R^{\frac{2}{3}}$. Meanwhile, the particle mass $m \sim R^3$. Then we can get $f_0 \sim R^{-7/6}$.

Now we focus on the coupling strength term, which is $\frac{m}{A\rho_2}\frac{\omega^4\left(1-\frac{\omega^2}{k^2{c_L}^2}\right)^{\frac{1}{2}}}{k^3{c_T}^4}\frac{1}{\left(\frac{\omega^2}{{\omega_0}^2}-1\right)}$. Around the resonant frequency, we use the approximation $k \approx \frac{1}{c_R}\omega_0$. Due to $m \sim R^3$, $A \sim R^2$ and $\omega_0 \sim R^{-\frac{7}{6}}$, we get the coupling strength is proportional to $R^{-\frac{1}{6}}$. Although it is a rough estimation, we can still obtain the idea that the smaller particles will result in a slightly stronger coupling strength. The difference in coupling strength can be reflected by the bending in the avoided-crossing region and the splitting distance, which is the frequency gap between the lower branch and the upper branch around the avoided-crossing.

In chapter 3 we are going to introduce the experiment result with two different sized particles, one with $R = 504\text{nm}$ and the other with $R = 259.5\text{nm}$. Here we use the analytical result (2.30) to do the numerical computation at first and compare the dispersion curves for those two different particle dimensions. The result is shown in Figure 2.8. The resonant frequency is

obviously raised from 144MHz to 339MHz as the particle dimension is scaled down. Besides, the result for smaller particles has a smoother bending and a larger frequency gap in the splitting position, both of which indicate a stronger coupling strength.

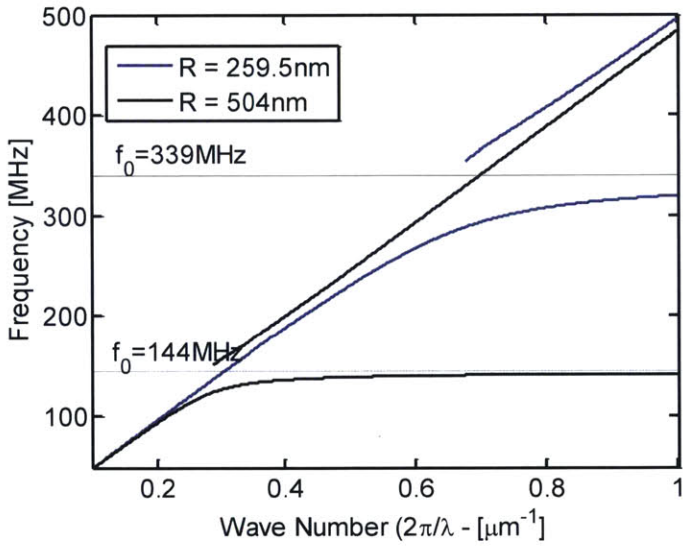

Figure 2.8 Dispersion curve for particle monolayer with different sizes. The blue solid curve is for particles with $R = 259.5\text{nm}$ whereas the black solid curve is for particles with $R = 504\text{nm}$. The dashed lines denote the resonant frequencies for those two different particle monolayers.

2.5.2 Adhesion Work

From (2.9) we know the spring constant $K_{2,DMT}$ relates to the work of adhesion w. Therefore the resonance frequency f_0 can be modulated by w. Since the coupling strength contains $\omega_0 = 2\pi f_0$, it can be adjusted by changing w as well. Changing materials of contacting surfaces is a fast way to modulate w. There are two noteworthy points.

A. In the contact mechanics only the surface material matters and the material of bulk does not have direct influence. Therefore in practical operation, we may not need to change the whole substrate or use particles of completely different material. Alternatively, we can coat the substrate or particles with desired materials to change the surface properties. Another advantage of changing

surface properties in this way is all the volumetric properties such as the bulk wave speed and the particle mass will not be changed.

B. Other properties associated with mechanical contact such as the equivalent modulus involved in equation (2.9-2.10) will also be changed when surface coatings are changed. It makes the estimation of the scaling relation between work of adhesion and resonant frequency/coupling strength impossible.

Thus here we give an example of changed contacting surface and use the computed dispersion curves to demonstrate the influence of w on wave behavior. In this example, we assume a silver coating is applied to both the substrate and particles. The value of adhesion work w is derived from the Hamaker constant in literature [49]. The result is shown in Figure 2.9. In this specific case, work of adhesion $w = 0.372\mathrm{J/m^2}$ and the resonant frequency is improved to $f_0 = 261\mathrm{MHz}$. The larger f_0 also results in a stronger coupling strength, a smoother bending and a larger frequency gap in the splitting regime. As a comparison, we also plot the result for the original contacting case in Figure 2.9.

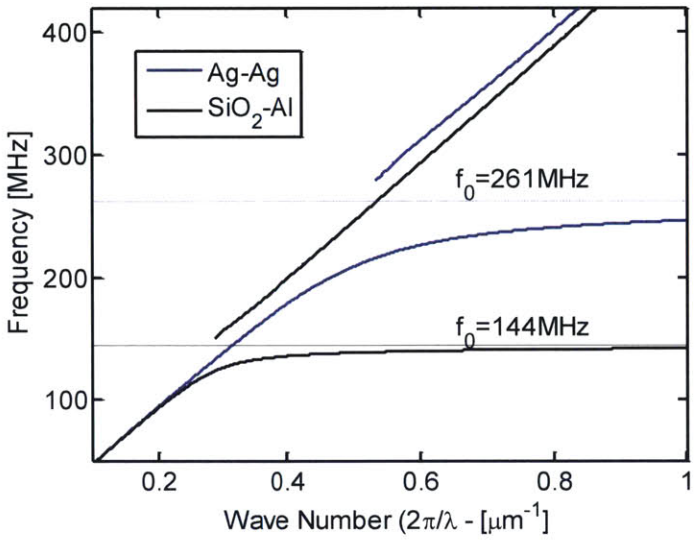

Figure 2.9 Dispersion relations for different combinations of contacting surfaces. The blue solid curve is for the silver-coated substrate contacting with silver-coated particle. The black line is for the aluminum-coated substrate contacting with silica particles. The dashed lines denote the resonant frequencies for the two cases.

The result in this section indicates that we can modulate the work of adhesion by applying different coatings to the substrate or particles to adjust the wave modulation. However, when doing this we should examine whether other mechanical properties, the equivalent modulus, for example, are influenced by the coating.

2.5.3 Unit Cell Area

Different from the particle dimension or the adhesion work discussed above, the unit cell dimension can change the coupling strength without influencing the resonant frequency at all. The unit cell is defined as a parallelogram illustrated in Figure 2.10 with an area $A = 2\sqrt{3}R^2$. A can be adjusted by changing the distance between neighboring particles, namely D denoted in Figure 2.10. We reformulate A in to $A = \frac{1}{2}\sqrt{3}D^2$ accordingly.

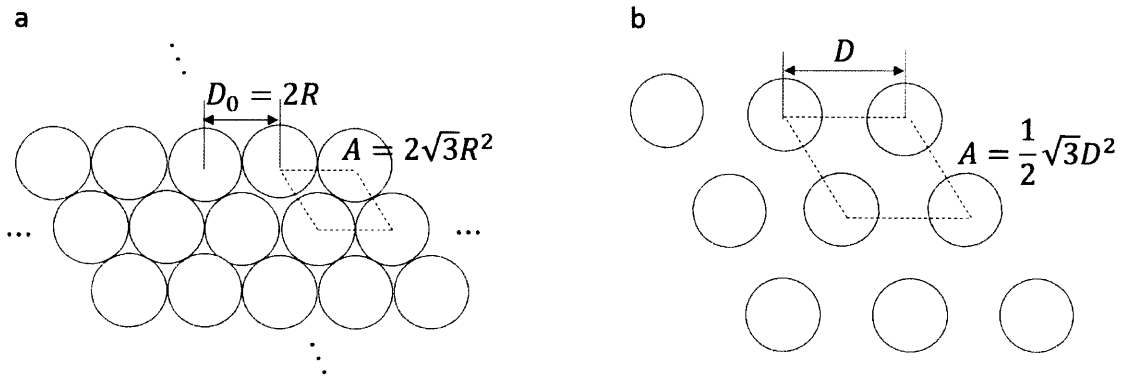

Figure 2.10 (a) Illustration of unit cell for a closely packed structure, where the distance between neighboring particles is $D_0 = 2R$. (b) By changing the distance D between particles the unit cell area A can be adjusted.

Given $A \sim D^2$ and the coupling strengh$\sim A^{-1}$, the increase of D will decrease the coupling strength. In Figure 2.11 we show the comparison between structures with different values of D. As expected, the two cases have the same resonant frequency f_0 and the structure with a larger $D = 2D_0$ renders a sharper bending around f_0. Referring to the concept of "refractive index" in optics, an effective refractive index can also be defined for SAW in our granular system, which is the ratio between a standard wave velocity to the velocity in granular structure. Here the velocity is phase velocity of waves, the same as the definition in optics. We can observe clearly from Figure 2.11 that the phase velocity $\frac{\omega}{k}$ decreases or the refractive index increases as D decreases, namely the structure gets more compacted. Therefore the change of D is an effective method to modulate the refractive index of Rayleigh wave around f_0. Based on this ability to modulate refractive index, we expect to observe more interesting phenomenon by using the microparticle-based granular structure and we are going to give an example demonstration in the following section. In addition to the phase velocity, the group velocity is also influenced by D. As shown in Figure 2.11, the gradients of dispersion curves around f_0 are also different for those two structure with different

unit cell areas. The structure with larger neighboring particle distance D has a sharper gradient $\frac{d\omega}{dk}$, indicating a faster group velocity.

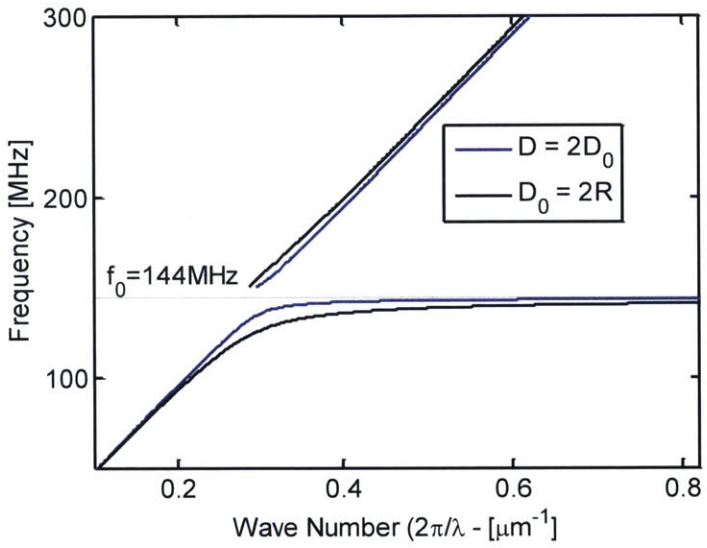

Figure 2.11 Dispersion relations for structures with different unit cell areas or different distances between neighboring particles. The solid blue curve corresponds to $D = 2D_0$ whereas the black solid curve to $D_0 = 2R$. The dispersions share a common resonant frequency f_0.

2.6 Granular Luneburg Lens Structure

2.6.1 Introduction

The gradient-index materials have attracted lots of research interests in areas including optics and acoustics because of various application possibilities. For example, the Luneburg lens, a structure with radically varying refractive index, can focus light from different directions equally well [50] and enable the aberration-free imaging (Figure 2.12). Luneburg lenses in plasmonics, silicon photonics, and acoustics have been proposed with either continuously-tuned material or discrete shell structure [50–58]. Here we propose a microparticle structure which can function as a SAW Luneburg lens based on the ability to modulate refractive index via adjusting the interparticle distance as discussed previously.

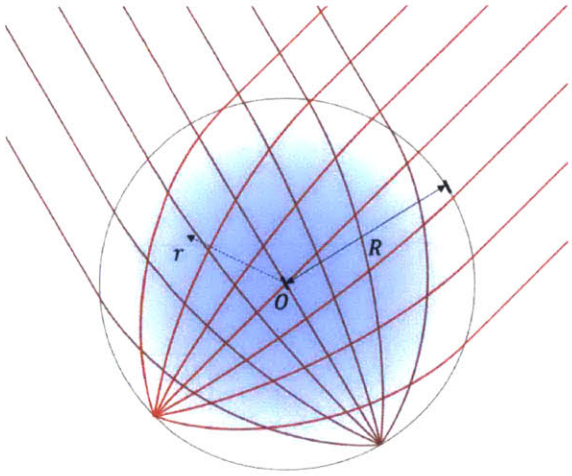

Figure 2.12 Illustration of Luneburg lens structure with a radius of R. The index decreases in the radical direction, at its maximum in the center and at the minimum on the edge. All the parallel incident wave beams can be focused into a spot without aberration.

2.6.2 Luneburg Lens for SAWs

The refractive index n of a Luneburg lens is tuned radially and expressed as

$$n = \sqrt{2 - \left(\frac{r}{R}\right)^2}, \tag{2.32}$$

where R is the radius of the whole lens structure and r is the radial distance from the center of the lens. For SAW on the substrate of glass, if the refractive index is modulated according to the formulation (2.32), the same functionality of Luneburg lens in optics is expected in a SAW system.

The refractive index for a medium is essentially a ratio of a standard phase velocity to the velocity in this medium. Thus the gradient index is equivalent to the gradient phase velocity. As we discussed in section 2.5, all the variables which relate to the coupling strength term such as the substrate density and the particle mass, can influence the profile of dispersion curve and the phase velocity accordingly. However, only the variable A can modulate coupling strength without inducing any influence on the resonant frequency. This property makes the modulation result

neater. In addition, the wave modulation is most effective around the resonance frequency. If we can modulate the coupling strength and keep the resonant frequency unchanged, then we do not need to worry that the shift of resonance frequency makes the wave modulation insignificant. Eventually, keeping the resonance frequency unchanged can help increase the bandwidth of the final Luneburg lens device. Thus we determine to manipulate A rather than other variables to realize the gradient index for SAW.

The area of unit cell A is related to the distance between neighboring particles D as discussed in 2.5.3. We define a dimensionless ratio $D_r = \frac{D}{D_0}$, where $D_0 = 2R$ is the interparticle distance for the closely packed microparticle monolayer. Figure 2.13 shows the relation of phase velocity versus wave number for D_r ranging from 1.0 to 2.0 with a step of 0.125. The phase velocity keeps increasing as D_r increases. A qualitative explanation to this observation is given here: as D_r increases the particle structure becomes sparser, the wave will accordingly behave closer to the normal Rayleigh wave on a bare substrate, whose phase velocity is faster than the modulated wave. One note here is we use the dispersion equation (2.31) to derive the phase velocity for D_r ranging from 1.0 to 2.0. However, we cannot use this method for D_r which is of a very large value. As we discussed before, (2.31) is based on the effective medium approximation, which requires the wavelength to be comparatively larger than the unit cell dimension. As D_r gets larger, this condition cannot be satisfied.

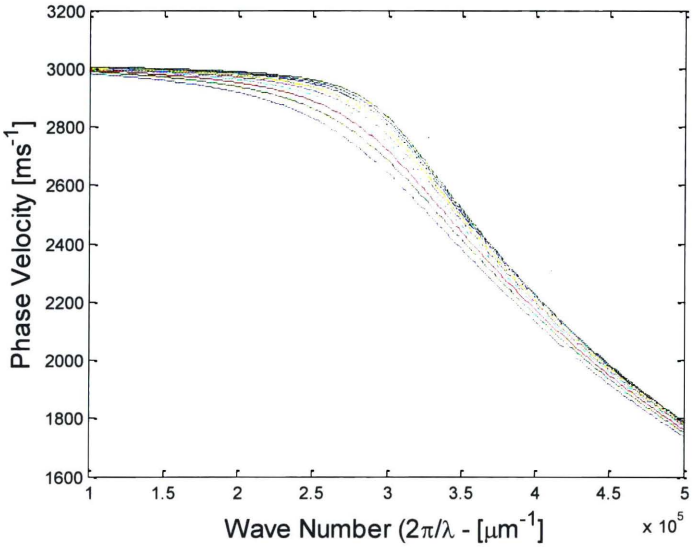

Figure 2.13 The change of phase velocity versus wave number for multiple D_r, which ranges from 1.0 to 2.0 with a step of 0.125.

Then we look back at the index formulation of Luneburg lens (2.32), which indicates that the maximum refractive index is $n_{max} = \sqrt{2}$. From Figure 2.13, we can clearly see that the phase velocity is dependent on the wave number k. We need to find a suitable value of k which can render us an $n_{max} \geq \sqrt{2}$. If we define the standard phase velocity as the wave velocity on the bare substrate, then we can do the numerical computation and find the wave number has to satisfy $k \geq 4\mu m^{-1}$ for $n_{max} \geq \sqrt{2}$. Thus we use the phase velocity at the wave number $k = 4\mu m^{-1}$ to define the refractive index as:

$$n = \frac{phase\ velocity\ on\ bare\ substrate\ |k=4\mu m^{-1}}{phase\ velocity\ on\ granular\ crystal\ structure\ |k=4\mu m^{-1}}.$$

Accordingly, we can get a relation between n and D_r as shown in Figure 2.14. The maximum index $n_{max} = \sqrt{2}$ now corresponds to the closely packed structure with $D_r = 1$. In Figure 2.14 the minimum value of refractive index does not reach 1 as we cannot apply effective medium

approximation to compute refractive index. When $k = 4\mu m^{-1}$, the wavelength is $\lambda \approx 16\mu m$. In order to have the effective medium approximation valid, $D = D_r D_0 \leq \lambda/5$ should be satisfied. It requires $D_r < 3$. Although the computation based on effective medium approximation is impossible here, it is for sure that the index will finally reach 1: when $D_r \to \infty$, the system becomes the bare substrate case and the refractive index equals to 1. The phase velocity and the refractive index for larger D_r may also be obtained via experimental measurement.

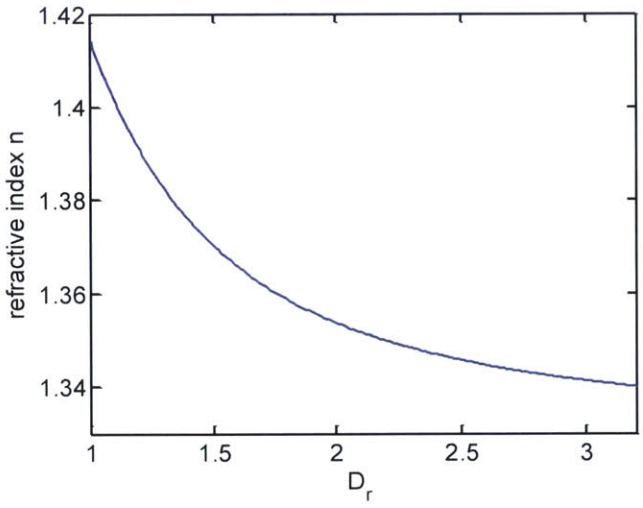

Figure 2.14 Refractive index n versus D_r. The calculation is based on phase velocities of waves corresponding to $k = 4\mu m^{-1}$.

In Figure 2.15 we give a layered structure as a discrete Luneburg lens for SAW. D_r is a constant in each layer. From the innermost layer to the outmost layer, D_r gradually increases for a gradient index as formulated by (2.32). The exact value of D_r in each layer can be calculated according to the refractive index defined before. For example, for the ith layer with a radius r_i, we can plug this radius into (2.32) to get the desired value of n_i. According to Figure 2.14, we can get the value of D_r for this layer. Again, this method is not suitable for the outer layers due to the

limitation of effective medium approximation. Then the relation between refractive index and D_r obtained from experiment may be used.

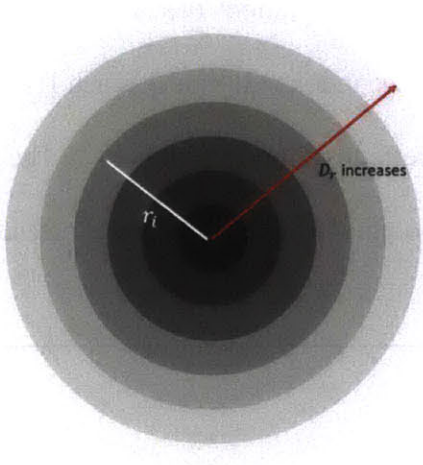

Figure 2.15 The layered structure with varying structure as a discrete version of Luneburg lens for SAWs.

Chapter 3 Fabrication of Monolayered Granular Crystals

3.1 Introduction

One of the challenges encountered with studies on wave phenomenon of microscale granular crystals is sample fabrication. Although complicated micro/nano structures have been produced with the state of art in nanomanufacturing, the fabrication of a granular structure with a large dimension for the experimental analysis as well as a micro/nanoscale resolution is still challenging. Self-assembly technique, an organization process of microscopic elements via the intrinsic interactions in the system, is a possible solution for an efficient and economical fabrication of ordered structure with either monotonous or multiple components. The key mechanism of self-assembly is the interactions among elements. For example, in Langmuir-Blodgett method it is the interactions resulted from surface charge and charge dipole that are manipulated to organize nanoparticles into ordered structure at the medium interface [59–61]. The dielectrophoresis method makes use of the field-dipole interaction and the dipole-dipole interaction to fabricate microsphere monolayer [62].

In this thesis, we are interested in the assembly of micrsoscopic particles into closely packed monolayer structure. The convective self-assembly is one of the most widely employed methods for the assembly of micro/nanostructures. The fabrication of centimeter-sized monolayer of spherical micro/nanoparticles via convective self-assembly has been reported [63–65]. There are several different types of convective self-assembly with different experiment configurations. However, almost all of them share the same fundamental process: first, the evaporation of a thin liquid film leads to the transportation of particles; the limited thickness of this liquid film results

in the deposition of particles into a thin layer [63]; at the liquid-air interface, capillary forces connect particles with each other and assemble them into an ordered array.

One classical setup for the convective self-assembly of microspheres was proposed by Dimitrov and Nagayama [66]. Their setup is composed of a movable substrate along the vertical direction, which can drag the meniscus and enable the deposition of monolayer structure (Figure 3.1.a). At the edge of meniscus, a thin liquid film exists. A convective flow is generated from the bulk reservoir towards the thin film to compensate the liquid loss induced by evaporation. Particles in the liquid are transported altogether with the flow. When approaching the thin film region, they connect with each other into a densely packed array. One drawback of their method is the waste of particle solution----the substrate is dipped into a container of particle solution whereas only a limited amount of particles finally deposit on the substrate. Then a modified setup was proposed by Prevo and Velev [67] (illustrated in Figure 3.1.b). With their method, a much smaller volume of particle solution is confined between two slides. By withdrawing either the substrate or the deposition plate, the meniscus is lengthened and flattened to form a thin film at the front edge of the whole liquid phase.

This modified setup is essentially a flipped version of the previous one. For both of those two setups, if the receding velocity of the meniscus V_m is equal to the growth velocity of the particle array V_{pa} a uniform layer of particles will deposit on the substrate [66]. Since the withdrawal velocity of the deposition plate (in some cases, the substrate instead of the deposition plate is withdrawn) is usually much larger than the receding velocity induced by evaporation, V_m is approximately equivalent to the withdrawal velocity. Therefore in drag methods, the withdrawal velocity is carefully controlled in order to realize $V_m = V_{pa}$ and the monolayer deposition.

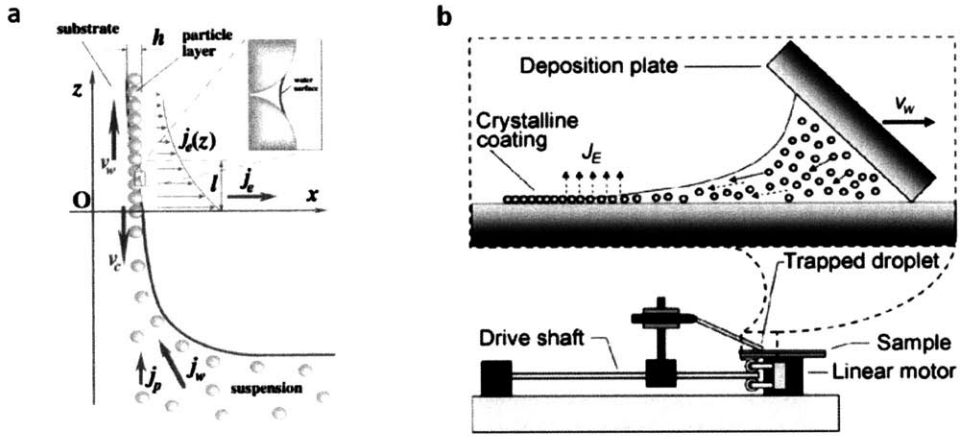

Figure 3.1 (a) Sketch of the particle and water fluxes in the vicinity of monolayer particle arrays growing on a substrate plate that is being withdrawn from a suspension. The inset shows the menisci shape between neighboring particles. Here, V_w is the substrate withdrawal rate, V_c is the array growth rate, j_w is the water influx, j_p is the respective particle influx, j_e is the water evaporation flux, and h is the thickness of the array. Figure is adapted from [66]. (b) The modified convective assembly method. The inset above illustrates the process of convective assembly driven by the evaporation flux, J_E. Figure is adapted from [67].

There is another widely used convective assembly process [64,65,68]. This method is composed of a wedge-shaped cell and it will be referred to as "wedge method" in the discussion later. Particle solution is confined within the wedge cell. A pronounced evaporation around the liquid-air interphase induces an influx which transports particles to the drying front. The contact line, which is the three-phase interface at the drying front of the liquid, can assemble particles into an ordered structure by inducing the immersion capillary force. After the liquid evaporates completely, a centimeter-sized particle array can be deposited (Figure 3.2). It has been proved that the wedge-shaped cell can straighten the contact line whereas other similar setups result in a curved one. The straightened contact line can suppress the polycrystalline and improve the ordering of the assembled structure [64]. It is recently proposed that gravity can contribute to the particle transportation and improve the assembly result in wedge method [65].

In wedge method, a good monolayer structure can be obtained by controlling the solution concentration and humidity. The advantage of wedge method compared with drag method is the simplicity of experiment setup and operation process. The drawback of wedge method is that a much longer time is required to finish the whole assembly process because the receding rate of meniscus in wedge method is completely dependent on evaporation. However, in drag method, the receding motion of meniscus is mainly induced by the withdrawn deposition plate.

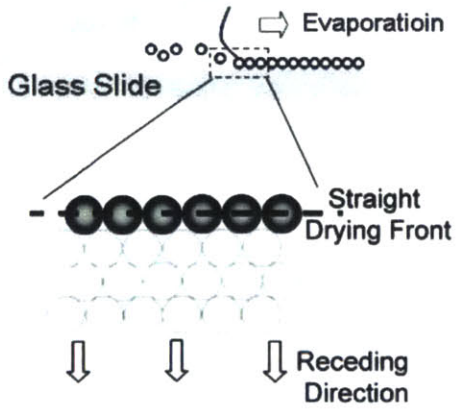

Figure 3.2 Schematic of the convective assembly in a wedge-shaped cell. Figure is adapted from [64].

Considering the robust fabrication result and the simple experiment configuration, we decide to employ the wedge method to prepare the monolayer samples. As mentioned in Chapter 2, we are interested in understanding the influence of various factors, such as the dimension of particles on the modulation of SAWs. Therefore different types of granular crystal samples are in need. The understanding of assembly mechanism will be helpful to the fabrication of different samples for sure. Thus in this chapter, not only the experimental operations but also the mechanism of assembly is to be discussed in a systematic way. At first, the experiment setting will be described. The mechanism of convective assembly by using wedge method will be explored by comparing

our experimental observations and the available theorem. Then influences of experimental conditions such as the concentration of particle solution, the environment humidity, and gravity will be discussed with the support of experimental results. Finally we will conclude the optimized experimental operations and provide the result of fabrication.

3.2 Experiment Setting

The substrates we used for studying assembly mechanism were plain microscope glass slides from VWR International LLC. Glass slides of two different widths were used, one was 25mm wide and the other was 75mm wide. Before the assembly, we cleansed substrates with acetone, then rinsed them with isopropanol and deionized water to remove the organic residues. After that we submerged substrates into a hot bath of 30% hydrogen peroxide (H_2O_2) at 80°C to improve the wetting of substrate surfaces. By adjusting the treatment time of H_2O_2 hot bath, we were able to obtain substrates with different extents of hydrophilicity, which enabled the analysis on the influence of surface wetting on assembly in section 3.4.4. After treatment, substrates were rinsed by deionized water and then dried in the nitrogen flow. The contact angle was measured by goniometer to quantify the wetting property of substrate surfaces. After H_2O_2 treatment for more than 30 minutes the contact angle of water on the glass slide surface was stably below $10°$.

Microparticles/Nanoarticles to be assembled were plain silica spheres from Corpuscular Inc. (www.Microspheres-Nanospheres.com). Two differently sized particles were used. One had a diameter of 1.08μm and the other 519nm. The fabrication processes of monolayer structures composed of these two kinds of particles respectively were completed. The purchased particles were suspended in the water with an original concentration of 5.0wt%, or 50mg/mL. The concentration can be adjusted by adding a certain volume of water or evaporating the liquid. Before

assembly the particle solution was sonicated for one hour in order to have particles distributed in the liquid uniformly.

To build up a wedge-shaped cell, each substrate needs two more glass slides, which are referred to as top slide and bottom slide, respectively. Top slides were all rinsed and treated for hydrophicility with the same method for substrates as described above. One substrate slide was first epoxied on bottom slide (Figure 3.3.a). Then we pipetted a certain volume of particle suspension on the substrate (Figure 3.3.b), quickly mounted a top slide over it (Figure 3.3.c), clamped the top and bottom slides on one edge, and obtained a wedge-shaped cell (Figure 3.3.d). The distance l between one substrate edge to one bottom slide edge was calibrated so that the wedge angle of the assembly cell was 2°(Figure 3.3.a). The wedge cell was put upon a rotatable stage. By rotating the stage, we were able to tilt the wedge cell and analyze the influence of tilting angle δ on the assembly result (Figure 3.3.d).

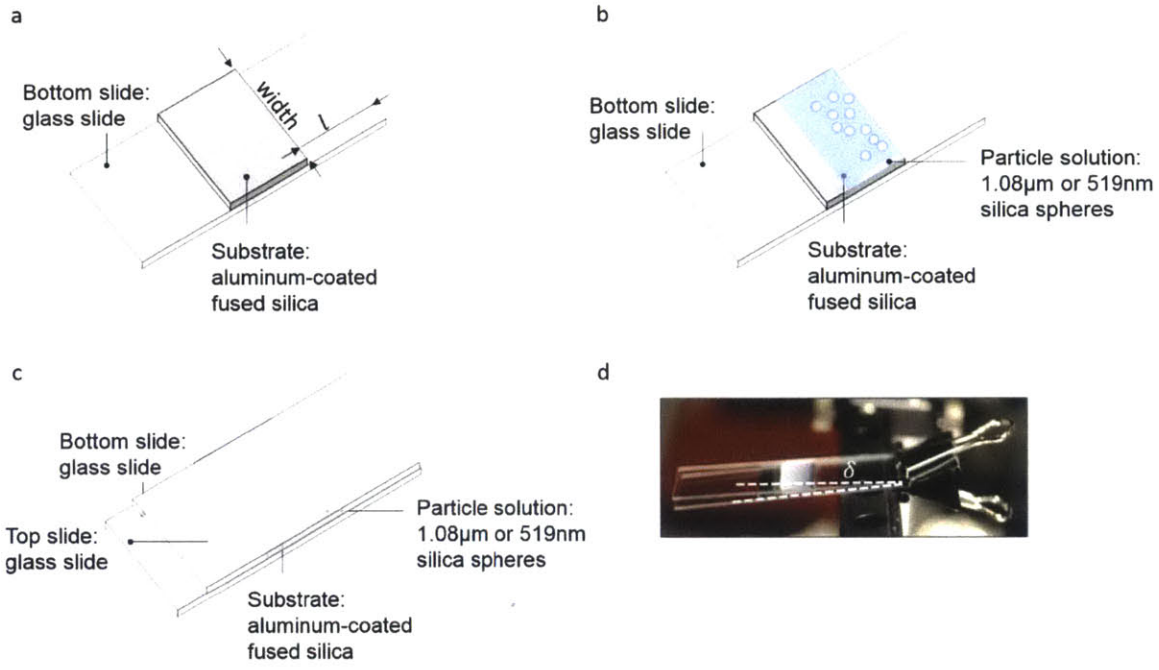

Figure 3.3 Schematic illustration of setting up a wedge-shaped cell. (a) the substrate was epoxied on the bottom slide with a fixed distance l from the edge of bottom slide; (b) a droplet of particle suspension was pipetted on the substrate; (c) the top slide was quickly mounted on the top; (d) photo of the established wedge cell. The whole cell in the photo is tilted downward by angle δ.

A microscope objective lens connected with a CCD, was placed over the wedge cell to observe the motion of particles during assembly. After the liquid evaporated completely, samples composed of 1.08μm diameter spheres were observed directly via a Canon optical microscope. For samples composed of 519nm particles, scanning electron microscopy (SEM) was used for characterization.

After the exploration on the assembly mechanism and the analysis on influential factors in experiment we concluded and optimized the setting of experimental conditions. We then applied the optimized setting to the assembly on substrates with aluminum coating on the surface as required by the measurement technique. Those substrates were glass test slides coated with

100nm-thick bare aluminum purchased from EMF Corporation (EMF AL134). Before assembly, they were also cleansed and treated in H_2O_2 hot bath as introduced above.

3.3 Assembly Mechanism

3.3.1 Developed Theorem and Experimental Observation on Assembly Mechanism

In this section, we will give a general introduction about studies on convective assembly mechanism at first. Then we will analyze the assembly mechanism in our wedge cell system based on the experimental observation. By using scale estimation, we can analyze the dynamics of the assembly process. The comparison between the reported theorem and our analysis will be concluded.

The assembly mechanism of drag method has been systematically studied [66,69–71]. Dimitrov and Nagayama [66] proposed that two processes resulted in the continuous assembly in drag method. The first process is the initiation of assembly. They pointed out the presence of a relatively parallel liquid film in the front of the liquid reservoir is necessary. The pronounced evaporation in the thin film region induces an influx of particles, which enters into the thin film. The film thickness h_f should be slightly smaller than the particle diameter D_p, then particles inside of the film can connect with each other via the immersion capillary force (Figure 3.4). If h_f is obviously smaller than D_p, then particle deposition can never be initiated. The second process is a continuous growth of deposition. The deposited particle array attracts more and more particles via the lateral capillary force. If there are enough particles around the thin film region, a close-packed array will form.

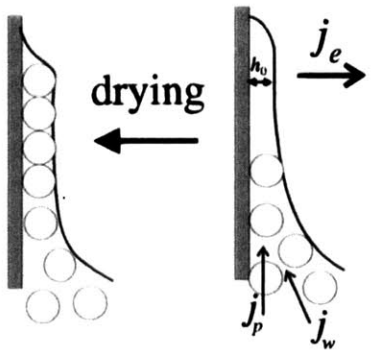

Figure 3.4 Onset of particle array formation in a wetting film. The particle diameter is slightly larger than the thickness h_0. Then, water evaporation from the film causes suspension influx from the bulk toward the film. The monolayer particle arrays are initiated successfully, and their growth can continue. Figure is adapted from [66].

In the drag method the film thickness is adjustable by controlling the withdrawal velocity of the substrate or the deposition plate as we mentioned before. For the modified drag method (shown in Figure 3.1.b), it has been experimentally proved that the increase of withdrawal velocity results in the decrease of thin film thickness h_f [63]. A gradual increase of the withdrawal velocity can lead to the transition of deposition structure from multilayer, monolayer to sub-monolayer [72].

The wedge cell method, in which neither the substrate nor the deposition blade is withdrawn, can be treated as a drag method with a very small receding velocity of the meniscus V_m. The meniscus profile in a wedge-shaped cell has been investigated [73]. A liquid film also exists at the drying front. However, the thickness h_f is on the scale of 10nm. According to [66], the deposition of particles with diameter on the micron scale, which is much larger than the thin film thickness h_f can never deposit. However, by using wedge method the deposition of microparticles have been fabricated successfully. Thus another mechanism which initiates the deposition in wedge cell system should exist. There is a different explanation on the assembly initiation, which does not relate to h_f [72]. This explanation is based on the particle deposition phenomenon in an

evaporating droplet, in which particles at the edge of droplet lead to the pinning of contact line, increase the transportation of particles and enable the continuous deposition of particles along the contact line (Figure 3.5.a). This pinning-induced deposition was then applied to explaining the drag method system which has a setup exactly the same as that shown in Figure 3.1.a. According to [72], the initiation of deposition is owed to the aggregation of particles around the liquid edge and the pinned contact line (Figure 3.5.b).

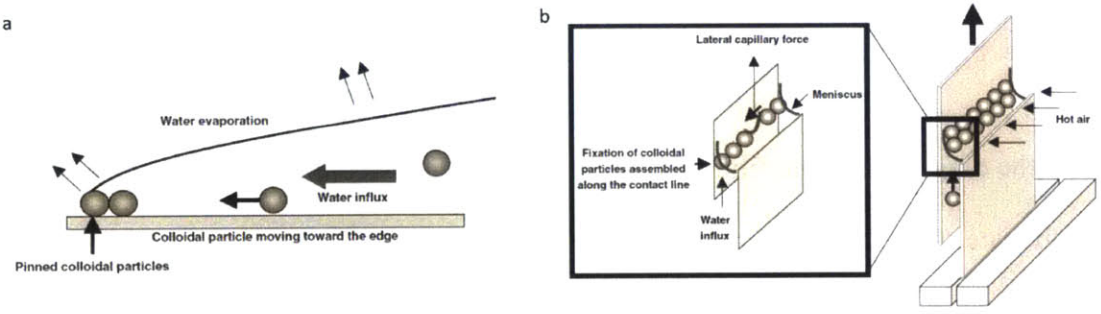

Figure 3.5 a.Schematic illustration of colloidal particles assembling at the meniscus of a colloidal suspension droplet. In the early stage, the colloidal particles assemble into a monolayer. b. The experimental set-up. The magnified image schematically shows the phenomena that occur at the meniscus. Figures are adapted from [72].

This mechanism is possibly applicable to the wedge cell system as well. In order to validate that, we decided to directly monitor the motion of particles during the assembly process and examine whether the pinning of particles and the pinning of contact line take place. The particle motion around the liquid reservoir edge was directly observed and recorded by a 40× objective lens connected to a CCD camera. Relative humidity (RH) was kept at $24 \pm 3\%$. The whole wedge cell was tilted downwards by 10°.

Initially it was observed that particles moved forward towards the edge of liquid reservoir, which was due to the evaporation and the corresponding influx towards the contact line. Then

those particles at the very front were pushed back and a highly-concentrated particle aggregation formed at the edge of cell (Figure 3.6.a-c). The backward motion indicates that those particles at front were encountered with a barrier, which could only be the liquid-air interface. The backward motion also illustrates that the contact line was not pinned at that moment and kept receding. Then the receding liquid-air interface brought particles backward. The combinative effect of this receding contact line and the forward particle flow enabled a rapid aggregation of particles at the drying front. At the state shown in Figure 3.6.c we observed that the front edge of particle aggregation stopped receding and was pinned over there. Therefore the fixation of particles around the contact line region did take place in our wedge cell system. After that particles at the aggregation front gradually moved forward and then organized themselves into a line segment (Figure 3.6.d). Gradually, more particles in the reservoir moved towards the formed line segment and lengthened it. The formed line became a locus which absorbed particles towards itself (Figure 3.6.e). Finally, a long ordered line formed at the reservoir front and the deposition was initiated (Figure 3.6.f). The forward motion observed in the transition from Figure 3.6.c to Figure.3.6.d should be due to the deformation of meniscus profile after evaporation, which could result in a change of the force imposed on particle. More explanation will be given later. The automatic organization of particles into line segment indicates that the capillary interactions exist and proves again those particles at the front were touching the liquid-air interface. Figure 3.6.g-i illustrated the continuous growth of particle array: while the liquid reservoir was moving backwards due to evaporation, a monolayer of particles deposited and covered the substrate. After a continuous deposition of about 0.5cm, the growth of the microsphere monolayer stopped. Particles did not deposit but receded together with the liquid. We could observe that the particle concentration was much smaller than before, which was due to the consumption of particle in deposition. The

deposition was not sharply ended. Instead, a discontinuous deposition took place: the deposition was kept for a short distance about several particle long, paused, and deposited again. The deposited structure was shown in Figure 3.6.j. After the discontinous deposition, particles were confined in the liquid completely and kept receding. No deposition took place any longer.

As shown in Figure 3.6.k-m, the deposition was associated with the existence of a milky line at the front of cell. The milky line indicated an extremely concentrated aggregation of particles. During the complete continuous deposition, the milky line moved backwards as the deposition area increased (Figure 3.6.l). When the deposition ended, we observed that the milky line became much thinner and lighter (Figure 3.6.m), indicating a drop of concentration. This observation indicates the importance of a high concentration of particles in deposition. The observation of milky line has also been reported by Ye et al. [65].

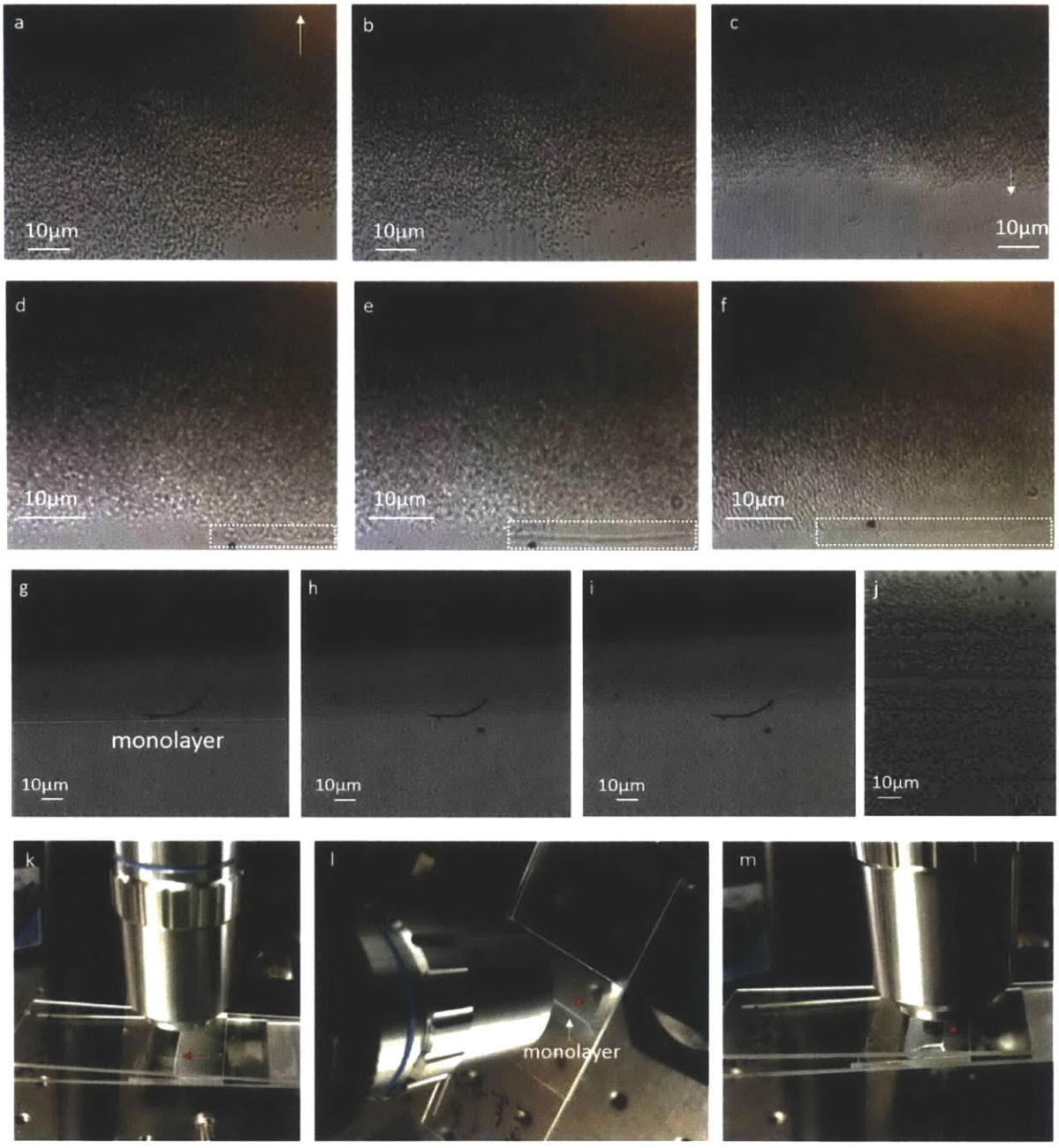

Figure 3.6 (a-b) At the beginning of assembly, particles receded together with the drying front instead of staying on the substrate. No deposition took place during this period. The receding direction was indicated by the white arrow in (a,c). A distinctive edge of particle aggregation formed. Some particles in the front edge moved forward slightly along the direction of the white arrow. (d-e) Particles around the drying front gradually organized themselves into a line segment and then the continuous growth of the microsphere monolayer started. (g-i) A continuous growth of monolayered deposition. The deposited structure was framed by white dotted line. (j) The profile of the discrete deposition at the end of deposition. (k-m) The milky line (denoted by red arrow) changed during the assembly process. (k) The deposition was initiated along with the appearance of a milky line. (l) During the continuous growth of monolayer structure, the milky

line was always there across the drying front. (m) When the deposition ended, the milky line became much thinner than before.

In general our observation was consistent with the mechanism that the pinning of particles and contact line initiated the continuous deposition as proposed in [72]. We are going to analyze the dynamics involved in the deposition initiation and the continuous deposition.

3.3.2 Dynamic Analysis

As we observed in Figure 3.6.a-b, particles were pushing backwards and remained in the liquid at the beginning of assembly. We first analyze the pushing force imposed on particles, which prevents them from depositing.

The profile of the meniscus in a wedge cell is concave, which indicates a pressure drop across the phase interface from air to water [74]. This pressure drop can push particle backwards. Referring to the approximation employed by [75] we model the meniscus as a segment of a circle as shown in Figure 3.7.a. Due to the geometrical relation, the expression for the meniscus' radius of curvature is given by

$$R = \left[\sqrt{\frac{W}{V}\left[\frac{\cos^2\theta}{\tan\left(\frac{\alpha}{2}\right)} - \cos\theta\sin\theta - \frac{\pi}{2} + \theta - \frac{\alpha}{2}\right]}\right]^{-1} \tag{3.2}$$

where W is the width of the substrate, V is the volume of the particle solution confined in the wedge cell, θ is the contact angle of water on the substrate, and α is the wedge angle.

With W= 25mm, $V = 60\mu L$, $\theta = 10°$, $\alpha = 2°$, we can get $R = 210\mu m$. Then pressure drop across the liquid-gas interface is given by

$$\Delta P = \frac{\gamma}{R} = 342 \text{ Pa} \tag{3.3}$$

where $\gamma = 0.072\text{N/m}$ is the surface tension of water. The corresponding backward force generated by ΔP is then

$$F_p = \Delta P A_p \sin\varphi \tag{3.4}$$

where A_p is the projected area of the particle that the pressure drop is imposed on. Another backward force is induced by the surface tension. When one particle touches the liquid-air interface, the interface will be deformed and exerted a backward force on the particle, which can be expressed as

$$F_\gamma \approx 2\pi r^* \gamma \sin\varphi, \tag{3.5}$$

where r^* is the radius of curvature of the deformation. Approximately, $A_p \approx \pi r^{*2}$, therefore we reformulate (3.5) into

$$F_\gamma = 2\sqrt{\pi A_p}\gamma \sin\varphi \tag{3.6}$$

By doing the scaling estimation, we can find $F_\gamma \gg F_p$ and therefore in current discussion we neglect the influence of F_p. Once the liquid interface at the very front has more severe deformation, equations (3.5) become invalid. Also $F_\gamma \gg F_p$ may not stand and we have to take F_p into consideration. This point will be elaborated in our further discussion.

Considering the motion of particles, a forward drag force F_D is also imposed on particles. For the condition of low Reynolds number flow, the drag force satisfies

$$\frac{F_D}{\frac{1}{2}\rho u^2 A_D} = \frac{24}{Re} \tag{3.7}$$

where u is the average flow velocity, $A_D = \pi {r_p}^2$, ρ and μ are density and viscosity of water, and the Reynolds number satisfies $Re = \frac{2\rho u r_p}{\mu}$.

We make the approximation that the receding velocity of particle is constant and then forces have to balance with each other, namely

$$F_\gamma = F_D \tag{3.8}$$

From the geometrical relation, we can get $\varphi = 14°$. For water, $\mu = 8.90 \times 10^{-4}$ Pa · s at 25°C. We have no knowledge of the flow velocity and use u=10μm/s for the scaling estimation. Plugging values of all the parameters into equation (3.8) we can get

$\frac{A_p}{A_D} \sim 10^{-19}$, which indicates F_p, F_γ can exert strong enough backward force on particles even with an extremely small portion of the particle extruding outside of the meniscus. This result is consistent with previous observation (Figure 3.6.a-b). The schematic of the force analysis is shown in Figure 3.7.b.

As the concentration of particles gradually increases, particles at the drying front can be pinned, namely the contact line stopped receding. Once the pinning takes place, the liquid-air interface around the pinning position can be deformed severely due to the evaporation-induced liquid loss. The deformation can change F_γ dramatically as it is associated with the meniscus profile. We do not have knowledge about the exact profile of the deformed interface. In general, the pinning together with evaporation will result in a flattened meniscus and therefore F_γ is smaller than the value estimated from (3.5). The other backward force F_p as we analyzed above, is associated with a more general profile, the circular meniscus of the whole wedge cell. It may not be changed by the local change of meniscus as dramatically as F_γ.

As the deformation appears, one new mechanism exhibits and plays a significant role. It is the immersion capillary force. As shown in Figure 3.7.c, the dark grey particle represents for a particle in the liquid phase coming towards a light gray particle which has been pinned along the contact line. Unless the pinning takes place, particles are completely immersed inside of the liquid phase and the interparticle capillary forces do not exist. A liquid bridge which is represented by a dark blue curve connects them and enables the immersion capillary interaction. The analytical expression for the capillary force between spheres is available only when the distance L between two particles satisfies the conditions below [76]:

$$F_c = -2\pi\gamma Q_1 Q_2 / L, \quad r_p \ll L \ll q^{-1} \tag{3.9}$$

where $Q_i, i = 1,2$ is called "capillary charge" and defined as $Q_i = r_{pi} \sin\psi_i$, r_{pi} is the radius of particle i and ψ_i is the meniscus slope angle at the contact line around this particle; q^{-1} is a characteristic capillary length and for water $q^{-1} = 2.7\ \text{mm}$. In our system when the incoming particle approaches the deposited particle the distance between them cannot satisfy $L \gg r_p$ whereas $L \ll q^{-1}$ is valid. Nevertheless, we still use (3.9) to do the scaling estimation with $L =$ 1μm, which will render an underestimated capillary force. In our system, $r_{p1} = r_{p2} = 0.54\mu\text{m}$. $\psi_1 = \psi_2$ and they are decided by the geometry and the wetting property of particle surface. We set them equal to 20° for the scale estimation. For water $\gamma = 0.072\ \text{N/m}$. Plugging all the parameter values into equation (3.9), we can get

$$F_c \approx 1.5 \times 10^{-8}\ N \tag{3.10}$$

As a comparison, we also do a scaling estimation on F_γ . We do not have the exact expression of F_γ when the interface is deformed severely. So we still use the equation (3.5), which will overestimate F_γ. This time we use a smaller $\varphi = 5°$ considering the flattened meniscus and $r^* =$

0.54μm, which indicates half of the particle extrudes outside of the liquid. According to (3.5) we can get

$$F_\gamma \approx 2 \times 10^{-8}\, N. \tag{3.11}$$

Comparing the underestimated F_c with the overestimated F_γ, we can conclude that the capillary force is very likely to overcome F_γ and enable the deposition once the interface is obviously deformed.

As we discussed previously, F_p is negligible when the contact line is not pinned. However, as the pinning takes place, the role of F_p should be revisited. This time the two opposite effects F_γ and F_c have comparable magnitudes, the force F_p can play an important role in deciding whether particle is able to overcome the constraint of liquid-air interface. We predict that a decrease of this backward effect F_p will help initiate deposition. This prediction has been examined via experiment and we will introduce the result later.

When the interface is deformed even further, the surface tension may generate a force on the particle and pull it forward. The observed forwarding motion in Figure 3.6.d should be contributed by the force change after the interface deformation.

When the three forces F_c, F_γ, F_p are balanced out, a continuous growth of deposition will be achieved as we observed in Figure 3.6.g-i. During this growth process, it is the capillary interactions between particles that result in the ordering of the deposited structure [64] [65].As the deposition continues, the concentration of particles in the liquid decreases. As (3.10) illustrates, the capillary force F_c is dependent on the interparticle distance L, which is dependent on the concentration. A decreased concentration can lead to a too small F_c, which is not able to compete

with the backward forces F_γ and F_p. This analysis can explain our observation: as the deposition continued for a while, the particle concentration obviously decreased and the continuous deposition transitioned to a discontinuous one (Figure 3.6.j).

In conclusion, the analysis above validates that the pinning of particles at the meniscus front initiates the deposition. As the pinning takes place, the deformed liquid-air interface decreases the magnitude of backward force F_γ and exerts a forward capillary force F_c particles. Once the three forces F_γ, F_p and F_c are balanced with each other, a continuous growth of the deposition becomes possible. In the following section, we will analyze a range of influential factors in the assembly process. The analysis result is used to decide an optimized experiment setting for the fabrication of monolayer structures.

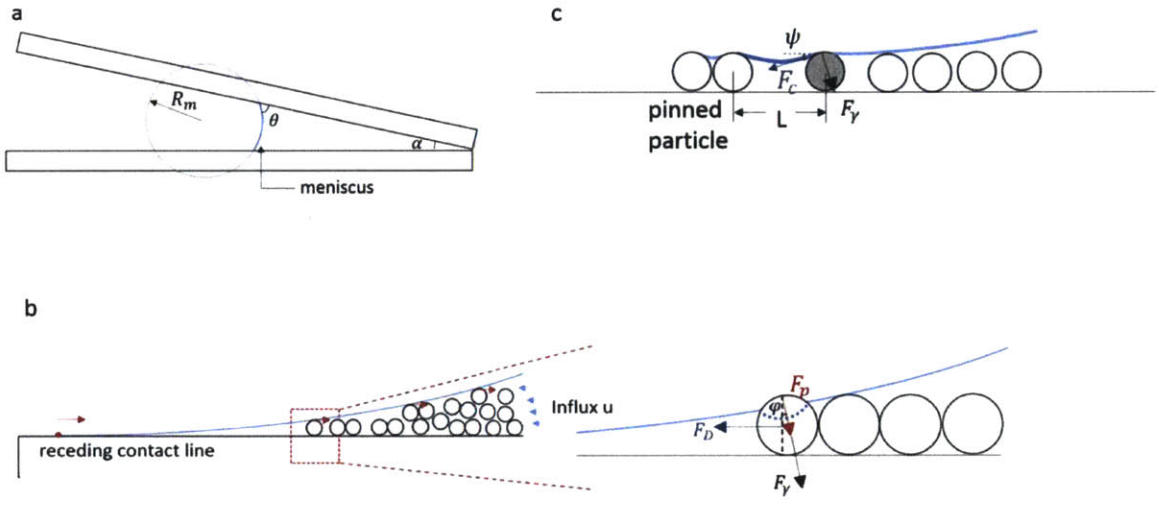

Figure 3.7 (a) The profile of the meniscus is modeled as a circular segment. (b) F_p induced by the pressure difference and F_γ induced by the surface tension push particles adjacent to the contact line backward to the reservoir whereas the influx brings more particles towards the reservoir edge. F_D is the drag force. At this moment, contact line is not pinned and keeps receding. Red arrows represent for the backward forces imposed on particles touching the interface. (c) Immersion capillary force F_c appears as the interface is deformed as the pinning takes place.

3.4 Influential Factors in Fabrication

Based on the assembly mechanism concluded in section 3.3, we analyze influences of several parameters including the particle concentration, geometrical parameters, the relative humidity, gravity and the surface property of substrates on the deposition in this section. All of those influential factors will be examined via experiments.

3.4.1 Particle Concentration

The mechanism that initiates the deposition in our system is the pinning of contact line induced by the aggregation of particles. This is also the mechanism that enables the deposition in an evaporating droplet [77–80]. Studies on the particle deposition in droplet indicate that the high concentration can benefit and maintain the pinning of contact line [78,80,81]. Shen et al. [80] proved in experiment that the high concentration can result in a large diffusion velocity of particles and therefore particles are fast enough to connect with each other, form a layer, and maintain the pinning of contact line. We also expect the high concentration to promote the pinning of contact line and initiate the deposition in the wedge cell system.

First we clarify the definition of concentration here. Conventionally, the concentration quantifies how densely particles are distributed in the whole system. In the wedge cell, this conventional concentration can be defined as the number of particles per unit volume, namely

$$C_1 = \frac{N_p}{V}.$$

where N_p is the total number of particles in the liquid with a volume V.

The concentration that determines the pinning of contact line, is the particle concentration around the contact line. We refer this concentration as C_2. C_2 cannot be adjusted directly, however, it can be easily adjusted by changing C_1. We did two deposition experiments. The only difference

between those two experiments was C_1. In the first experiment $C_1 = 12.5\text{mg/mL}$ and in the second $C_1 = 50\text{mg/mL}$. All the other experimental conditions were kept the same. Liquid volume $V = 60\mu\text{L}$, substrate width $W = 75\text{mm}$, relative humidity (RH) was 24% and the wedge cell was tilted downward with an angle $\delta = 10°$. In the first experiment the deposition was sparse on the substrate, indicating that the concentration of particle aggregation was not high enough across the whole width with $C_1 = 12.5\text{mg/mL}$. Only in several small regions the particle concentration was high enough to initiate the deposition. By contrast, in the second experiment a continuous deposition of monolayer structure was observed (Figure 3.8). The coloring of the monolayer structure in Figure 3.8.b results from the optical diffraction, which is intrinsic to the periodic structure and can be used to help identify the monolayer structure.

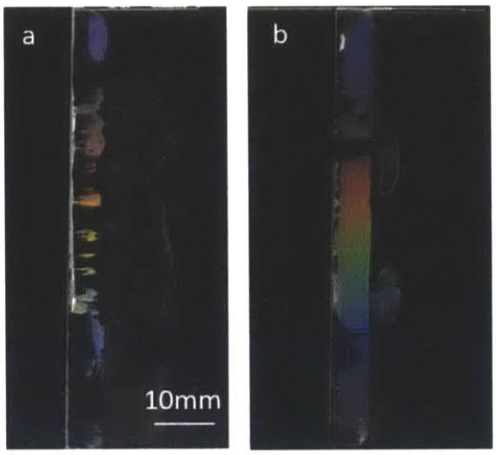

Figure 3.8 In two experiments all the other experimental conditions were kept the same except in (a) $C_1 = 12.5\text{mg/mL}$ whereas in (b) $C_1 = 50\text{mg/mL}$. After deposition finished, we found in (a) particles could not deposit to cover the whole width of the substrate. Instead they only deposited into several small areas. (b) Particles deposit continuously across the whole width of the substrate.

As shown in Figure 3.6.k-m, a milky line formed around the edge of wedge cell whereas the liquid reservoir was transparent, indicating the majority of particles which were distributed in the whole liquid reservoir previously had moved to the limited volume around the contact line.

Thus the number of particles in the milky line region is related to the total number of particles in the liquid, which is equal to $C_1 \times V$. Therefore C_2 is influenced by the liquid volume V as well. The increase of V means a larger total number of particles contained in the liquid phase. As the majority of particles are to be finally transported to the vicinity of contact line, the increase of V will result in an increase in C_2. In addition, particles at the drying front are distributed along the width of substrate W. The effective concentration of particles in the milky line region is then influenced by W as well. For example, if we place two particle solution droplets of the same volume on two substrates with different widths, C_2 corresponding to the wider substrate will be smaller, which may lead to a failure in initiating deposition. V and W can influence the deposition in a different way. Later we will come back to a discussion on V and W from a different perspective.

The immersion capillary force between particles, which maintains the continuous deposition of particles in our system, is also influenced by the particle concentration as we mentioned in 3.3.2. The immersion capillary force is sensitive to the distance between particles. When the distance is increased the capillary force will decay dramatically. A high concentration indicates a smaller distance between particles. Thus we expect a larger C_2 to promote the maintenance of deposition. This conclusion have been used to explain the ending of deposition in our previous discussion. When particles in the cell edge gradually deposit on the substrate, the total number of particles in the milky line region decreases and C_2 decreases as well. When C_2 drops below a threshold value, the capillary interaction cannot compete with the backward forces exerted on particles by the liquid-air interface and the deposition stops growing. We have designed experiments to validate the influence of C_2 on the maintenance of deposition. In two experiments we kept all the other experimental conditions the same and changed C_1 only. Deposition was able

to be initiated in both cases, however, we found the larger C_1 resulted in a larger area of deposition, which meant the deposition was kept longer and the ending of deposition was postponed with a higher particle concentration (Figure 3.9).

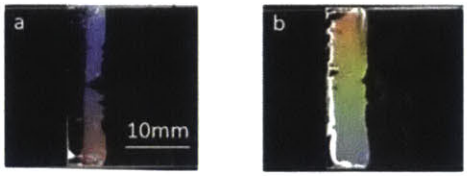

Figure 3.9 In these two experiments $V = 20\mu L$, $W = 25mm$, $RH = 24\%$, and $\delta = 10°$. However, in (a) $C_1 = 12.5mg/mL$ whereas in (b) $C_1 = 50mg/mL$. It is clear that the deposition area increases altogether with the increase of solution concentration C_1.

In conclusion, a high concentration of particle solution C_1 is favorable as it will increase the concentration C_2 around the liquid edge. Both the initiation of deposition and the maintenance of continuous growth of particle array can benefit from the increased C_2. V and W should also be taken into consideration for the control over C_2.

Nevertheless, a too high concentration can become a trouble for the monolayer structure as well. As schemed in Figure 3.10, when the aggregation of particles is so concentrated that not only particles at the very front but also particles immediately behind them (in dark gray) are pinned. Then the structure deposited on the substrate is multi-layered. In our system, when the concentration is as high as $C_1 = 50mg/mL$ the deposition is still monolayered.

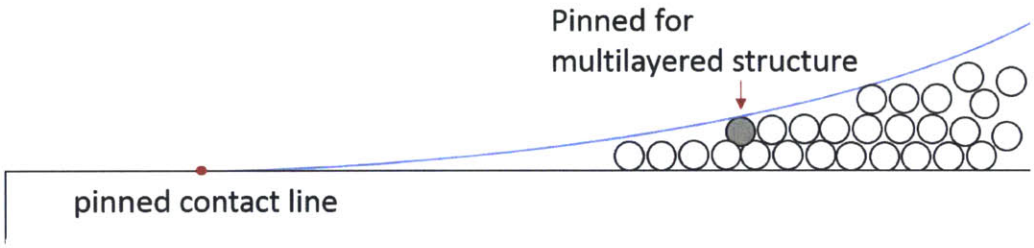

Figure 3.10 If the concentration is too high, not only particles at the very front are pinned, particles on the upper layer (the dark gray particle, for example) will also be pinned. Then instead of a monolayer structure, the deposition is multilayered.

3.4.2 Pressure Drop

In section 3.2, we pointed out that the pressure drop ΔP imposed by the concave meniscus can hurdle the initiation of deposition. According to equation (3.3), ΔP is inversely proportional to the radius of curvature R, which is then related to the liquid volume V and the substrate width W as illustrated by equation (3.2). Equation (3.2) indicates that the increase of V or the decrease of W will result in a larger R and therefore enhances the chance of deposition.

We start from the analysis on V. As shown in Figure 3.8.a and discussed in section 3.4.1, the deposition across the whole width of substrate could not be initiated with $\mathrm{C_1 = 12.5mg/mL}$, $\mathrm{V = 60\mu L}$, $\mathrm{W = 75mm}$, $\mathrm{RH = 24\%}$, and $\delta = 10°$. This time instead of increasing C_1, we increased liquid volume to $\mathrm{V = 180\mu L}$ and a deposition of monolayer structure was obtained (Figure 3.11.a). However, as mentioned before the concentration C_2 is associated with V we cannot ensure the initiation of deposition after increasing V is due to the change of R rather than the increase of C_2. Thus we designed another experiment. In this one $V = 180\mu\mathrm{L}$ whereas C_1 was decreased to the third of the original value, namely $C_1 = 4.2\mathrm{mg/mL}$. As the total number of

particles was the same as that in the experiment corresponding to Figure 3.8.a, in which $V = 60\mu L$ and $C_1 = 12.5mg/mL$, the concentration around the liquid edge C_2 was definitely no larger than that corresponding to Figure 3.8.a. This time a continuous monolayered deposition was achieved as shown in Figure 3.11.b. Now we can conclude that the pressure drop ΔP plays an important role in enabling the particle deposition.

Similarly, according to (3.2) the decrease of substrate width W can also result in a larger R and promote the initiation of deposition. As shown in Figure 3.11.c, when other experimental conditions were kept the same as in the experiment corresponding to Figure 3.8.a, we used a substrate with a smaller width $W = 25mm$, a monolayer structure deposited on the structure.

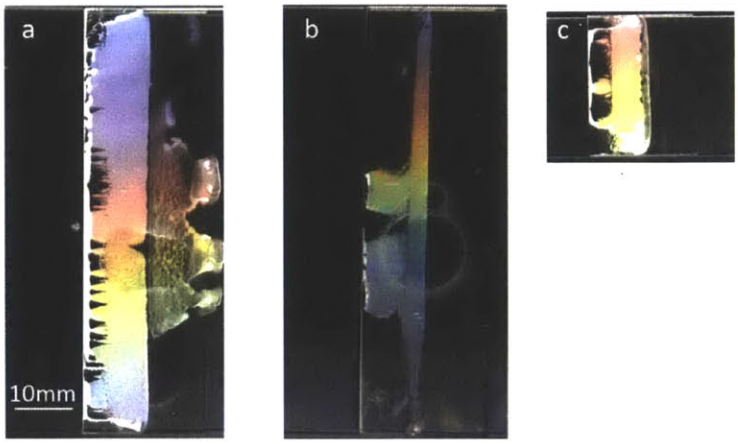

Figure 3.11 (a) When V was increased from $60\mu L$ to $180\mu L$, a large-sized monolayer structure was obtained. (b) After V was increased to $180\mu L$ and C_1 was decreased to $4.2mg/mL$ a continuous deposition was still observed. (c) The decrease of W to $25mm$ could also enable the continuous deposition.

3.4.3 Relative Humidity and Tilting Angle

It has been reported that relative humidity (RH) has an influence on the pinning of contact line. Chhasatia et al. claimed that the high RH would result in a low contact angle and more

spreading, which was desirable for the particle deposition [82]. Shen et al. found that the increase of RH leads to a decrease of minimal size of droplet for the formation of "coffee ring" deposition, which indicate a stronger pinning of contact line [80].

We designed control experiments to study on the role of RH in our wedge system. In two experiments $C_1 = 12.5\text{mg/mL}$, $V = 60\mu\text{L}$, $W = 25\text{mm}$, and $\delta = 0°$. One was conducted at low $\text{RH} = 24\%$ whereas the other at $\text{RH} = 65\%$. As shown in Figure 3.12.a and Figure 3.12.b, there was no obvious difference in deposition results between those two experiments despite that it took much longer time to have liquid evaporate completely under high RH. It is also reported in the drag method that RH only changed the evaporation rate but not had much influence on the deposition structure [67]. Perhaps in our system, the contact line pinning was already stable enough even under the low RH. Then the effect of the higher RH on pinning was undetectable.

Ye et al. have reported that by tilting the wedge cell downward, the gravity component could contribute to the particle transportation from bulk reservoir towards the drying front and therefore promote the deposition [65]. We have also tried to introduce a tilting angle δ to our experiment system. Therefore a gravity component pointing along the substrate surface was imposed on particles. We found when the wedge cell was tilted downward with $\delta = 10°$, the deposition area was just increased slightly (Figure 3.12.a,c), indicating that the gravity component parallel with the substrate surface did not have obvious influence in our wedge cell system.

In the study by Ye et al. [65], the transportation of particles from the liquid reservoir towards the contact line was ascribed to the gravity rather than the evaporation-induced flux. The dominant role of gravity in particle transportation, however, was invalid in our system when $\text{RH} = 24\%$. Here is the proof: First, we observed that it took about 10 minutes to have the milky line

formed when $\delta = 0°$ or when gravity did not function in the system. With $\delta = 10°$ the time needed for the formation of milky line was shortened slightly to 8-9 minutes. Since the milky line indicates the ability to transport particles form the bulk liquid reservoir towards the edge of wedge cell, the tiny difference in the time needed for the formation of milky line demonstrates that gravity was not the main contribution to the particle transportation. The fact that the deposition area was not increased obviously when the cell was tilted can also verify the small contribution of gravity.

According to [65] all the experiments in Ye et al.'s work were conducted with RH $\geq 65\%$. When we increased RH to 65% the increase of deposition area after tilting the wedge cell was much more obvious as shown in Figure 3.12.b,d. Here is the explanation to this experimental result: The increase of RH can slow down the evaporation rate. According to the empirical equation, the evaporation rate can be slowed down by 2.5 times when RH is raised from 24% to 65%. In experiment we observed that it took 160 minutes to have all the liquid evaporate at $\mathrm{RH} = 24\%$ whereas 370 minutes at $\mathrm{RH} = 65\%$. As the evaporation was slowed down the corresponding influx would become smaller. Then the particle transportation due to gravity, which was uninfluenced by RH, played a comparatively more important role than before. There is an alternative understanding: the increase of RH required a longer time to have all the liquid evaporate; the gravity component was then able to transport particles for a longer time during the slowed-down evaporation process; finally more particles were transported by gravity to the edge of cell.

In conclusion in this section we find both high RH and the gravity are favorable conditions for the particle deposition as well as the increase of deposition area. In order to make the best use of them the high RH and the tilting angle should be satisfied at the same time.

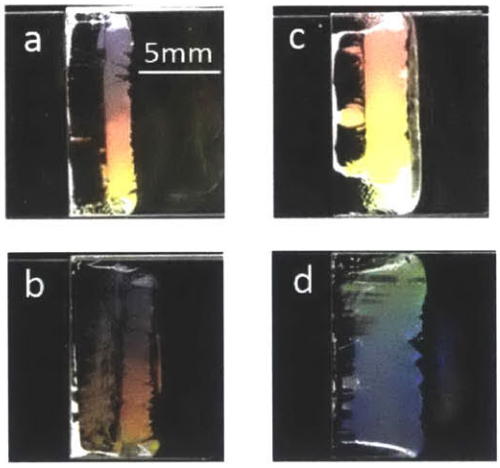

Figure 3.12 Control Experiments for the study on the influences of RH and tilting angle. $C_1 = 12.5\text{mg/mL}$, $W = 25\text{mm}$, and $V = 60\mu\text{L}$. (a) $RH = 24\%$, $\delta = 0°$; (b) $RH = 65\%$, $\delta = 0°$;(c) $RH = 24\%$, $\delta = 10°$; (d) $RH = 65\%$, $\delta = 10°$. The comparison between (a) and (c) indicates that the change of RH did not have obvious influence on the deposition result. When RH was kept at a high value, the increase of deposition contributed by gravity (b and d) was much more obvious than that at a low RH (a and c).

3.4.4 Surface Property of Substrate

The surface property we will focus on in this section is the wetting property, which can be quantified by the contact angle θ of water-air interface on the substrate. As mentioned in 3.4.3, a small contact angle can lead to more spreading and benefit the deposition of particles [82]. Moreover, M. Malaquin et al. pointed out that the convective assembly can only take place for the surface with a contact angle smaller than 20°. When the contact angle is too large the horizontal component of the force imposed on the particle by the meniscus will pull particles back towards the liquid reservoir. It is also reflected in (3.4) and (3.5): the backward forces are related to the angle φ. Since φ can be increased by increasing the contact angle θ, the worse wetting property of substrate surface will result in a stronger pushing force towards the liquid phase.

We applied H_2O_2 treatment to substrates for different time lengths in order to have them exhibit different contact angles. In general, the longer treatment results in a smaller contact angle. In this way we were able to study the influence of contact angles on the convective assembly in our wedge cell. After the treatment we used the goniometer to measure the contact angle. In our wedge cell system when $\theta < 40°$ the monolayer structure could be obtained. With a larger θ no particle can deposit.

According to those experimental results we treated all the substrates for a small θ or equivalently a good wetting before the assembly. Several treatment methods for this purpose are available. The hot bath of H_2O_2 renders $\theta < 10°$. The oxygen plasma and the piranha treatment can render an even smaller contact angle $\theta < 5°$.

3.4.5 Conclusion on Experiment Conditions

Now we can conclude the setting of experimental conditions for the deposition of monolayer structure based on above discussions. First, the substrate should be treated for good wetting property or a small contact angle θ. We employed the hot bath of H_2O_2. A high concentration C_2 in the vicinity of contact line is favorable both for initiating the deposition and maintaining the continuous deposition. C_2 is influenced not only by the solution concentration C_1 but also the liquid volume V and the substrate width W. A high C_2 can be achieved by choosing a high C_1, a large liquid volume V and a large substrate width W. Since a too high C_2 can result in a multilayered structure, setting of C_1, V, W should be adjusted for different fabrication purposes. Introducing both a high relative humidity and a nonzero tilting angle to the system can assist in the maintenance of high C_2 and increase the size of deposition. In our wedge cell system, when $C_1 = 12.5\text{mg/mL}$, $V = 60\mu\text{L}\,(180\mu\text{L})$, $W = 25\text{mm}\,(75\text{mm})$, $\text{RH} = 65\%$ and $\delta = 10°$ a centimeter-sized deposition of monolayer structure consisting of $1.08\mu m$ diameter particles can

be obtained. We also employed this recipe to the fabrication on substrates with aluminum coating, which is used in the SAW measurement. A good monolayer structure is obtained with our experimental setting and the deposition result is illustrated in Figure 3.13.

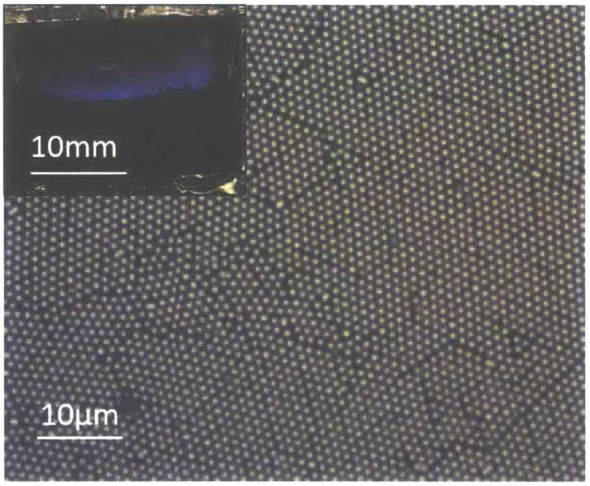

Figure 3.13 A representative microscope image of the microsphere monolayer. The inset is the photo of sample.

3.5 Fabrication of Nanosphere Monolayer

In Chapter 2 we have discussed the influence of several parameters on the wave modulation and propose the possibility of using those parameters to control the wave behavior. For example, the change of the particle size can influence the resonant frequency as well as the coupling strength. The fabrication of a monolayer structure composed of differently sized particles will enable the experimental measurement, which can be used to examine the numerical analysis. In this section we explore the fabrication of monolayer structure consisting of 519nm diameter silica particles based on the deposition mechanism concluded in 3.3 and the discussions in 3.4.

First we directly used the experimental conditions concluded for the monolayer of 1.08μm-diameter particles in section 3.4 to fabricate the monolayer structure composed of $519nm$

diameter particles. When $C_1 = 12.5\text{mg/mL}$, $V = 60\mu\text{L}$, $W = 25\text{mm}$, RH $= 65\%$ and $\delta = 10°$ the deposition was in general of multilayered structure as shown in Figure 3.14. As analyzed in section 3.4.1, a too concentrated aggregation of particles can result in a too strong pinning. Then the deposition of multilayered structure instead of a monolayer will be initiated. Since with the above experimental setting the monolayer of 1.08μm diameter microspheres can be obtained, the pinning can be maintained at least for the liquid film with a thickness of 1.08μm. Then for the smaller particles with a diameter of 519nm the strong pinning is possible to result in the multilayered deposition as schemed in Figure 3.10. Furthermore we can also observe that as the deposition continued the color of the deposited structure gradually transformed from the opaque white color to a transparent one, indicating the thickness of the deposited structure gradually decreased. This observation can be explained by the decrease of particle concentration at the drying front. As deposition continues, the concentration decreases, due to which the monolayered deposition becomes possible again.

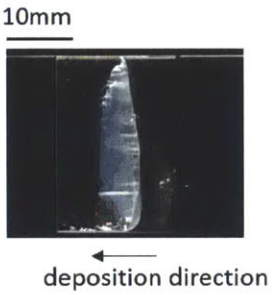

Figure 3.14 Photo of the deposition of $519nm$ diameter nanospheres. Along the deposition direction, the color of the deposition structure changes from the opaque white to a transparent, indicating the gradual decrease of thickness. The area inside of the dotted red rectangle is the thinnest regime and expected to be a monolayer structure.

Based on the result above, in order to have 519nm particles deposit into a monolayer structure, the particle concentration C_2 in the vicinity of contact line should be decreased. Among

several possible choices, increasing the substrate width W is a very convenient one. As we have observed the failure in initiating the deposition for 1.08μm particle with width $W = 75\text{mm}$ as shown in Figure 3.8.a, $W = 75\text{mm}$ may successfully result in the monolayer structure composed of those smaller particles. In addition, an increased W not only results in a smaller effective concentration C_2 but also increases the strength of the backward force F_p and F_γ, which could prevent particles corresponding to the multilayered structure from depositing as analyzed in 3.4.2. So we increased the width W to 75mm, kept all the other experimental conditions the same as before, and did the assembly experiment again. With this setting a large area of transparent film deposited on the substrate, which signaled a monolayer structure for 519nm particles (Figure 3.15.a). In Figure 3.15.b the SEM image validates that the structure is monolayered after the adjustment of experimental conditions.

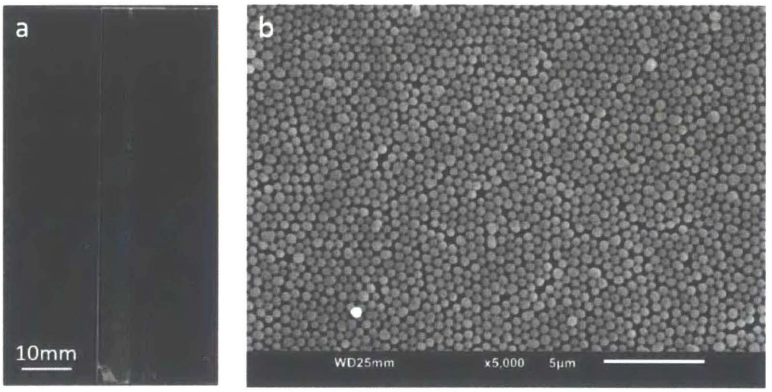

Figure 3.15 (a) Photo of the sample composed of 519nm diameter nanospheres after adjusting the concentration C_2 via the increase of W. The deposition structure is of a transparent color. (b) SEM image of the sample.

In this section we have applied the the assembly mechanism and the analysis on influential factors concluded in 3.2 and 3.3 to fabricating the monolayer structure composed of differently

sized particles. By adjusting the substrate width W, the concentration C_2 was effectively lowered and the pinning corresponding to a multilayered structure was avoided. The fabrication of monolayer structures composed of different micro/nanoparticles on different types of substrates may also be achieved via the adjustment of experimental settings in a similar manner.

Chapter 4 Measurement on Modulated SAWs in Granular Crystals

The application of focused short laser pulses to excite SAWs in the untrasonic regime is an important breakthrough in studies on SAW and material science [3]. In this chapter, we will introduce the measurement on the granular crystal sample by using the laser technique, transient grating. The measurement result is then processed and interpreted into the dispersion spectrum. The method for data analysis is an important part in the post-measurement process and therefore is included in this chapter as well. We start from an introduction of the transient grating technique and provide the measurement settings for our granular sample. Then we give the measurement result and the dispersion spectrum of granular crystal samples composed of two differently sized microparticles. The comparison between experimental result and theoretical analysis in chapter 2 is to be discussed as well.

4.1 Transient Grating Method

Transient grating method, also known as impulsive stimulated thermal scattering, is applied intensively to the measurement on mechanical properties and thermal transport of thin films. It is a non-contact and non-destructive technique and effective in detecting the surface behavior. Transient grating is also widely manipulated for SAW measurement on solid or liquid thin films, including both free standing films and those bound to substrates [83,84]. We also implement the transient grating method to measure SAWs modulated by the granular "film". The configuration of transient grating setup is illustrated in Figure 4.1.

In transient grating, SAWs are excited by two short pulses derived from an excitation laser. The two pulse beams cross at an angle of θ, enter into the surface of the sample and generate an interference pattern, which then forms a sinusoidal intensity profile on the substrate surface with a period of

$$\Lambda = \frac{\lambda_e}{2\sin(\frac{\theta}{2})} \tag{4.1}$$

where λ_e is the wavelength of the excite beam.

If the substrate can absorb energy from the light pattern, a thermal expansion of the same sinusoidal profile will form and launch the coherent monochromatic counter-propagating SAWs with a wavelength of Λ on the substrate. For transparent substrates which cannot absorb light energy, the conventional solution is to coat a very thin aluminum film on the transparent surface. This is the reason why we choose aluminum-coated glass slides as substrates. Due to the symmetry of the excitation beams, only Rayleigh waves can be excited whereas other surface waves, for example Love waves, cannot be excited.

As indicated by equation (4.1), wavelength or wave vector of SAWs is determined by the crossing angle θ of the two excitation pulses if the wavelength of excitation beam is fixed. By adjusting this angle, wave vector can be changed. In experiment, one single excitation pulse passes through a binary phase mask with periodic grating structure at first (Figure 4.1). Due to diffraction by the grating structure, the single pulse is transformed to an array of pulses. Only the ± 1 order diffracted pulses are selected to enter into the sample surface. Then the crossing angle θ is equal to the diffracted angle of the ± 1 order diffracted pulses. This diffraction angle is determined by the period of the phase mask. Therefore by using phase masks with different periods, we can excite SAWs with various wavelengths. In our measurement, the phase masks used can generate SAWs

with wavelength ranging from 3.2μm to 43.5μm. There are some other methods for the wave excitation. For example, instead of generating the light grating on the substrate, people can coat a metal grating structure on the substrate surface, which absorbs energy from a uniform excitation pulse. The wavelength is completely determined by the period of the metal grating [85]. Since the available fabrication technique can create metal gratings with very small period length, this method can generate SAWs with wavelength shorter than 1μm. Limited by the optical diffraction, the transient grating method cannot achieve not small wavelength. Nevertheless, our measurement does not require short wavelength. In addition, transient grating method is more flexible in view that it can adjust the wavelength of SAWs easily.

After the excitation, a single beam with wavelength λ_p is incident onto the phase mask and splits into two diffracted beams, one is used as a probe beam and the other is attenuated and used as a reference beam. The phase difference between those two beams can be adjusted in order to maximize the intensity of the final signal and this method is called heterodyne detection. The probe beam is then diffracted by the surface ripples or the refractive index variation on the sample. The ripples are mainly the surface displacements induced by surface waves. The refractive index variations are contributed by the bulk longitudinal wave. Therefore by using transient grating, we can also get the information of longitudinal wave.

The diffracted probe beam then interferes with the reflected reference beam. The time-dependent intensity of the interference is collected by a detector. The temporal signal can be used directly for the thermal property analysis. However, for the wave analysis, the signal Fourier transform is usually employed in the data processing, which will be elaborated later.

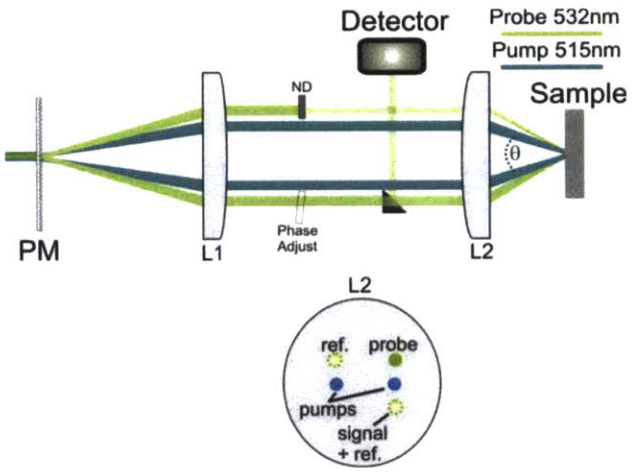

Figure 4.1 Schematic illustration of transient thermal grating experiment in reflection geometry. The diffractive optic, a binary phase-mask (PM), splits incident pump and probe beams into ± 1 diffraction orders. The two resulting pump beams are focused and crossed at the sample surface by a set of lenses (L1 and L2), generating the transient thermal grating. Diffracted probe light is combined with an attenuated reference beam (ND) and directed to a fast detector. The relative phase difference between probe and reference beams is controlled by adjusting the angle of a glass slide (Phase Adjust) in the probe beam path. At the bottom, the spatial arrangement of beams on L2 is depicted. The figure is adapted from [84].

In Transient Grating measurement the probe beam can enter into the sample either from the front side or the back side. For our sample specifically, the probe beam enters onto the back side for the wave analysis. We have also done the front-side measurement where the probe beam touches microparticle directly and therefore can detect particle motion. The comparison of front-side and back-side results are used to analyze the modulation mechanism and support our analysis model.

In our measurement, the excitation beam is from a laser source with a wavelength of 515nm and a pulse duration of 60ps. The total pulse energy at the sample is 2.44μJ. The pump spot on the sample surface has a diameter of 500μm at $1/e^2$ intensity level. The aluminum layer can quickly absorb the laser light and induce a rapid thermal expansion, which leads to the generation of SAWs with a wavelength defined by the period of phase mask. A quasi-cw probe

beam with a wavelength of 532nm and a diameter of 150μm is used for the signal detection. The probe beam is focused at the center of the excitation spot. The average power of the probe beam on the sample is 10.7mW. The interference of diffracted probe beam and the reference beam is then directed to a photodiode with a 1GHz bandwidth. The signal is recorded using an oscilloscope and averaged over 10^4 repetitions.

With those parameters, we can estimate the vertical displacement of the substrate surface induced by the thermal expansion of the aluminum film. This displacement then is a criterion to examine the validity of the linear model we applied in Chapter 2. Following [86], the amplitude of the substrate vertical displacement is

$$u_{z,0} = g\Gamma Q_0 \tag{4.2}$$

$$g = \frac{3\alpha_L(1-R_{ref})}{\rho_1 C_p}\left(1 - \frac{4c_T^2}{3c_L^2}\right), \tag{4.3}$$

$$\Gamma = \left[\left(c_T^2 - \frac{1}{2}c_R^2\right)\left[(c_T^2 - c_R^2)^{-1} + (c_L^2 - c_R^2)^{-1}\right] - 2\right]^{-1} \tag{4.4}$$

$$Q_0 = \frac{Q_L}{\pi R_L^2} \tag{4.5}$$

Parameters in (4.3) are the linear thermal expansion coefficient $\alpha_L = 23.6\mu\text{m/m}\cdot\text{K}$, density $\rho_1 = 2.7\text{g/cm}^3$, the specific heat $C_p = 0.90\text{kJ/kg}\cdot\text{K}$, and the surface reflectivity $R_{ref} = 0.92$ of aluminum, respectively. c_T, c_L, c_R are transverse, longitudinal and Rayleigh wave velocities of the glass substrate. Here velocity values are the same as those used in Chapter 2, namely $c_T = 3280\text{m/s}, c_L = 5640\text{m/s}, c_R = 3013\text{m/s}$. Plugging all the parameters in (4.2)-(4.5), we get :

$u_{z,0} = 8.1\text{pm}.$

Despite that the displacement of the particle is possible to be larger than that of the surface displacement, the estimated $u_{z,0}$ is over an order less than the displacement induced by adhesive contact at the equilibrium position, which is

$\delta_0 = 0.44\text{nm}$ as analyzed in 2.2. Therefore the validity of the linear model is proved.

4.2 SAWs in Granular Crystal Composed of 1.08μm Microparticle

In this section the measurement results on the granular crystal sample composed of 1.08μm diameter microparticles are provided. Methods for signal processing and parameter fitting are included in this section as well.

4.2.1 Measurement Result and Data Analysis

First we provide the back-side measurement result on the sample coated with 1.08μm diameter particles. As mentioned previously, by choosing a phase mask with a specific period, we can determine the wavelength or the wave vector of SAWs. We repeated the measurement for multiple times and each time we used a different phase mask. In this way we can examine the wave behavior under various wave vectors and finally get the dispersion property of SAWs in our granular crystal sample. In Figure 4.2 we use the measurement result with $\lambda = 10.0\mu\text{m}$ or $k = 0.63\mu\text{m}^{-1}$ as an example to show the typical data we obtained in one measurement. Figure 4.2.a-b are the temporal signals obtained directly from transient grating measurement. Figure 4.2.a is for a location on the sample that is not covered by microparticles, which will be referred to as "off-particle" case. Figure 4.2.b is for a location covered by granular crystal, which will be referred to as "on-particle" case. In both cases, there is a sharp initial increase which is induced by the excitation source. The slowly decaying profile of the temporal signal is contributed by the thermal

grating associated with the temperature profile in the sample [32,84]. This component may be used for the analysis on materials' thermal properties. The high frequency component then corresponds to the SAW propagating in the material and is what we are concerned with. Figure 4.2.c-d are the Fourier spectra of acoustic oscillations corresponding to the temporal signal in Figure 4.2.a-b. In the off-particle case, there are two sharp peaks on the Fourier spectrum. One at the lower frequency corresponds to the Rayleigh wave and the other at a higher frequency is induced by the longitudinal wave. As we mentioned in 4.1, the transient grating can detect the refractive index change, which is mainly contributed by the bulk longitudinal wave. The on-particle case is distinctly different from the off-particle case, which are indicated by both the Fourier spectra 4.2.c-d and temporal signals 4.2.a-b. From 4.2.c we can observe that the peak corresponding to the longitudinal wave is unaffected by the existence of particle coating whereas the peak for Rayleigh wave is split into two. This observation validates that the modulation from the granular crystal is a surface effect. This modulation does not influence the bulk mechanics, such as the longitudinal wave. The comparison of Rayleigh peaks between "off-particle" case and "on-particle" case is highlighted in Figure 4.2.d.

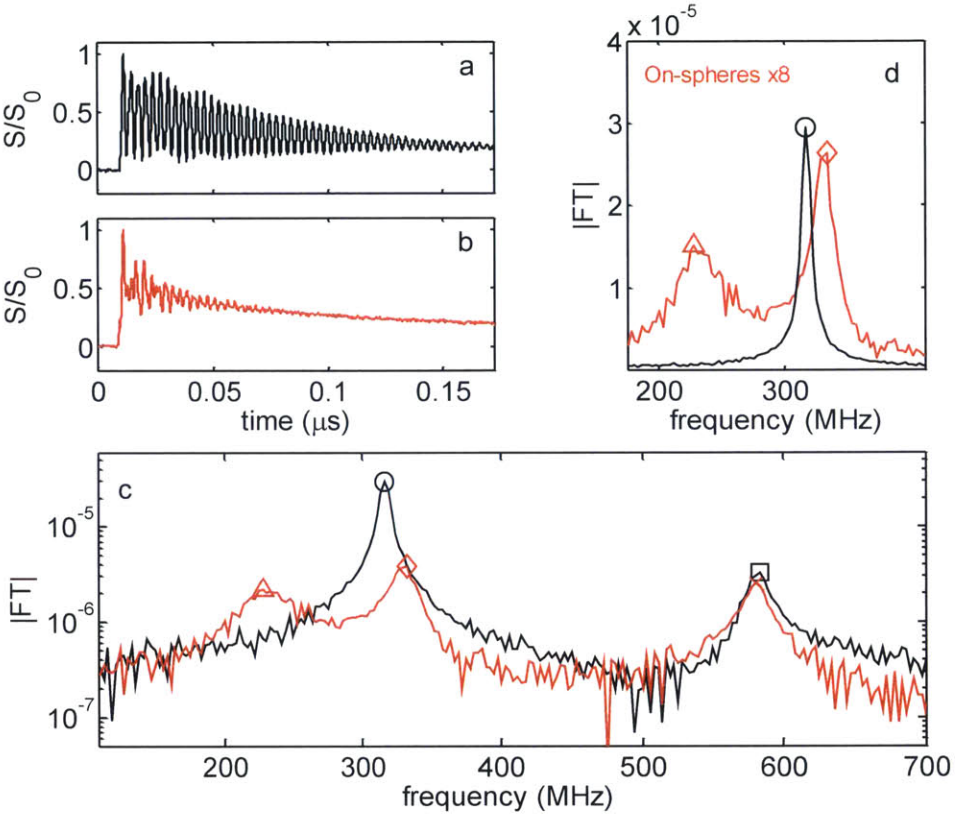

Figure 4.2 (a-b) Normalized temporal signals of off-particle shown in (a) and on-particle shown in (b) for $k = 0.63\mu m^{-1}$. The acquired signal S is normalized by the maximum signal amplitude S_0. (c-d) Fourier transform magnitudes corresponding to the signals in (a-b) plotted in linear scale (c) and in log scale (d). The black curve corresponds to signal in (a) and the red curve to signal in (b). The markers denote the identified peaks, which are also plotted in Figure 4.3 and Figure 4.4 using the same makers.

In the same manner, we completed the transient grating measurement and identified peaks from the Fourier spectra by using multiple wavelengths. The spectra for all the used wavelengths are illustrated in Figure 4.3. Peaks in the Fourier spectra are identified by different markers. From this multiple-wavelength measurement, we can obtain dispersion curves of modulated Rayleigh wave and other wave modes in our granular crystal system as shown in Figure 4.4.

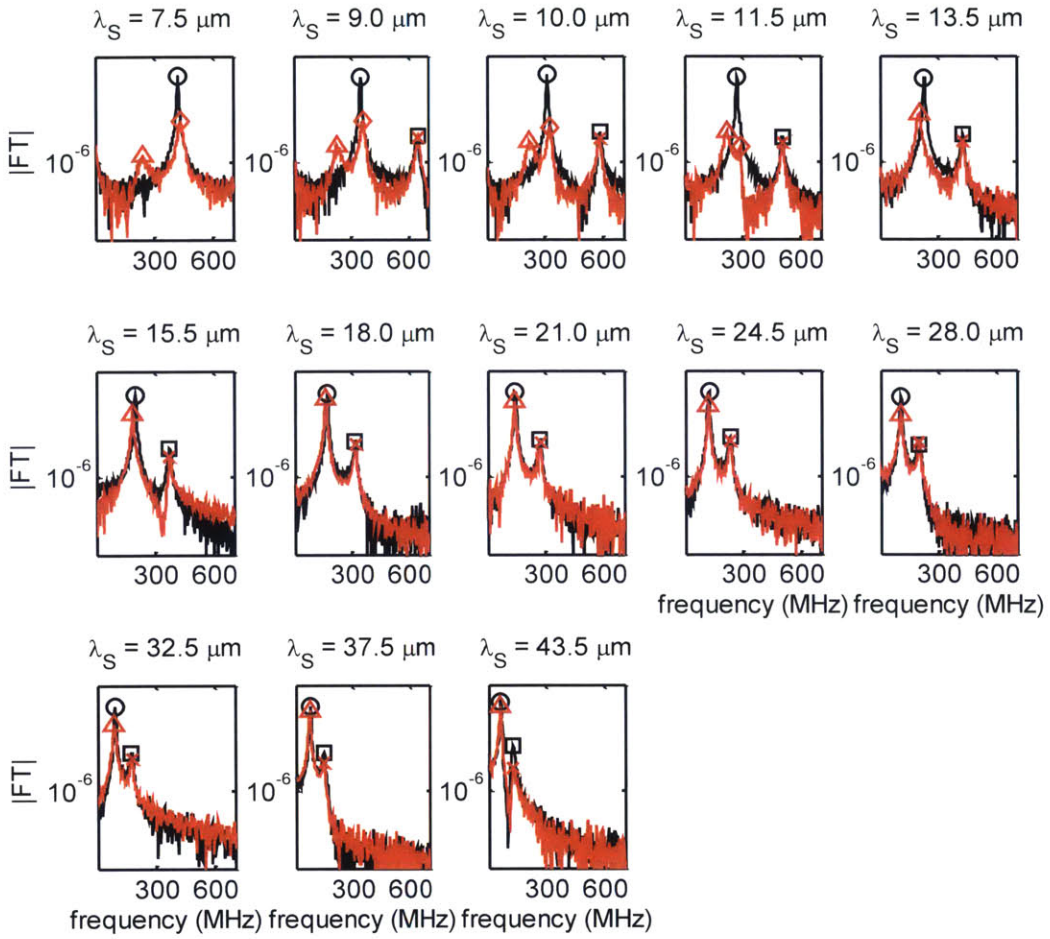

Figure 4.3 Measured spectra for multiple SAW wavelengths, ranging from $7.5\mu m$ to $43.5\mu m$. The black curves are for the off-particle measurement and the red curves for on-particle measurement. Identified peaks are denoted by the same types of markers used in Figure 4.2.

In Figure 4.4, all the markers are experimental data and curves are the numerical results computed according to the model discussed in chapter 2. The parameter fitting involved in the numerical computation will be elaborated later. At this moment we focus on wave properties exhibited in Figure 4.4.

From the off-particle case, we can see that the longitudinal component satisfies the linear dispersion property and the Rayleigh wave on the bare substrate is close to linear, the same as what

we obtained in section 2.3. As for the modulated Rayleigh wave, the profile of this measured dispersion curve is similar to the numerical result shown in Figure 2.7. From Figure 4.4, we can see that the on-particle Rayleigh dispersion (red triangles and diamonds) displays a classical "avoided crossing" between the normal Rayleigh wave mode and the resonance of mircoparticles. The lower branch starts as a Rayleigh wave at low wave vector magnitudes and approaches a horizontal asymptote corresponding to the resonant frequency of microparticle. The upper branch is similar to the Rayleigh wave at high wave vector magnitudes. In the "avoided crossing" region, the upper branch deviated from the Rayleigh wave and stops at the threshold corresponding to the transverse bulk wave as we predicted in section 2.4.

In chapter 2 we have computed the dispersion relation of the modulated Rayleigh wave as expressed in (2.31):

$$(2-\frac{\omega^2}{k^2{C_T}^2})^2-4\left(1-\frac{\omega^2}{k^2{C_L}^2}\right)^{\frac{1}{2}}\left(1-\frac{\omega^2}{k^2{C_T}^2}\right)^{\frac{1}{2}}=\frac{m}{A\rho_2}\frac{\omega^4\left(1-\frac{\omega^2}{k^2{C_L}^2}\right)^{\frac{1}{2}}}{k^3{C_T}^4}\frac{1}{\left(\frac{\omega^2}{{\omega_0}^2}-1\right)}, \tag{2.31}$$

We can use this equation to numerically compute the dispersion curve for the modulated Rayleigh wave and compare this numerical result with experimental data. In (2.31), the frequency of contact resonance ω_0 is included. In chapter 2 we have computed $f_0=\frac{\omega_0}{2\pi}=144\text{MHz}$. However, this value can be different from the true resonance frequency in the experimental system. The difference is caused by uncertainties in the contact and adhesion models. For instance, a greater work of adhesion w in the experimental system than the value estimated from the Hamaker constant may result in a higher resonant frequency. The contact mechanics in nanoscale is still a challenging field of research and the available contact models including DMT model cannot accurately describe the nanoscale contact system [87]. All of those reasons can lead to a resonant

frequency different from the result derived in chapter 2. However, we can fit the measured data shown in Figure4.4 according to the analysis result (2.31) and treat the resonant frequency f_0 as a single fitting parameter. We then use the fitted f_0 to compute the dispersion numerically. In that sense, our SAW measurement on the granular sample can provide a promising study tool for the research of nanoscale contact mechanics. The detailed introduction of the fitting method introduced in the appendix of this chapter.

The acoustic dispersion curves based on the fitting result is shown in Figure 4.4. The numerical result of Rayleigh wave is denoted by red solid curves. In general the numerical dispersion curves are in agreement with the measured data, especially in the upper branch region and lower branch region measured with longer wavelengths. The disparity between the numerical result and the experiment data in the flat dispersion region is due to that the fitted resonance frequency f_0 is smaller than the measured largest frequency in the lower branch. However this f_0 is still the best fitting considering all the measured data points: there are only a small number of data points at the flat region to support the fitting whereas a larger number of data points are available in other regions, which finally result in a fitted f_0 lower than expected. Meanwhile, as shown in Figure 4.3, peaks corresponding to the Rayleigh modes at lower branch are widened at the flat region, which may influence an accurate measurement.

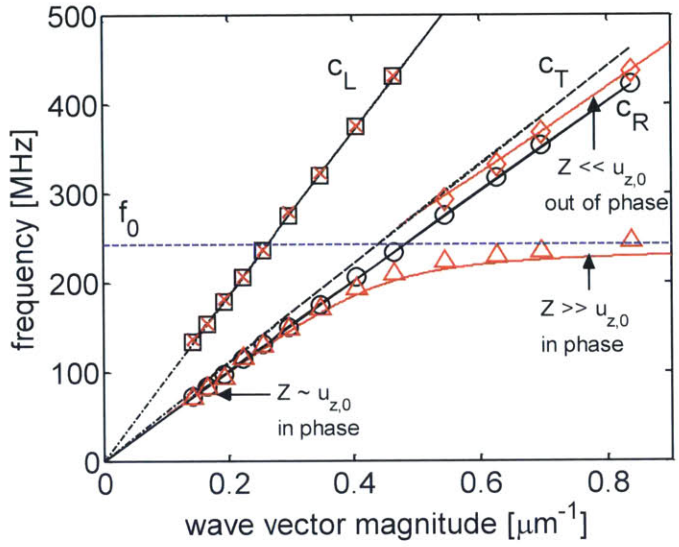

Figure 4.4 Dispersion relations. Red and black markers are the measured frequency peaks for the on-particle and off-particle cases. The solid red line is the dispersion calculated using (2.31). Also shown are lines corresponding to longitudinal wave, transverse wave, a Rayleigh wave in glass substrate and a horizontal dashed blue line corresponding to the frequency of contact resonance.

4.2.2 Discussion

A. In chapter 2, we have defined a parameter α, which is the ratio of particles' vertical displacement z to the substrate displacement $u_{z,0}$. According to (2.26)

$$\alpha = \frac{z}{u_{z,0}} = \frac{K_{2,DMT}}{K_{2,DMT} - m\omega^2}.$$

Since $K_{2,DMT} = m\omega_0^2$, we can rewrite α into:

$$\alpha = \frac{z}{u_{z,0}} = \frac{{\omega_0}^2}{{\omega_0}^2 - \omega^2}. \tag{4.8}$$

Therefore in the lower branch when wave vector k and frequency ω are small, we have $z \sim u_{z,0}$, and $z, u_{z,0}$ are of the same sign, namely in phase. When the wave vector is large and the Rayleigh wave is split into two branches, the upper branch at high frequencies $\omega \gg \omega_0$ satisfies $z \ll u_{z,0}$

whereas the lower branch corresponding to a $\omega \approx \omega_0$ satisfies $z \gg u_{z,0}$. In addition, for the former case the two displacements are of opposite signs and therefore out of phase. The above discussion indicates the lower branch wave should have a progressively smaller amplitude compared to the upper branch as the splitting exhibits. This conclusion is supported by the spectra in Figure 4.3. In Figure 4.3, for measurements done with short wavelengths, we can see the splitting of Rayleigh peak takes place and the amplitude of the lower branch peak is smaller than that of the upper branch. In addition, as the wavelength gets shorter, the amplitude disparity between the lower branch mode and the upper branch mode becomes more obvious. We have also completed the front-side measurement, namely the probe beam enters onto the microparticle side. In this way, we can directly measure the particle displacement z. Thus the comparison between the front-side and the back-side measurements can be used to validate the scaling relation between z and $u_{z,0}$.

As illustrated in Figure 4.5, the spectra in red are back-side measurement results and those in blue are front-side results. It clearly displays that when the wave length is large whereas wave vector k and frequency ω are small, the amplitude of the particle-motion peaks (blue triangles) are close to the amplitude of peaks of modulated Rayleigh wave (red triangles). When the wavelength becomes smaller and the splitting takes place, for peaks corresponding to the lower branch (marked by triangles) where $\omega \approx \omega_0$, we can see that the front-side peaks have larger amplitudes than the back-side peaks, indicating $z > u_{z,0}$. By contrast, as for peaks corresponding to the upper branch (marked by diamonds), the front-side peaks are weaker than the back-side ones, indicating $z < u_{z,0}$. This observation is consistent with our analysis based on (4.8). Also we can see that the front-side spectrum does not exhibit the frequency peak for longitudinal wave as the particle motion is not related to the bulk wave.

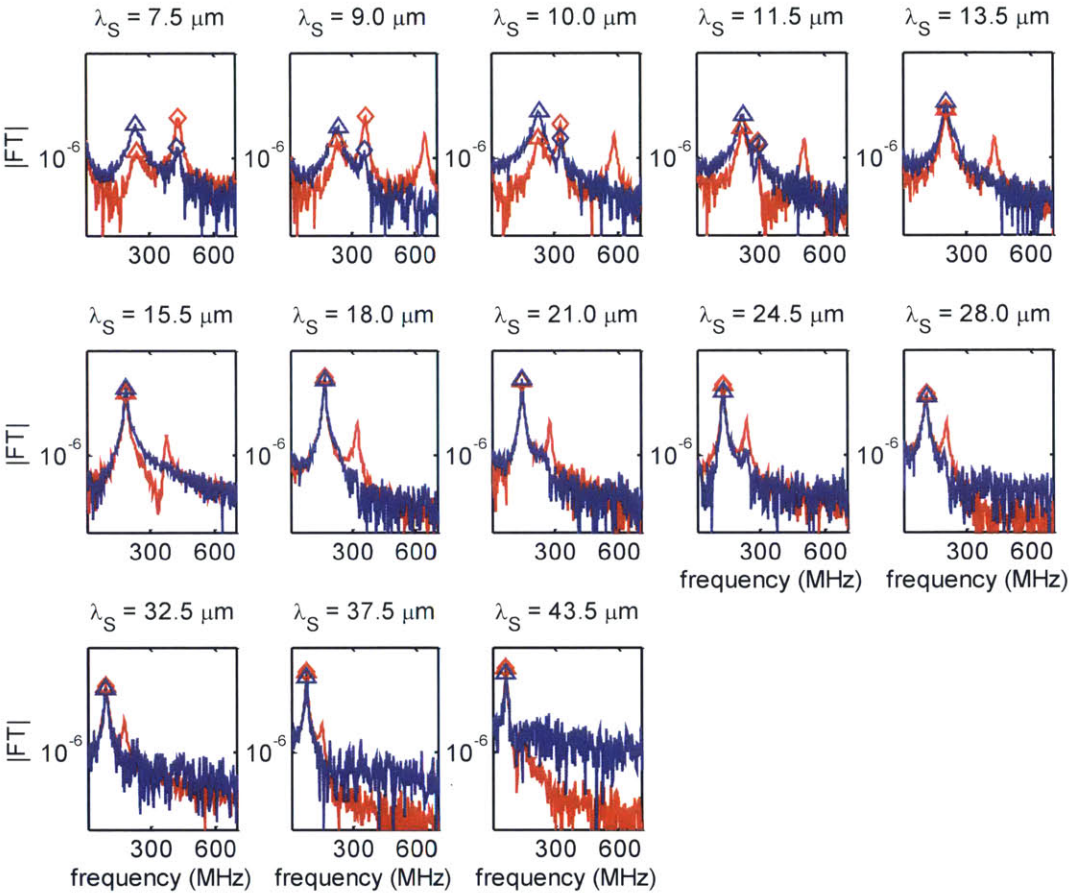

Figure 4.5 Spectra of multiple wavelength measurements. Red curves are for the back-side measurement and blue curves are for the front-side measurement. The red and black triangle markers are used to denote signals corresponding to the surface wave at lower branch and the particle motion, respectively.

B. The comparison between on-particle and off-particle measurements indicates that the former case has a faster decay (Figure 4.2.a) and broader peaks (Figure 4.2.d). In the off-particle measurement, the acoustic wave signal decays because the counterpropagating SAWs leave the probed area [32]. In the on-particle measurement, as the group velocity of the modulated SAW is slower, a longer decay time is expected. Therefore the opposite observation indicates the existence of additional attenuation. One possible mechanism is the scattering induced by microparticles. However, the scattering cannot be generated by collective array on a half-space with $\omega < c_T k$

despite that the single sphere oscillator is able to radiate energy into the substrate [32]. Peak broadening is also possibly induced by anharmonicity. However, we have estimated the wave amplitude in 4.1, which indicates that the particle motion is still in the linear region. One possible contribution to acoustic losses in periodic structure is the disorder that makes the structure deviate from the exact periodicity. The variation of the particle size and the polycrystalline of granular crystal structure are possible defects in our granular system.

C. In the measurement on 1.08μm particle sample, the shortest wavelength is 7.5μm, which satisfies the long wavelength condition compared to the dimension of microparticles. Therefore the experimental result can be compared with the derivation in Chapter 2 which is based on effective medium approximation. This scale difference can also make our granular crystal structure eligible to be included in the group of metamaterials. The locally resonant oscillating particles are in essence the artificial atoms in this SAW metamaterial. In our model, particles are treated as independent oscillators and the interactions between neighboring particles are neglected. Despite that particles are closely packed, the numerical result based on our simplified model where we treat those particles as independent oscillators matches the experimental data very well. It is again, likely due to the long wavelength used in our theoretical analysis and experiment. At shorter wavelengths, we expect to see different dynamics due to interaction between particles.

4.3 SAWs in Granular Crystal Composed of 519nm Nanoparticle

4.3.1 Measurement Result and Data Analysis

We have also prepared the monolayer of particles with 519nm diameter. In this way, we can examine the influence of particle size on the wave modulation as we have numerically

computed in 2.5.1. On the one aspect, the comparison of measurement results of different samples can help examine the validity of our model. On the other aspect, the comparison may be employed to control the SAW behavior by using particles of various dimensions in the future.

In this measurement, the wavelength ranges from 3.2μm to 43.5μm. Since the diameter of the particle now is only 519nm, the long wavelength condition is still satisfied. We implemented the back-side measurement. The data were analyzed in the same way as introduced in 4.2. We have used the same fitting method and derived the resonant frequency, which is $f_0 = 628\text{MHz}$.The obtained dispersion curve is illustrated in Figure 4.6. The dispersion profile is similar to that for 1.08μm particle case shown in Figure 4.4. The Rayleigh wave is modulated by the granular crystal effectively and also splits into two branches around the resonant frequency.

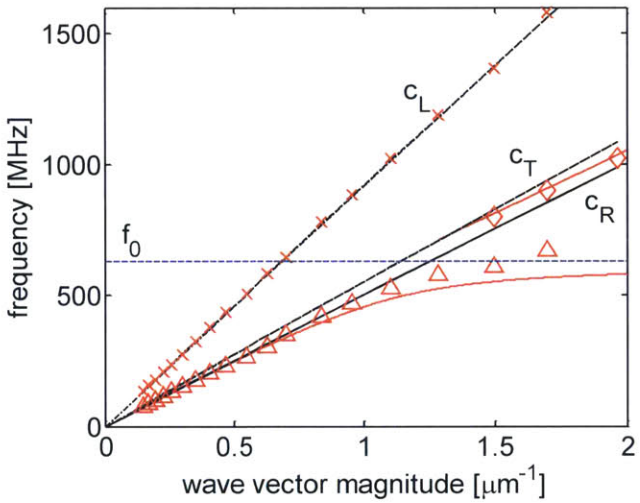

Figure 4.6 Dispersion relations. Red markers are the measured frequency peaks for on-particle measurement. The solid red line is the numerical result based on our model. The dispersion curves for the longitudinal wave and transverse wave on the substrate and the normal Rayleigh wave are fitting results from the off-particle measurement as discussed in section 4.2. The dashed blue line denotes the fitted frequency of microparticle contact resonance.

This estimated resonant frequency is still smaller than the measured largest frequency in the flat dispersion region. However, it renders the best fitting result considering all the data points on both the lower branch and the upper branch. The spectra from the multiple wavelength measurement are sown in Figure 4.7. We can see that the peak corresponding to the lower branch disappears in the measurement with shortest wavelength $\lambda_s = 3.2\mu m$,. As we analyzed in section 4.2, when the splitting takes place, the Rayleigh-wave-like mode on the upper branch is dominant. By contrast, the particle-motion-like mode becomes undetectable.

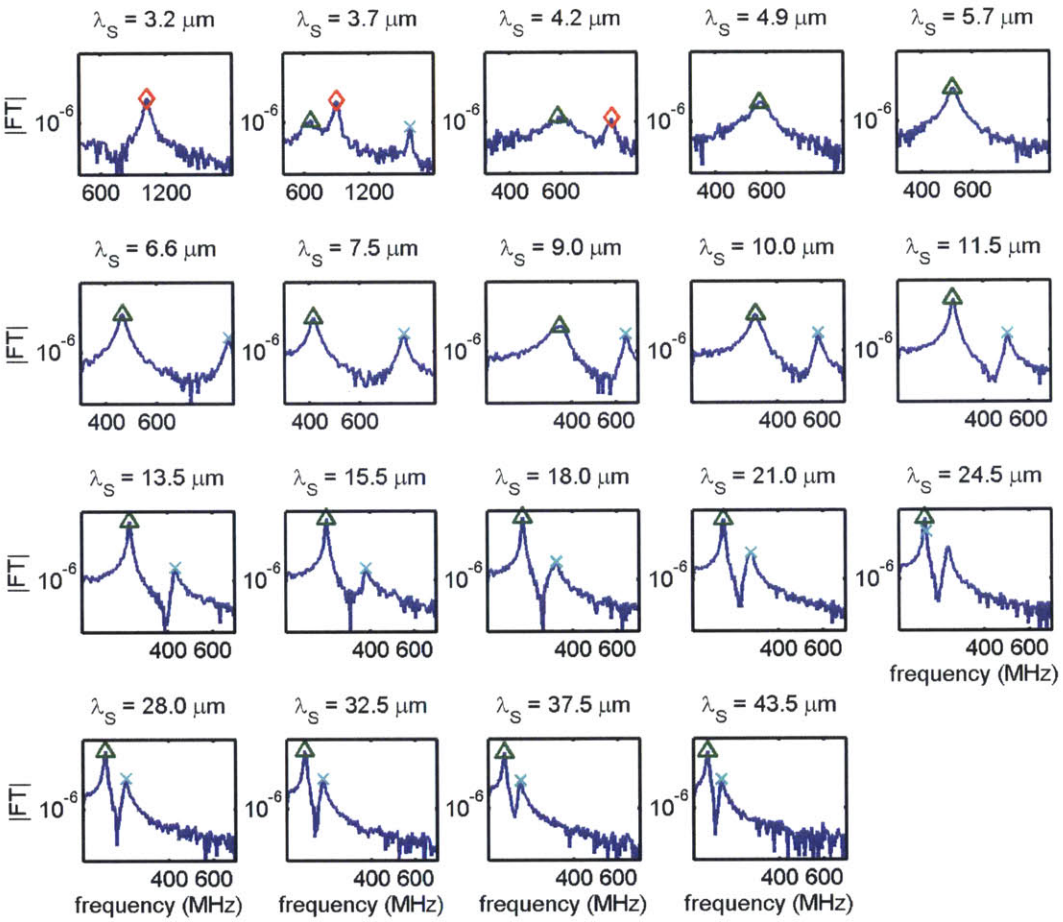

Figure 4.7 Measured spectra for multiple wavelengths. The green triangles denote the wave modes at the lower branch whereas the red diamonds denote those at the upper branch of the modulated Rayleigh wave. The light blue crosses denote the longitudinal wave peaks.

4.3.2 Discussion

In 2.5.1 we have analyzed the relation between the resonant frequency and particle dimension, which is

$$f_0 \sim R^{-7/6}, \tag{4.9}$$

We can also get the relation between the spring constant in DMT model and the particle dimension, which is

$$K_{2,DMT} \sim R^{\frac{2}{3}}. \tag{4.10}$$

Now we have two differently sized particles, $R_1 = 540\text{nm}, R_2 = 259.5\text{nm}$. The resonant frequency for those two cases are $f_1 = 242\text{MHz}$ and $f_2 = 628\text{MHz}$, respectively. We can see

$\frac{f_1}{f_2} = 0.39$, which is close to $(\frac{R_1}{R_2})^{-7/6} = 0.43$.

For those two case, spring constants are $K_{2,DMT,1} = 3.06\text{kN/m}, K_{2,DMT,2} = 2.28K\text{kN/m}$. Then we plug those values into (4.9) and find

$\frac{K_{2,DMT,1}}{K_{2,DMT,2}} = 1.34$ whereas $(\frac{R_1}{R_2})^{2/3} = 1.63$.

This value computed from experimental results is approximately consistent with the theoretical analysis, which again supports the validity our model.

4.4 Conclusion

In this chapter, we have introduced the laser technique----transient grating, which is applied to measuring the wave property in our granular crystal samples. According to the measurement setting, we have validated that the motion of particle is in the linear regime and therefore supported the theoretical model we established in chapter 2. The measurement on granular crystal samples exhibits the classic "aovided crossing" phenomenon around the frequency of contact resonance. The measurement result is in great agreement with our numerical result. We have measured two granular samples composed of particles with 1.08μm diameter and with 519nm diameter,

respecitvely. The comparison of their measurement results is also consistent with the theoretical analysis covered in chapter 2.

Appendix

Now we give a step-by-step description of the fitting method used to derive f_0 and we use the result shown in Figure 4.4 as an example.

A. The value of longitudinal velocity c_L is first estimated from the off-particle measurement data. As stated above and shown in Figure 4.2-4.4, peaks located at the highest frequency in each spectrum, namely those marked by black squares, correspond to the longitudinal wave. We use those longitudinal wave peaks from the off-particles measurements to fit the velocity of longitudinal wave c_L. According to the linear dispersion property of longitudinal wave, the fitting equation is $\omega = c_L k$ and c_L is the fitting parameter. In this way, we obtain $c_L = 5775\mathrm{m/s}$.

B. Although the transient grating cannot directly detect the signal of transverse waves, we can still estimate the value of c_T from Rayleigh wave data. As mentioned before, the lower frequency peaks in the off-particle measurement are for the Rayleigh wave, namely those marked by black circles. In chapter 2, we have derived the dispersion equation for the Rayleigh wave on a bare substrate, which is

$$(2-\frac{\omega^2}{k^2{c_T}^2})^2 - 4\left(1-\frac{\omega^2}{k^2{c_L}^2}\right)^{\frac{1}{2}}\left(1-\frac{\omega^2}{k^2{c_T}^2}\right)^{\frac{1}{2}} = 0. \tag{2.20}$$

Now we reformulate this equation and get:

$$4\left(1-\frac{\omega^2}{k^2{c_L}^2}\right)^{\frac{1}{2}} = \frac{(2-\frac{\omega^2}{k^2}\cdot\frac{1}{{c_T}^2})^2}{\left(1-\frac{\omega^2}{k^2}\cdot\frac{1}{{c_T}^2}\right)^{\frac{1}{2}}}, \tag{4.6}$$

We plug the measured (k, ω) data pairs for Rayleigh mode and c_L from step A in (4.6) and treat the left hand side term $4\left(1-\frac{\omega^2}{k^2{c_L}^2}\right)^{\frac{1}{2}}$ as a single variable y dependent on the other variable $x \equiv \frac{\omega^2}{k^2}$. Then $\frac{1}{{c_T}^2}$ becomes a parameter in the fitting equation:

$$y = \frac{(2-x\cdot\frac{1}{{c_T}^2})^2}{\left(1-x\cdot\frac{1}{{c_T}^2}\right)^{\frac{1}{2}}}. \tag{4.7}$$

The nonlinear fitting problem (4.7) is solved by using the "nlinfit" function of MATLAB R2013b. We then get $c_T = 3464.9\text{m/s}$.

C. The Rayleigh wave velocity can also be estimated from Rayleigh wave data. By approximating the dispersion of Rayleigh wave as a linear relation, we can get $c_R \approx 3154\text{m/s}$.

The fitted dispersion curves for the longitudinal wave, the transverse wave and the normal Rayleigh wave are all plotted in Figure 4.4.

D. Then we can estimate the value of resonant frequency ω_0 by reformulating (2.31) into

$$\frac{m}{A\rho_2}\frac{\omega^4\left(1-\frac{\omega^2}{k^2{C_L}^2}\right)^{\frac{1}{2}}}{k^3{C_T}^4}[(2-\frac{\omega^2}{k^2{C_T}^2})^2 - 4\left(1-\frac{\omega^2}{k^2{C_L}^2}\right)^{\frac{1}{2}}\left(1-\frac{\omega^2}{k^2{C_T}^2}\right)^{\frac{1}{2}}]^{-1} = \left(\frac{\omega^2}{{\omega_0}^2}-1\right),$$

The whole left hand side term is treated as a single variable u dependent on the variable $v \equiv \omega^2$, then $\frac{1}{{\omega_0}^2}$ is simply a parameter in a linear fitting $u = \frac{1}{{\omega_0}^2}v - 1$. This time we plug in the (ω, k) data pairs corresponding to the modulated surface waves, namely those marked by the red triangles and diamonds in Figure 4.4. We get

$f_0 = \frac{1}{2\pi}\omega_0 = 242\text{MHz}$. This resonant frequency is highlighted by a dashed blue line in Figure 4.4.

E. Plugging the derived resonance frequency f_0 in equation (2.31), we can get the numerical dispersion curve for modulated Rayleigh wave as shown by the red solid lines in Figure 4.4.

Chapter 5 Granular SAW Waveguide

Waveguides are important structures in various systems. They are applied for guiding the wave along a particular path, confining the energy in a finite space, and accordingly realizing the wave propagation without attenuation. SAW waveguides have been intensively explored theoretically and experimentally due to not only the interesting physics phenomenon intrinsic to waveguides but also their wide applications, especially in devices for optical communication and signal processing. Waveguides can overcome problems in the planar propagation including beam spreading, inefficient use of the substrate area, and awkwardness in bending wave path [88,89]. When device circuits get more compacted and complicated, a good confinement of wave becomes a critical requirement in order to avoid circuit crosstalk. Consequently, waveguides, which can help reduce the need of substrate space, are integral to the design of compact circuits. Similar to other wave systems, waveguides for SAW system are mostly based on a "fast-slow-fast" structure. The majority of reported studies on SAW waveguides are of this structure and referred to as strip waveguides (Figure 5.1.a). A strip waveguide consists of an overlaid strip material on the substrate. The strip can reduce the wave velocity and thus the wave velocity on the strip regime is slower than that on the bare regime [90]. Conventionally, a thin metal layer is used as slow strip [89]. Metal strip waveguides have been widely used in convolvers that depend on surface wave beams. After the development of phononic structures for SAWs, which can render unusually slow wave velocity, waveguide structures based on artificial periodic structures were proposed. SAW waveguides based on phononic crystals are one of the most frequently reported, in which the wave is slowed down due to the band gap of phononic crystals [91–94].

As we analyzed in previous chapters, around the resonance frequency of particle oscillation, the dispersion curve of the modulated Rayleigh wave gets flattened and accordingly the phase velocity $\frac{\omega}{k}$ becomes exceptionally small. In consequence, we propose to use the granular crystal as the slow strip material and get a strip waveguide based on granular structure, which is composed of a strip of closely packed microparticle deposition on the bare substrate (Figure 5.1.b). In addition, we expect a great confinement effect in this granular waveguide considering two reasons. One is the granular crystal can support a very slow wave around the resonance frequency. In general, the larger velocity contrast between the strip regime and in the substrate regime can result in a better waveguide confinement. The other reason is Hertzian contact is an extremely confined mechanism. Therefore the wave modulation and the corresponding slow waves, which are enabled by Hertzian contact, can be confined in the granular crystal regime strictly.

In this chapter, we will explore the application of granular crystals in realizing waveguide function for SAWs. Theoretical analysis, method employed to fabricate granular waveguides, and the results from preliminary experiment by using transient grating technique are to be presented.

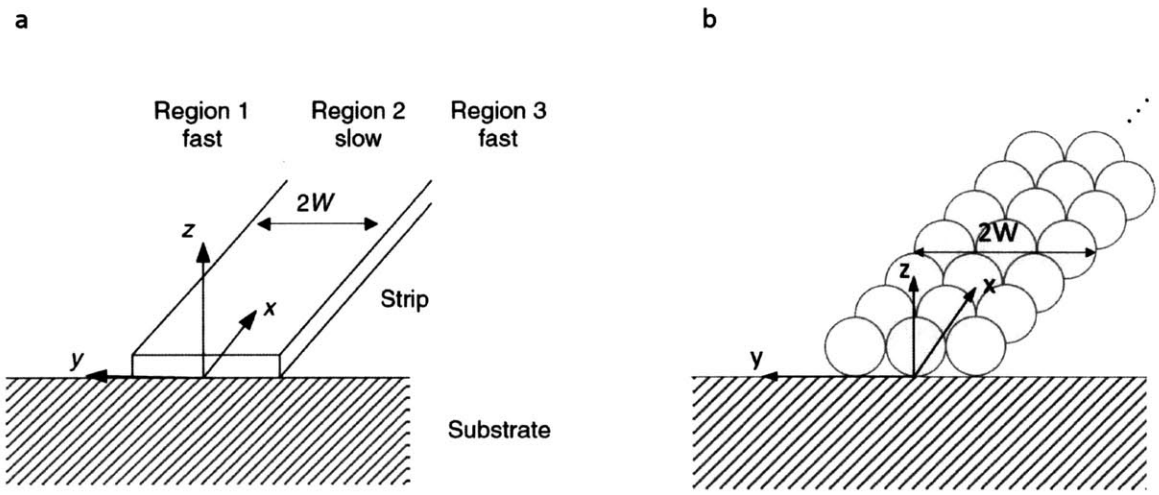

Figure 5.1 (a) The strip waveguide for surface acoustic waves. The image is adapted from [90]. (b) By replacing the strip material with granular crystals, we propose a granular waveguide structure, which is expected to render an effective waveguide mode.

5.1 Theoretical Analysis

As illustrated in Figure 5.1.b, the granular waveguide we have proposed has a length of L and a width of $2W$. Particles which compose the waveguide have a diameter of $1.08\mu m$. $L \gg W$ is satisfied and therefore the waveguide structure can be treated as infinitely long, which will be made use of to simplify the theoretical analysis. For a given width $2W$, a set of waveguide modes can be supported. Although it is possible to obtain a rigorous solution for the strip SAW waveguide, the derivation process which involves multiple nontrivial boundary conditions, is particularly cumbersome [95]. An approximation solution is therefore employed conventionally in studies on SAW strip waveguides [88–90,95]. In our analysis, we adopt the simplified model in [95]. The wave is then formulated into

$$\psi_n(x, y), \tag{5.1}$$

where $n = s, f$ represents for the slow medium and the fast medium, respectively. This formulation is explicitly dependent on y coordinate because the whole waveguide structure including the substrate outside of the strip regime is not uniform in the y direction. For our granular waveguide, the slow medium is namely the regime covered by microparticles and the fast medium is the bare substrate.

The approximate solution for waveguide modes is derived by matching the amplitude of $\psi_n(x, y)$ and its normal derivative at boundaries. The wave vectors for slow and fast regime are represented by k_s, k_f. For a waveguide mode, the component of wave vector along the propagation direction, namely x axis in our coordinate, should be the same everywhere. Therefore we have

$$k_{s,x} = k_{f,x} = k_x \tag{5.2}$$

The confinement effect of waveguides requires that the wave mode exists only inside of the slow medium and quickly decays to zero as approaching to the fast substrate. Accordingly the y component of the wave vector in fast regime is an imaginary number. Instead of using an imaginary $k_{f,y}$, we define a coefficient $\kappa_{f,y}$ as the magnitude of this component, namely:

$\kappa_{f,y} = |k_{f,y}|$, $k_{f,y} = i\kappa_{f,y}$. Then wave functions in (5.1) are elaborated into

$$\psi_s(x, y) = Aexp(-ik_x x - iik_{s,y} y) + Bexp(-ik_x x + ik_{s,y} y),\ |y| < W \tag{5.3}$$

$$\psi_f(x, y) = Cexp(-ik_x x)\exp(-\kappa_{f,y} y),\ |y| > W$$

where A, B, C are constants. All the wave vector components should satisfy these relations:

$$k_x^2 + k_{s,y}^2 = k_s^2 \tag{5.4}$$

$$k_x^2 - \kappa_{f,y}^2 = k_f^2$$

Combining (5.3) (5.4) and matching the wave amplitude as well as its derivative at boundaries $|y| = W$, we finally get the equation for waveguide modes:

$$Wk_{s,y} = m\frac{\pi}{2} + \tan^{-1}\left(\frac{\kappa_{f,y}}{k_{s,y}}\right), m = 0,1,2,\cdots \tag{5.5}$$

In order to get the dispersion relation of waveguide modes from equation (5.3), we have to compute the values of k_s, k_f at first. In this process, we still employ the effective medium approximation. We treat the granular crystal as a slow medium with a known dispersion equation (2.31). Given a specific frequency ω, we can get the magnitude of the corresponding wave vector k_s according to (2.31). Similarly, we can get the magnitude of the wave vector on the fast regime k_f from the dispersion equation of a normal Rayleigh wave (2.20). By plugging the derived k_s, k_f in (5.4) (5.5), we get the value of k_x. In this way, values of k_x for various angular frequencies ω are computed numerically and the obtained curve of ω versus k_x is namely the dispersion curve for waveguide modes.

Now we compute the dispersion relation of a ten-particle waveguide ($2W = 9.5\mu\text{m}$) as an example to illustrate the dispersion property of SAW waveguide. In our computation, we use the values of c_T, c_L, ω_0 estimated from the measurement on 1.08μm microparticle sample covered in 4.2. Specifically, $c_T = 3464.9\text{m/s}, c_L = 5775\text{m/s}, \omega_0 = 2\pi f_0 = 2\pi \times 242\text{MHz}$. The numerical result for the first three modes in this ten-particle waveguide is shown in Figure 5.2. The dispersion curve for the SAW on bare substrate and that for modulated SAW on granular crystal are also exhibited. The lowest mode with $m = 0$ is closest to the mode for the granular crystal. As the mode number gets larger, the phase velocity increases. Therefore the lowest mode is also the slowest one. All the modes are strictly confined between the dispersion curve for the modulated Rayleigh wave and that for a normal Rayleigh wave. Therefore the phase velocity of those wave

modes are guaranteed to be slower than the wave in the outer region. We can also observe that except for the lowest mode $m = 0$, all the other modes have their respective "cutoff" frequencies. At cutoff frequencies, the phase velocity of waveguide mode becomes equal to the velocity in the outer regime. This condition is equivalent to $k_s = k_f$ and $\kappa_{f,y} = 0$. Under that condition there is no velocity disparity and therefore the confinement effect cannot be supported. The cutoff frequencies for the two modes $m = 1, 2$ are marked in Figure 5.2.

When ω is small, the Rayleigh wave mode in the granular crystal structure is similar to the normal Rayleigh wave. Therefore the velocity disparity is also small. The waveguide mode, modulated Rayleigh wave and the normal Rayleigh wave are similar to each other and in Figure 5.2 those three curves (the dashed black curve for normal Rayleigh wave, the solid black curve for modulated Rayleigh wave on granular crystal, and the solid blue line for waveguide mode $m = 0$) are nearly overlapped. As the frequency ω gets closer to the resonance frequency, the modulated Rayleigh wave enters into the flat dispersion region and the phase velocity decreases sharply. In this case, the waveguide mode behaves similar to the slow Rayleigh wave in a granular structure. Since the waveguide is of a "fast-slow-fast" structure, the upper branch which has a larger phase velocity than the normal Rayleigh wave cannot be used to support the waveguide modes.

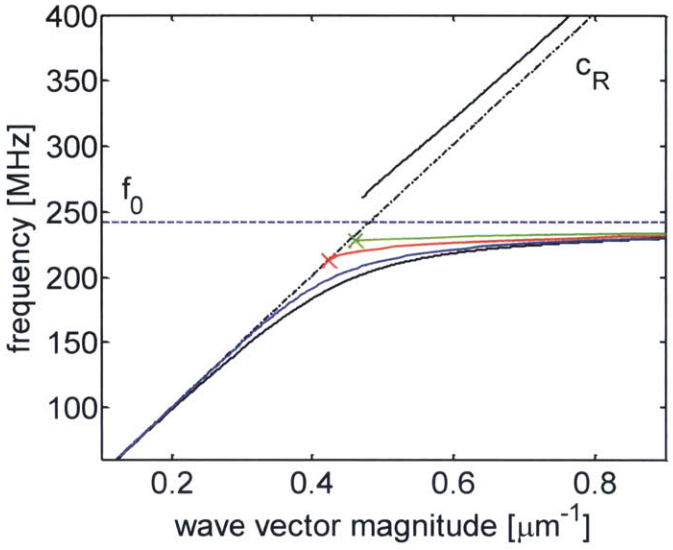

Figure 5.2 Dispersion relations. The solid blue, red and green curves are for the first three waveguide modes in the ten-particle-wide granular waveguide. The dashed black line is the dispersion curve of normal Rayleigh wave which can be supported by the bare substrate. The solid black line is for the modulated Rayleigh which can be supported by the granular crystal structure. The resonance frequency f_0 of this granular crystal is denoted by the dashed blue line. There are cutoff frequencies for waveguide modes with $m > 0$. Cutoff frequencies for $m = 1,2$ are marked by red and green crosses, respectively.

The solution for (5.5) can be used to examine the confinement effect as well. As equation (5.3) indicates, the waveguide mode decays exponentially in the slow regime:

$$\psi_f(x,y) = Cexp(-ik_x x)\exp(-\kappa_{f,y} y) \quad |y| > W \tag{5.3}$$

Therefore $\kappa_{f,y}$ is also a decay coefficient, which can quantify the confinement effect. The larger decay coefficient is expected to result in a better confinement effect. In Figure 5.3, the relation between the decay coefficient and frequency is illustrated. We can find that as the frequency approaches to the resonant frequency of particle oscillation, the decay coefficient increases, which indicates a stronger confinement effect. This conclusion is consistent with our conclusion above that the phase velocity in the granular crystal regime decreases sharply as approaching to the resonance frequency and the slow velocity is key to a great confinement effect.

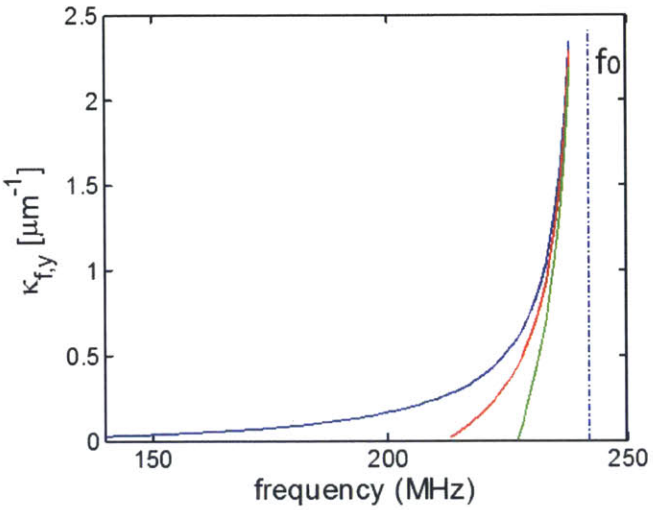

Figure 5.3 The relation between the decay coefficient and frequency. The solid blue, red and green curves are for the first three waveguide modes in the ten-particle-wide granular waveguide.

5.2 Fabrication of Patterned Granular Structure

5.2.1 Template-Assisted Assembly for Patterned Granular Structure

The fabrication of patterned granular structures on micro/nano scales is requested for various research purposes. The periodic artificial structures such as phononic crystals and metamaterials are possibly presented in the form of granular structures. The organized granular arrays can exhibit unconventional properties that enable novel optical devices, sensitive chemical sensors, high-density data-storage, catalytic applications, bioassays, etc. [96–98]. For our study on the SAW modulation via granular materials, the fabrication of patterned granular structure is not only requested for SAW waveguide but also desired for a better control over wave. For instance, the modulation of SAWs would be controllable if we are able to adjust the structural parameters of the granular crystal. As discussed in 2.5.3, changing the unit cell area or the distance between microparticles can influence the dispersion property of SAWs.

Template-assisted self-assembly is a frequently employed and robust technique for the fabrication of patterned granular structures [96–99]. In the fabrication process, a substrate patterned with desired structures are used as a template. Templates can take different forms, which are usually topographical confinement (such as physical holes and trenches on a flat substrate) [96,99–101] or chemical templates with hydrophilic-hydrophobic contrast pattern [102].

The patterned template are used in different assembly processes dependent on the feature of desired structures. Malaquin et al. have discussed two main processes where templates are used for controlled particle placement [96]. The first is convective assembly. This assembly has been discussed and employed in the fabrication of granular crystal structure in chapter 3. In a template-assisted convective assembly, the substrate is patterned. The receding direction of the particle solution is perpendicular to structures on the template. The non-structured regimes on the template have wetting surfaces and therefore particles can deposit continuously on the template similar to the monolayer deposition in Chapter 3. The patterned structure on the template performs as a geometrical barrier and prevents particles from depositing (Figure 5.4.a). This method is suitable for structures which are mostly covered by particles and sparsely patterned by non-particle regimes. The second assembly process is capillary assembly. The template in general is hydrophobic. On the flat regimes without patterned structure, particles cannot deposit due to the hydrophobicity on the surface. Once the receding meniscus reaches a structure on the template, the meniscus is dragged and flattened by the structure, and finally pinned there. Then a capillary force is created by the pinned meniscus. This force, together with the physical confinement induced by the template structure, can confine particles in recess regimes on the substrate (Figure 5.4.b). The capillary assembly method suits better for the sparse particle structure, namely the final sample is a bare substrate with sparsely patterned features covered by particles. The waveguide structure that

we aim to achieve, is a thin strip of particle deposition on the large bare substrate. Given this sparse structure, the capillary assembly process should be employed.

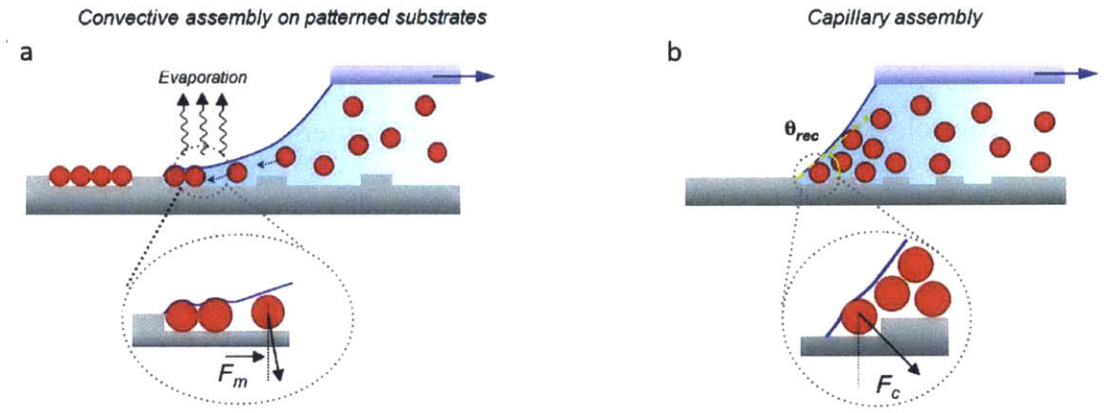

Figure 5.4 Schematic illustrations for (a) template-assisted convective assembly, where the flattened meniscus imposes a meniscus force to confine particles in the recessed regime; (b) template-assisted capillary assembly, where the capillary force and the physical confinement result in the particle deposition. Figures are adapted from [96].

The other thing to be considered in the fabrication of granular waveguide is the removal of template. In some other applications, the template does not influence the function of the granular structure. Yet for the SAW waveguide, the removal of template is necessary. The template structure is mostly made of a polymer, which can influence the SAW propagation severely. In the reported works which also require a granular pattern with no existence of template, the solution is to transfer the patterned granular structure to a bare substrate instead of removing the template [98,101]: after particles are deposited into desired pattern on the template, a carrier substrate is placed upon the template and contacts with particle structure directly. The carrier is chosen carefully in order to have a stronger adhesive contact with particles than the template surface. Thun when the carrier is raised up from the template, particles are picked up and stick to the carrier. After that, the carrier transfers the patterned particle array onto the target bare substrate which exerts an even stronger adhesive force on particles than the carrier surface. This method has

also been applied in a different way: a patterned carrier directly picks up particles from a uniform granular layer. In this way the pattern of carrier is imposed on the particle layer after the first transfer. Then the carrier continues to transfer the patterned particle array to a target plane [103]. This pattern transfer technique is efficient, however, has a high requirement on the experimental setting and control. The surface properties of template, carrier and target plane have to be considered carefully in order to support distinct disparity in adhesion with particles. The substrate selected according to this requirement may not be eligible for the SAW measurement. However, we can still borrow the idea of manipulating adhesion to enable the direct removal of template.

The template structure in our system is simply a uniform flat surface with a long recessed trench (Figure 5.5.a). We expect to confine particles inside of the trench during the capillary assembly. If we can guarantee a strong adhesion between particles and the surface of recess region in the trench, particles will be able to survive and stay on the substrate in the process of removing the template. By using the glass slide with an aluminum coating on the surface, which is the same type of substrates used for the granular crystal sample, we find the contact between the aluminum surface and silica particles are strong enough to keep the particle structure in the operation of removing template.

5.2.2 Fabrication Process

A. Template Preparation: For waveguide structures, we used the same type of substrates and the 1.08μm diameter microspheres for the fabrication of monolayer sample in Chapter 3. The substrate is aluminum-coated glass slide. Microparticles are made of silica and have a diameter of 1.08μm. The template we used is a patterned thin layer of photoresist, which can be easily removed later. We implemented photolithography to create a photoresist structure with trench patterns on the substrate (Figure 5.5.a). As mentioned above, the capillary assembly requires a hydrophobic

template surface. We have measured the contact angle of water on substrate covered by the photoresist OCG, which is about 45°. Thus the OCG photoresist is hydrophobic enough to support the capillary assembly [96] and it is used to fabricate the template. The depth of the recessed trench structure is expected to be close to the diameter of microparticle in order to have particles confined in the recessed regime effectively. Given the dimension of particles we used, the height of the trench was set as $1\mu m$.

In the fabrication, we first rinsed the substrate. However, this time we did not do the hot bath treatment of H_2O_2 as the hydrophilicity was not desired for the capillary assembly. Then we spin-coated the positive photoresist OCG on the substrate and adjusted the spin velocity to achieve a $1\mu m$-thick photoresist coating. Then photolithography was used to fabricate the photoresist template with trench patterns. We have designed a photomask with trench structures of various widths ranging from $1.1\mu m$ (for a one-particle-wide waveguide structure) to $16.2\mu m$ (for a fifteen-particle-wide waveguide structure), and therefore we could study on waveguide devices of different widths. The length of each designed trench pattern is $L = 1cm$. The distance between neighboring trench patterns is $4mm$. Thus the interaction between neighboring waveguides is negligible. After the whole photolithography process, we examined the thickness of the photoresist structure by Dektak profilometer (Veeco) and validated that the thickness of the trench pattern was about $1\mu m$.

B. Capillary Assembly: After the template was ready, we used the wedge method described in chapter 3 to assemble particles. The orientation of the template was important in the assembly. The length of the trench structure has to be perpendicular to the receding direction of the particle solution (Figure 5.5.b). In this way the trench structure can effectively pin the meniscus and

therefore confine particles in the recessed regime. The concentration of particle solution was 12.5mg/mL. The humidity was kept at 24% and the temperature was at 293K.

C. Removal of Template: After all the liquid evaporated, we continued to remove the photoresist template. Acetone is conventionally used to remove OCG photoresist in micro/nanostructure fabrication. We immersed the substrate deposited with microparticle pattern into a container of acetone. In order to remove the photoresist completely, the substrate was placed upside down so that particles facing downward. After immersion for 5 minutes, the sample was quickly taken out and flipped over to face upward. After the whole process, we observed that particles were able to stay on the substrate and the stripe structure was kept. As analyzed above, we believe it is due to the strong adhesion between particles and the bare substrate surface. The schematic illustration of fabrication process is shown in Figure 5.5.b. Experimental results after each fabrication step are provided in the following section.

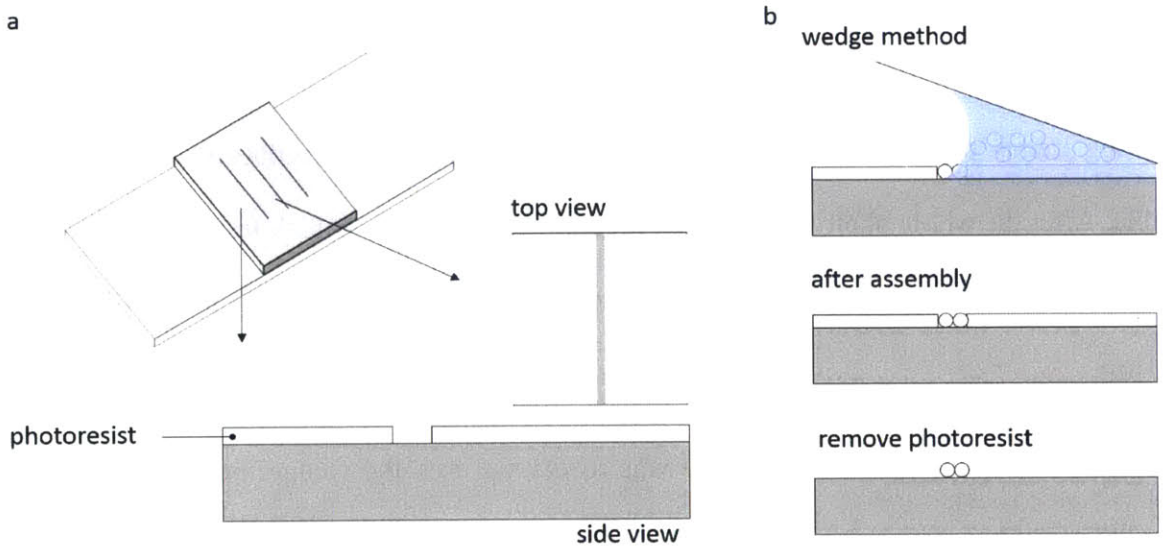

Figure 5.5 (a) A thin photoresist layer with trench structure is used as the template for the fabrication of granular waveguide. The side view and top view of the template structure are also provided. (b) The schematic illustration of the fabrication process. Particles are firstly assembled

by using the wedge method. After the assembly, the photoresist template is removed whereas the structure of particles is kept.

5.2.3 Waveguide Sample

We implemented the process described above to complete template preparation, particle assembly and the removal of template. Waveguides of different widths $2W$ have been fabricated. As mentioned, trench structures in the mask have a length of 1cm. Although the final sample is not necessarily that long, the length has to be close to that of pump spot used in the later measurement. The pump beam length in our current experiment is about $600\mu\text{m}$. Therefore We examined sample structures after all the fabrication process and used the following criteria to select samples for the measurement: (1) the length of microparticle strip $L > 600\mu\text{m}$; (2) no obvious defects along the whole length whereas small defects such as cavity, disorder, existence of extra particles over a length shorter than five particles is allowed (examples of minor and severe defects are given in Figure 5.7.d-f). In Figure 5.6.a-c, we show a waveguide sample of a single-particle-stripe structure as an example. The results after each fabrication process are included. This waveguide sample has a length $L \approx 1.5\text{mm}$. Waveguide structures of other widths are illustrated in Figure 5.7.a-c.

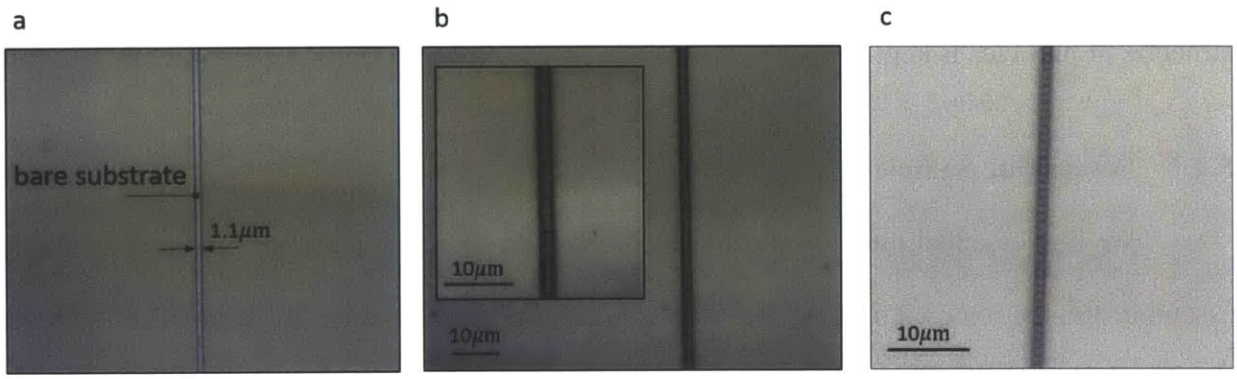

Figure 5.6 (a) The OCG photoresist template fabricated by using photolithography. The width of the trench structure is about 1.1μm. (b) The result after the wedge method assembly: particles are confined inside of the trench, which is uncovered by photoresist. (c) Waveguide sample after the removal of template. Particles are still on the substrate and the strip structure is kept.

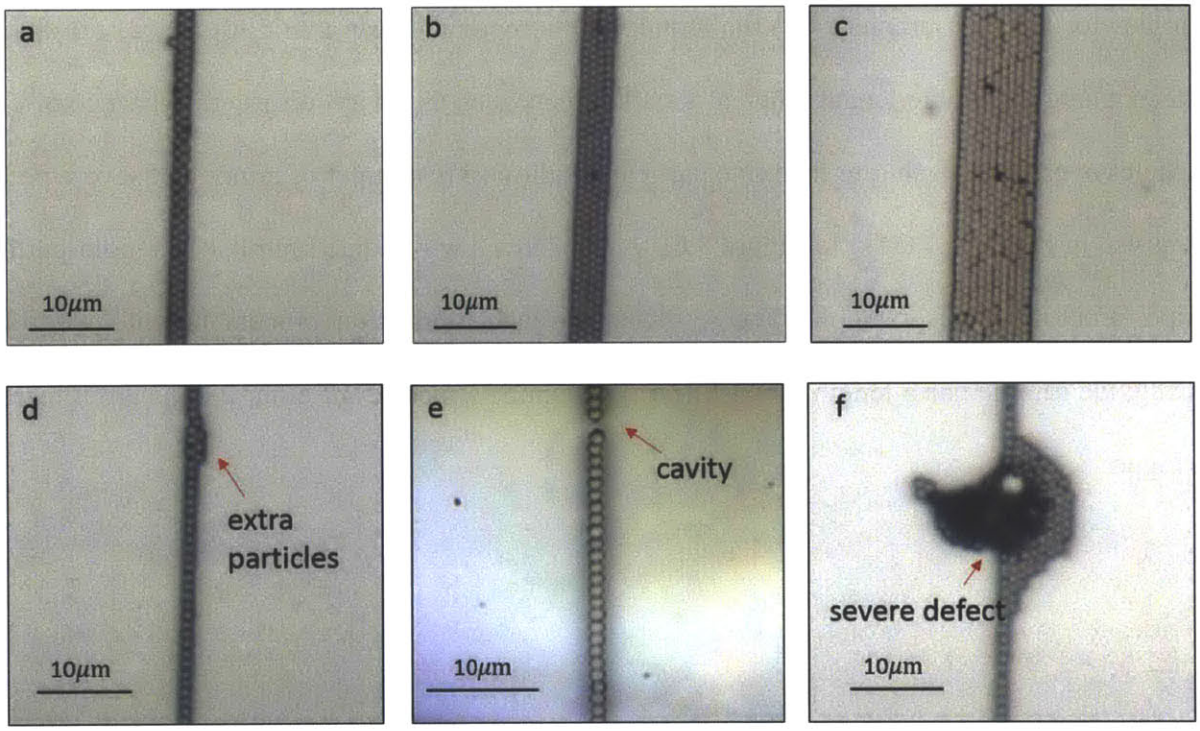

Figure 5.7 (a-c) Waveguide structures of various widths, including two-particle waveguide with $2W = 2R + \sqrt{3}R \approx 2\mu m$ (a); four-particle waveguide $2W = 2R + 3\sqrt{3}R \approx 3.9\mu m$ (b); and ten-particle waveguide with $2W = 2R + 9\sqrt{3}R \approx 9.5\mu m$ (c). (d-f) Examples of defects including a negligible defect due to the appearance of extra particles(d), a negligible defect of cavity (e), and an severe defect (f), due to which the sample is not eligible for measurement.

In addition to the waveguide structures, we have also tried to fabricate granular structures of more complicated patterns by using the same template-assisted capillary assembly. In Figure 5.8 we have exhibited several examples. Those structures may be used to study the novel physics phenomena as well as in the practical application. Figure 5.8.a is a coupled waveguide structure. The two stripes of particles can be treated as two waveguides. Since they are deposited close to each other, we can use this structure to study the crosstalk between neighboring waveguides [90]. The bending structure as shown in Figure 5.8.c can be used in the confinement effect analysis.

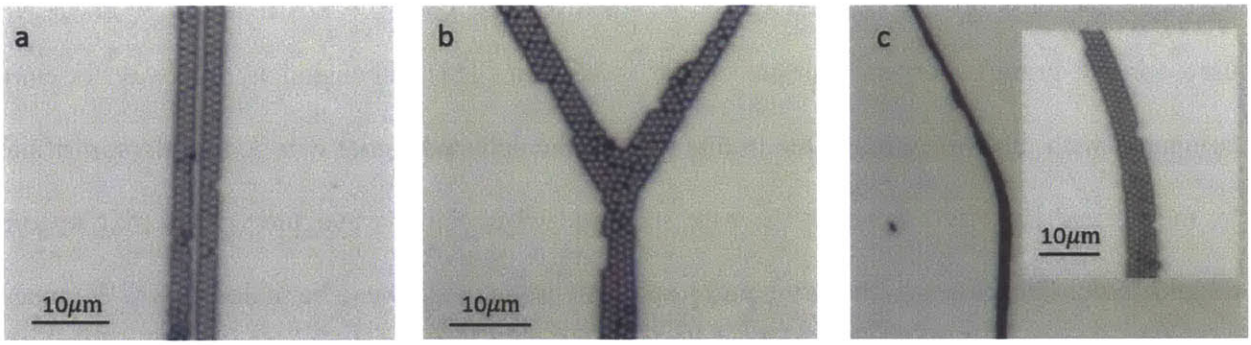

Figure 5.8 Examples of granular structures with more complicated patterns, including the coupled waveguides (a), splitting (b) and bending (c).

We can see that splitting and bending structures are not as ordered as the stripe structures such as the coupled waveguide in Figure 5.8.a and the waveguide structures introduced previously. It is mainly due to that the profile of the whole template structure cannot be exactly perpendicular to the receding direction of the meniscus during the assembly process. Therefore the meniscus front cannot be flattened into a straight line to have particles assembled with high ordering. However, those examples have demonstrated that the template-assisted capillary assembly is an effective technique for sparsely patterned granular structure.

5.3 Measurement Results

Before using the transient grating method to measure the waveguide sample, several modifications to the measurement setup are required. As introduced in Chapter 4, the pump spot on the monolayer sample has a diameter of 500μm. We cannot use this large sized pump beam to excite SAWs on a waveguide sample. This pump spot is much wider than waveguide samples whose widths are smaller than 10μm. Therefore this spot will excite not only the waveguide mode inside of the granular structure but also the normal Rayleigh wave on the substrate around the waveguide sample. In addition, the probe spot has the same problem. The diameter of probe spot used for the granular crystal sample before is 150μm. This dimension is still way too large compared with the waveguide. Due to this reason, the detected signal will be mainly contributed by the normal Rayleigh wave on the bare substrate whereas the waveguide mode may become undetectable. Therefore widths of the pump spot and probe spot have to be scaled down. We placed a cylindrical lens with a focal length of 10cm on the light path of the pump beam. In this way the pump beam spot on the sample is deformed into an ellipse with a major radius of 320μm and a minor radius of 45μm. As for the probe beam, two cylindrical lenses, whose respective focal lengths are 70cm and 8cm, were placed on the light path of probe beam. After passing through those two lenses, the probe beam was shrunk to an ellipse with a major radius of 90μm and a minor radius of 30μm. The orientations of pump and probe spots were adjusted in order to have their major axis parallel with the waveguide length and minor axis parallel with the waveguide width. The waveguide sample was placed at the center of the probe beam when we measured its dispersion property. The total energy of each pump pulse is 0.25μJ, which can guarantee the motion of particles is still in the linear regime.

Although dimensions of the probe beam and the pump beam are still too large compared with the waveguide sample, we can do a preliminary measurement. Given the current experimental setting we are able to observe the waveguide effect. In the following sections, results of measurement on the dispersion property and the confinement effect are introduced.

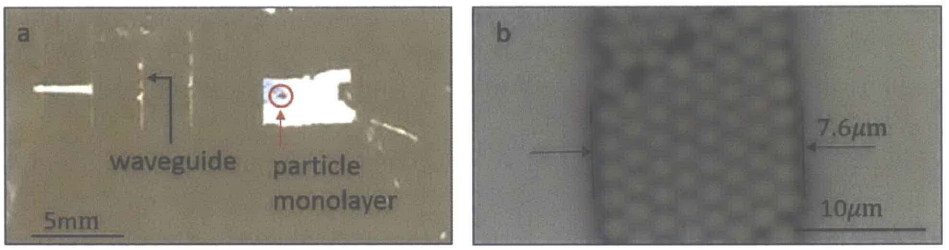

Figure 5.9 (a) Photo of the waveguide sample. The black arrow denotes the measured eight-particle waveguide. The red arrow denotes the region covered by a monolayer of granular crystal. There are some other waveguide structures on this sample substrate. (b) Microscope photo of the waveguide sample.

5.3.1 Dispersion Property of Waveguide Sample

The measured sample is an eight-particle waveguide, namely there are eight columns of closely packed particles along the width (Figure 5.9). The width of this waveguide is $2W = 2R + 7\sqrt{3}R \approx 7.6\mu m$. Although substrates for different samples are of the same type, they can still have different properties such as the surface roughness. That substrate variation will result in different dispersion properties of SAWs and the strength of Hertzian contact with particles. The photoresist template used for this measured waveguide sample has a large rectangular pattern, which is not covered by photoresist (Figure 5.9.a). We specially designed this pattern in order to have a considerably large monolayer structure deposited inside of this rectangular region. Then we can do the measurement on the monolayer structure at first to examine the dispersion property of the granular crystal and estimate values of several parameters including c_T, c_L, f_0. In this way we do

not need to use the parameters previously measured from the monolayer sample and avoid the influence from the variation of substrates.

As shown in Figure 5.9.a, there is a considerably large granular crystal monolayer deposited on the substrate, which is highlighted by the red circle. We use the same measurement technique and data processing method employed in Chapter 4. The pump spot and the probe spot have been scaled down as described previously. From the off-particle measurement result we obtain the fitted velocities of longitudinal wave, transverse wave and normal Rayleigh wave, which are $c_T = 3467\text{m/s}, c_L = 5840\text{m/s}, c_R = 3167\text{m/s}$, respectively. Given that result, we can estimate the value of resonance frequency from the on-particle measurement and get $f_0 = 215\text{MHz}$ for the granular crystal on this specific substrate. Dispersion curves for SAWs and bulk waves are displayed in Figure 5.10. As expected, the monolayer region exhibits the same dispersion profile of a modulated Rayleigh wave as that introduced in chapter 4. We can observe the disparity between the estimated f_0 and the measured data. As discussed in chapter 4, it is mainly due to the limited number of data points measured at the flat dispersion region.

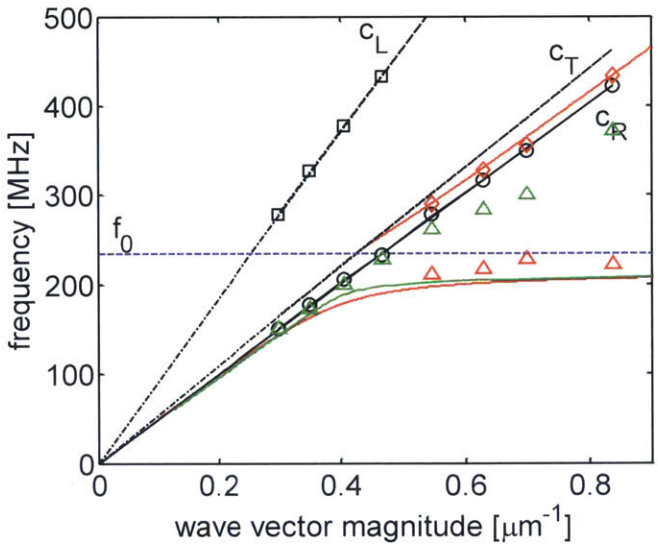

Figure 5.10 Dispersion relations. The solid red, black, and two dashed black curves are numerical results for the modulated Rayleigh wave from the on-particle measurement, the normal Rayleigh wave from the off-particle measurement, and transverse and longitudinal bulk waves. The resonance frequency f_0 of this granular crystal is denoted by the dashed blue line. The markers are measurement data. Green triangles correspond to the measurement data on the waveguide structure. The green solid line is numerical result for the first waveguide mode.

After obtaining the estimated parameters, we can measure the dispersion property of the waveguide sample. The measurement process is the same as that for granular crystal sample. The sample is placed at the center of the excitation spot and the probe spot, and oriented to make the length parallel with the major axis of pump and probe spots. Fourier spectra measured with multiple wavelengths are illustrated in Figure 5.11. For the first four measurement results with short wavelengths, we can observe that the peaks from the on-waveguide measurements are starkly different from the normal Rayleigh wave on a bare substrate. When the wavelength gets larger, the disparity between the waveguide mode and the normal Rayleigh mode disappears, which is consistent with our numerical result in Figure 5.2. We can observe that the peaks in the short-wavelength measurements are not as sharp and distinct as in the measurement on the granular crystal sample. In addition, several small peaks are presented and located close to each other in the

measured spectra. It is possibly due to the mingling of multiple waveguide modes whose frequencies are close to each other. From Figure 5.10, we can see that the measured waveguide mode behaves similar to the normal Rayleigh wave and their frequencies are above the resonance frequency, which indicates the large sized pump and probe spots have influenced the measurement. We have also plotted the measured peaks for the modulated Rayleigh wave in the waveguide structure in Figure 5.8 as marked by green triangles. The measured data points deviate from the numerical result (the green curve) obviously. In Figure 5.8, the measured waveguide data points are close to the normal Rayleigh wave and exceed the frequency of resonant contact. Thus it suggests the signal contributed by the normal Rayleigh wave on the outer region has influenced the detection of waveguide mode. As we mentioned before, this problem is unavoidable due to the large dimensions of pump spot and probe spot in our experiement.

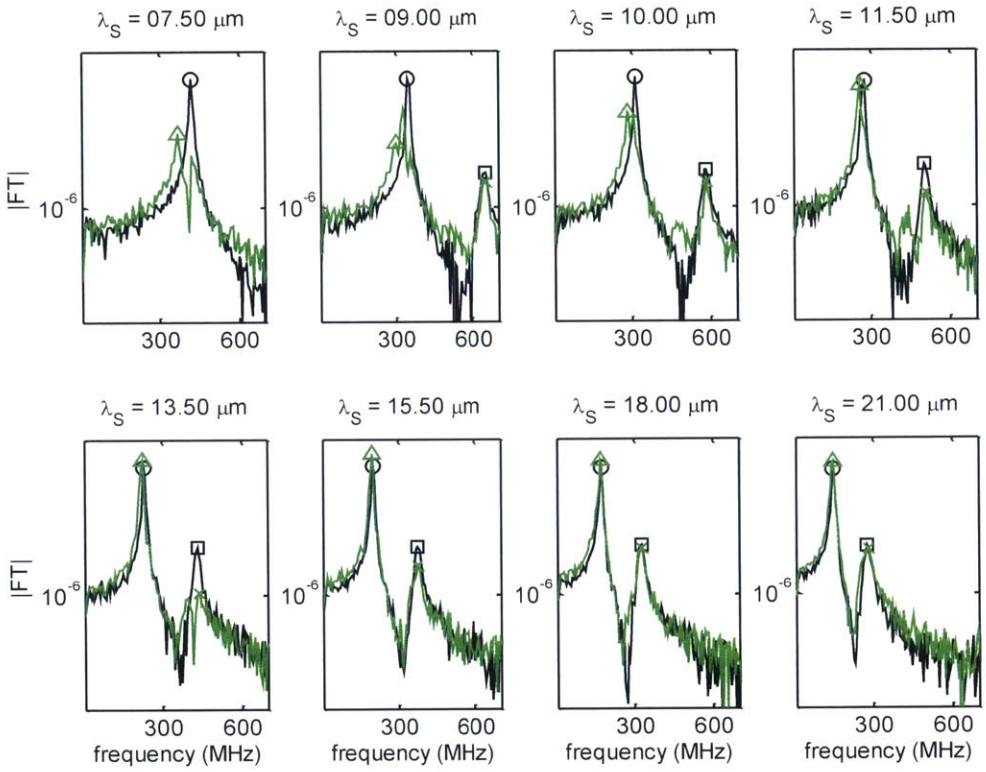

Figure 5.11 Fourier Spectra. Green curves are for the on-waveguide measurement results. The green triangles mark the peaks corresponding to the waveguide modes and the green crosses corresponding to the longitudinal wave modes. Black curves are the off-particle measurement done on the bare substrate. Black circles denote modes of the normal Rayleigh wave and black squares denote the longitudinal wave modes.

5.3.2 Confinement Measurement

Despite that the dimensions of pump spot and probe spot are too large for the waveguide structure to measure the waveguide dispersion spectrum, we can still clearly detect the difference between the wave inside of the waveguide structure and the normal Rayleigh wave under current experimental condition. Therefore, a measurement on the confinement effect of our waveguide structure is still possible. This time, we do the transient grating measurement on different locations of the waveguide sample. Both the pump spot and the probe spot were shifted along a line perpendicular to the waveguide structure. In each step, the two spots were moved by 1μm. The

wavelength of SAWs excited in the sample is 11.5μm. In Figure 5.12, the measurement across the waveguide structure is illustrated. The dispersion curve measured in on-waveguide case and in off-waveguide case are distinctly different.

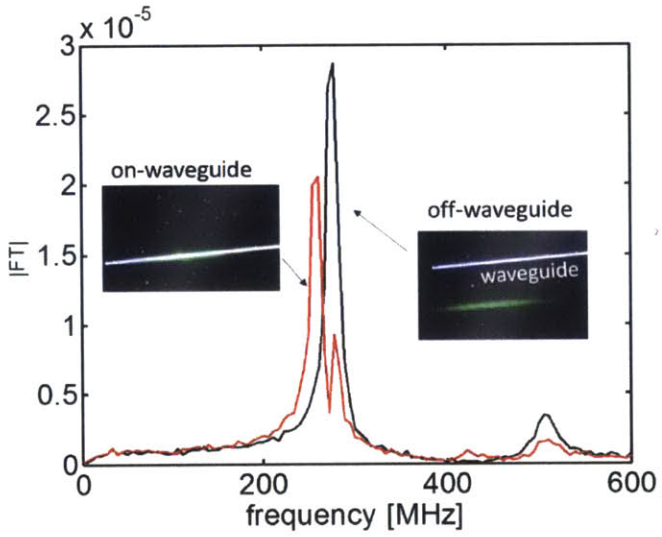

Figure 5.12 The on-waveguide (red curve) and off-waveguide (black curve) measurements. The pump spot and probe spot are shifted across the waveguide. The spectra of these two cases are distinctly different.

In Figure 5.13, the spectra measured by shifting the measurement spots across the waveguide structure are exhibited. We can observe that as the measurement spots scan across the waveguide structure, the measured spectrum profile changes sharply. There are in total eleven spectra corresponding to the on-waveguide measurement as denoted in Figure 5.13 and others are for the off-waveguide measurement. Considering the width of waveguide sample $2W \approx 7.6\mu m$ and the large sizes of pump spot and probe spot, this line-scanning measurement has reflected a good confinement effect of our granular SAW waveguide.

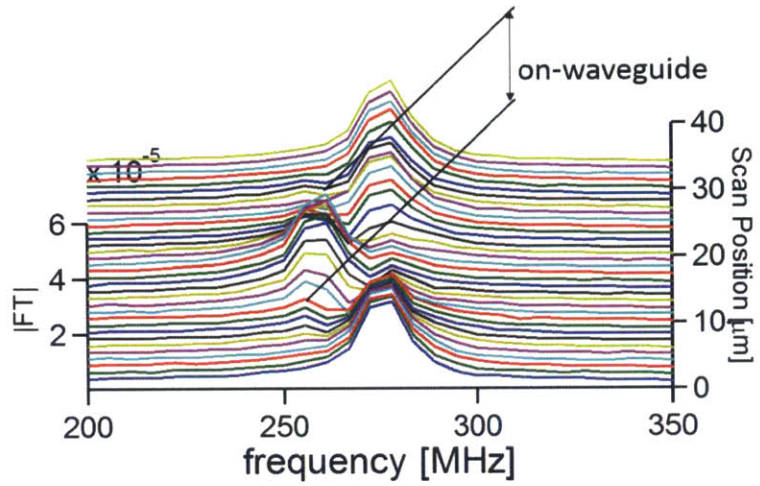

Figure 5.13 The confinement effect measurement. As spots scan across the waveguide structure, the measured Fourier spectrum changes sharply. Spectra for the on-waveguide measurement are denoted.

5.4 Conclusion

In this chapter, we have discussed the design of granular waveguide for SAWs. Due to the wave modulation by contact resonance, our granular crystal sample can effectively slow down the wave around the frequency of contact resonance. We have applied this slow velocity in granular crystal structure to the waveguide for SAWs. In section 5.2, we have analyzed the waveguide modes of the granular waveguide and examined the confinement effect via numerical computation. In section 5.3, the fabrication method for the structured granular material has been provided. We are able to make use of the template to assemble particles into stripe pattern for the waveguide sample as well as more complicated structures. We have also demonstrated the effective removal of photoresist template by making use of the strong adhesion between substrate surface and particles. In section 5.3, we discussed the measurement results on the waveguide sample. Although the current measurement conditions are not ideal, we are able to observe the sharp difference

between waveguide mode and the normal Rayleigh wave mode. The validity of this granular-material-based waveguide is supported by our measurement result. In addition, the initial measurement has also verified the good confinement performance of our granular waveguide.

Chapter 6 Conclusion

This thesis has studied the surface mechanical wave in a two-dimensional granular crystal, composed of closely packed spherical particles with a microscale diameter. Due to that small dimension of microparticles, the Hertzian contact between particles and the substrate becomes a dominant mechanics which is able to influence the wave propagation along the substrate surface effectively. Given the relation between the wave frequency and the dimension of granular unit, the effective wave modulation can be raised to a frequency range $\sim 10^2$MHz in our granular crystal system. We have observed the wave modulation and analyzed the modulation mechanism via both the numerical computation and the experimental measurement. The dispersion spectrum of the modulated wave exhibited a classic "avoided crossing" phenomenon around the resonance frequency of particle oscillation induced by Hertzian contact, which validated the strong coupling between particle motion and the mechanical wave. Our measurement results of different samples were in great consistency with the contact model that we have proposed. We also designed and fabricated a patterned granular structure, which can achieve the waveguide function dependent on the slow wave velocity in our granular crystal.

In chapter 2 we modeled the granular crystal system into an array of oscillators connected by a contact spring to the substrate. We started from the analysis on the Hertzian contact as well as the unmodulated wave behavior, and then combined these two mechanisms according to the proposed model. We have theoretically derived the dispersion relation of the modulated SAWs. Different factors which would influence the wave behavior including the particle dimension, the work of adhesion, and the unit cell area were discussed for the controllability in wave modulation.

In chapter 3 we focused on the sample fabrication. Considering the small dimension of particles in the granular system, we employed a convective assembly method in a wedge-shaped cell to fabricate the monolayer of closely packed micro/nanoparticles. The assembly mechanism was explored for not only a robust fabrication result but also the ability to achieve different granular crystal samples. Therefore an experimental examination on the relation between sample structure and the wave modulation was enabled.

In chapter 4 we provided the measurement results on two different granular crystal samples. The experimental observation validated the strong coupling between SAWs and the particle motion around the resonance frequency of Hertzian contact. The measured dispersion relation was in agreement with the numerical computation completed in chapter 2, which proved the validity of our model. Two different samples composed of two differently sized particles were compared in order to experimentally analyze the influence of particle dimension on the wave behavior. The result was again consistent with our numerical result.

In chapter 5, we proposed to replace the metal strip in the normal SAW strip waveguides with the microparticle granular crystal and made use of the slow wave supported by granular crystals to realize the waveguide effect. We fabricated the granular waveguide by using the template-assisted capillary assembly and experimentally measured the dispersion relation and the confinement effect of the waveguide sample. Although the large size of pump and probe spots in our measurement system limited the measurement accuracy, we could still see the distinct difference between the wave supported by waveguide structure and the normal wave propagating on the bare substrate, which verified the waveguide function of our granular structure. We have also completed a preliminary test on the confinement effect and the result justified a good confinement performance of our granular waveguide.

The coupling between SAWs and contact resonance is not only interesting in terms of its novel physics but also significant for the practical engineering applications. The wave modulation is raised to the frequency on the scale of 10^2MHz in our granular system. Thus our granular crystal sample can also be applied in signal processing devices which depend on SAWs. In our current study, the wave length is considerably larger than the dimension of unit particle. Therefore the effective medium approximation is valid. We expect the phonoic-crystal-like behavior as the wavelength scales down to the particle dimension, which will be part of our future work. In addition, the current model is based on the linear contact mechanics. As the excitation strength increases, the nonlinear effect should be taken into account. Considering the variety of nonlinear wave phenomena in the macroscopic granular system, more abundant wave behaviors and an improved ability to modulate SAWs are expected from the future study on nonlinear SAWs in a microscopic granular system.

Bibliography

[1] V. Chan and A. Perlas, in *Atlas Ultrasound-Guided Proced. Interv. Pain Manag.* (2011), pp. 13–19.

[2] T. Gorishnyy, M. Maldovan, C. Ullal, and E. Thomas, Phys. World **18**, 24 (2005).

[3] P. Hess, Phys. Today **55**, 42 (2002).

[4] A. G. Piersol and T. L. Paez, *Harris' Shock and Vibration Handbook* (2010), p. 14.

[5] G. Theocharis, N. Boechler, and C. Daraio, in *Acoust. Metamaterials Phononic Cryst.* (2013).

[6] M. Maldovan, Nature **503**, 209 (2013).

[7] H. Hertz, J. Für Die Reine Und Angew. Math. (1882).

[8] J. D. Goddard, Proc. R. Soc. A Math. Phys. Eng. Sci. **430**, 105 (1990).

[9] V. F. Nesterenko, *Dynamics of Heterogeneous Materials / Vitali F. Nesterenko.* (New York : Springer, c2001., 2001).

[10] C. Daraio, V. Nesterenko, E. Herbold, and S. Jin, Phys. Rev. Lett. **96**, 058002 (2006).

[11] F. Fraternali, M. A. Porter, and C. Daraio, Mech. Adv. Mater. Struct. **17**, 1 (2009).

[12] C. Daraio, V. Nesterenko, E. Herbold, and S. Jin, Phys. Rev. E **72**, 016603 (2005).

[13] D. Khatri, C. Daraio, and P. Rizzo, in *15th Int. Symp. Smart Struct. Mater. Nondestruct. Eval. Heal. Monit.*, edited by P. J. Shull, H. F. Wu, A. A. Diaz, and D. W. Vogel (International Society for Optics and Photonics, 2008), p. 69340U–69340U–8.

[14] A. Spadoni and C. Daraio, Proc. Natl. Acad. Sci. U. S. A. **107**, 7230 (2010).

[15] N. Boechler, G. Theocharis, and C. Daraio, Nat. Mater. **10**, 665 (2011).

[16] M. D. Murthy Peri and C. Cetinkaya, J. Colloid Interface Sci. **288**, 432 (2005).

[17] G. L. Dybwad, J. Appl. Phys. **58**, 2789 (1985).

[18] E. Vittorias, M. Kappl, H.-J. Butt, and D. Johannsmann, Powder Technol. **203**, 489 (2010).

[19] Y. A. Kosevich and E. S. Syrkin, Phys. Lett. A **135**, 298 (1989).

[20] E. Garova, A. Maradudin, and A. Mayer, Phys. Rev. B **59**, 13291 (1999).

[21] Y. Achaoui, A. Khelif, S. Benchabane, L. Robert, and V. Laude, Phys. Rev. B **83**, 104201 (2011).

[22] W. Cai and V. M. Shalaev, *Optical Metamaterials* (Springer, 2010).

[23] P. A. Deymier, editor , *Acoustic Metamaterials and Phononic Crystals* (Springer Berlin Heidelberg, Berlin, Heidelberg, 2013).

[24] R. Liu, T. Cui, D. Huang, B. Zhao, and D. Smith, Phys. Rev. E **76**, 026606 (2007).

[25] J. B. Pendry, A. J. Holden, D. J. Robbins, and W. J. Stewart, IEEE Trans. Microw. Theory Tech. **47**, 2075 (1999).

[26] R. A. Shelby, D. R. Smith, and S. Schultz, Science **292**, 77 (2001).

[27] U. Leonhardt, Science **312**, 1777 (2006).

[28] J. B. Pendry, D. Schurig, and D. R. Smith, Science **312**, 1780 (2006).

[29] Z. Liu, Science (80-.). **289**, 1734 (2000).

[30] S. John, Phys. Rev. Lett. **58**, 2486 (1987).

[31] T. F. Krauss, R. M. D. La Rue, and S. Brand, Nature **383**, 699 (1996).

[32] A. A. Maznev and O. B. Wright, J. Appl. Phys. **105**, 123530 (2009).

[33] V. Laude, M. Wilm, S. Benchabane, and A. Khelif, Phys. Rev. E **71**, (2005).

[34] A. Khelif, Y. Achaoui, and B. Aoubiza, J. Appl. Phys. **112**, 033511 (2012).

[35] I. A. Veres, T. Berer, O. Matsuda, and P. Burgholzer, J. Appl. Phys. **112**, 053504 (2012).

[36] D. Yudistira, A. Boes, B. Djafari-Rouhani, Y. Pennec, L. Y. Yeo, A. Mitchell, and J. R. Friend, Phys. Rev. Lett. **113**, 215503 (2014).
[37] (n.d.).
[38] D. Tabor, J. Colloid Interface Sci. **58**, 2 (1977).
[39] V. . Muller, V. . Yushchenko, and B. . Derjaguin, J. Colloid Interface Sci. **77**, 91 (1980).
[40] M. D. Pashley, Colloids and Surfaces **12**, 69 (1984).
[41] I. H. Background, **150**, (1992).
[42] J. N. Israelachvili, *Intermolecular and Surface Forces: Revised Third Edition (Google eBook)* (Academic Press, 2011), p. 704.
[43] A. I. H. Committee, *ASM Handbook, Volume 02 - Properties and Selection: Nonferrous Alloys and Special-Purpose Materials* (ASM International, 1990).
[44] N. P. BANSAL and R. H. DOREMUS, *Handbook of Glass Properties* (Elsevier, 1986).
[45] Y. Guillet, B. Audoin, M. Ferrié, and S. Ravaine, Phys. Rev. B **86**, 035456 (2012).
[46] W. M. Ewing, W. S. Jardetzky, F. Press, and A. Beiser, Phys. Today **10**, 27 (1957).
[47] E. Barthel, J. Phys. D. Appl. Phys. **41**, 163001 (2008).
[48] D. R. Lide, *CRC Handbook of Chemistry and Physics, 94th Edition, 2013-2014* (2013), p. 2616.
[49] S. Eichenlaub, C. Chan, and S. P. Beaudoin, J. Colloid Interface Sci. **248**, 389 (2002).
[50] A. Di Falco, S. C. Kehr, and U. Leonhardt, Opt. Express **19**, 5156 (2011).
[51] T. Zentgraf, Y. Liu, M. H. Mikkelsen, J. Valentine, and X. Zhang, Nat. Nanotechnol. **6**, 151 (2011).
[52] A. Vakil and N. Engheta, Science **332**, 1291 (2011).
[53] S. Rondineau, M. Himdi, and J. Sorieux, IEEE Antennas Wirel. Propag. Lett. **2**, 163 (2003).
[54] S. K. Yao and D. B. Anderson, Appl. Phys. Lett. **33**, 307 (1978).
[55] J. Dockrey, M. Lockyear, S. Berry, S. Horsley, J. Sambles, and A. Hibbins, Phys. Rev. B **87**, 125137 (2013).
[56] H. F. Ma and T. J. Cui, Nat. Commun. **1**, 124 (2010).
[57] H. Mosallaei and Y. Rahmat-Samii, IEEE Trans. Antennas Propag. **49**, 60 (2001).
[58] C. A. Boyles, J. Acoust. Soc. Am. **45**, 356 (1969).
[59] P. Pieranski, Phys. Rev. Lett. **45**, 569 (1980).
[60] B. van Duffel, R. H. A. Ras, F. C. De Schryver, and R. A. Schoonheydt, J. Mater. Chem. **11**, 3333 (2001).
[61] M. Szekeres, O. Kamalin, R. a. Schoonheydt, K. Wostyn, K. Clays, A. Persoons, and I. D??k??ny, J. Mater. Chem. **12**, 3268 (2002).
[62] S. O. Lumsdon, E. W. Kaler, J. P. Williams, and O. D. Velev, Appl. Phys. Lett. **82**, 949 (2003).
[63] P. Born, S. Blum, A. Munoz, and T. Kraus, Langmuir **27**, 8621 (2011).
[64] J. Sun, C. Tang, P. Zhan, Z. Han, Z.-S. Cao, and Z.-L. Wang, Langmuir **26**, 7859 (2010).
[65] R. Ye, Y.-H. Ye, Z. Zhou, and H. Xu, Langmuir **29**, 1796 (2013).
[66] A. S. Dimitrov and K. Nagayama, Langmuir **12**, 1303 (1996).
[67] B. G. Prevo and O. D. Velev, Langmuir **20**, 2099 (2004).
[68] V. Canalejas-Tejero, M. Ibisate, D. Golmayo, A. Blanco, and C. López, Langmuir **28**, 161 (2012).
[69] N. Denkov, O. Velev, P. Kralchevski, I. Ivanov, H. Yoshimura, and K. Nagayama, Langmuir **8**, 3183 (1992).

[70] C. D. Dushkin, H. Yoshimura, and K. Nagayama, Chem. Phys. Lett. **204**, 455 (1993).
[71] A. S. Dimitrov, C. D. Dushkin, H. Yoshimura, and K. Nagayama, Langmuir **10**, 432 (1994).
[72] M. H. Kim, S. H. Im, and O. O. Park, Adv. Funct. Mater. **15**, 1329 (2005).
[73] M. Kagan, W. V. Pinczewski, and P. E. Oren, J. Colloid Interface Sci. **170**, 426 (1995).
[74] J. Berthier and K. A. Brakke, *The Physics of Microdroplets* (John Wiley & Sons, Inc., Hoboken, NJ, USA, 2012).
[75] P. Kumnorkaew, Y.-K. Ee, N. Tansu, and J. F. Gilchrist, Langmuir **24**, 12150 (2008).
[76] P. a Kralchevsky and K. Nagayama, Adv. Colloid Interface Sci. **85**, 145 (2000).
[77] R. D. Deegan, O. Bakajin, T. F. Dupont, G. Huber, S. R. Nagel, and T. A. Witten, Nature **389**, 827 (1997).
[78] R. Deegan, Phys. Rev. E. Stat. Phys. Plasmas. Fluids. Relat. Interdiscip. Topics **61**, 475 (2000).
[79] R. Deegan, O. Bakajin, T. Dupont, G. Huber, S. Nagel, and T. Witten, Phys. Rev. E. Stat. Phys. Plasmas. Fluids. Relat. Interdiscip. Topics **62**, 756 (2000).
[80] X. Shen, C.-M. Ho, and T.-S. Wong, J. Phys. Chem. B **114**, 5269 (2010).
[81] A. Sangani, C. Lu, K. Su, and J. Schwarz, Phys. Rev. E **80**, 011603 (2009).
[82] V. H. Chhasatia, A. S. Joshi, and Y. Sun, Appl. Phys. Lett. **97**, 231909 (2010).
[83] R. M. Slayton and K. A. Nelson, J. Chem. Phys. **120**, 3908 (2004).
[84] J. a. Johnson, A. a. Maznev, M. T. Bulsara, E. a. Fitzgerald, T. C. Harman, S. Calawa, C. J. Vineis, G. Turner, and K. a. Nelson, J. Appl. Phys. **111**, 023503 (2012).
[85] Q. Li, K. Hoogeboom-Pot, D. Nardi, M. M. Murnane, H. C. Kapteyn, M. E. Siemens, E. H. Anderson, O. Hellwig, E. Dobisz, B. Gurney, R. Yang, and K. a. Nelson, Phys. Rev. B **85**, 195431 (2012).
[86] A. A. Kolomenskii and A. A. Maznev, in *Die Kunst Phonons* (Springer, 1994), pp. 99–104.
[87] M. Kopycinska-Müller, R. H. Geiss, and D. C. Hurley, Ultramicroscopy **106**, 466 (2006).
[88] A. A. Oliner, Proc. IEEE **64**, 615 (1976).
[89] K. Giannelli, L. Giovannini, E. Verona, and G. Socino, 1996 IEEE Ultrason. Symp. Proc. **1**, (1996).
[90] D. Morgan and E. G. S. Paige, *Surface Acoustic Wave Filters* (Elsevier, 2007), pp. 293–316.
[91] P. H. Otsuka, K. Nanri, O. Matsuda, M. Tomoda, D. M. Profunser, I. A. Veres, S. Danworaphong, A. Khelif, S. Benchabane, V. Laude, and O. B. Wright, Sci. Rep. **3**, 3351 (2013).
[92] M. Oudich and M. Badreddine Assouar, J. Appl. Phys. **111**, 014504 (2012).
[93] Y. Achaoui, A. Khelif, S. Benchabane, and V. Laude, J. Phys. D. Appl. Phys. **43**, 185401 (2010).
[94] J.-H. Sun and T.-T. Wu, Phys. Rev. B **74**, 174305 (2006).
[95] H. F. Tiersten, J. Appl. Phys. **40**, 770 (1969).
[96] L. Malaquin, T. Kraus, H. Schmid, E. Delamarche, and H. Wolf, Langmuir **23**, 11513 (2007).
[97] M. Rycenga, P. H. C. Camargo, and Y. Xia, Soft Matter **5**, 1129 (2009).
[98] T. Kraus, L. Malaquin, E. Delamarche, H. Schmid, N. D. Spencer, and H. Wolf, Adv. Mater. **17**, 2438 (2005).
[99] Y. Yin, Y. Lu, B. Gates, and Y. Xia, J. Am. Chem. Soc. **123**, 8718 (2001).

[100] S. M. Yang, H. Míguez, and G. A. Ozin, Adv. Funct. Mater. **12**, 425 (2002).
[101] Q. He, F. Sévérac, H. Hajjoul, Y. Viero, and A. Bancaud, Langmuir **27**, 6598 (2011).
[102] C.-A. Fustin, G. Glasser, H. W. Spiess, and U. Jonas, Langmuir **20**, 9114 (2004).
[103] A. Ruiz, C. A. Mills, A. Valsesia, E. Martinez, G. Ceccone, J. Samitier, P. Colpo, and F. Rossi, Small **5**, 1133 (2009).